NASA Contractor Report 4537

A Study of the Merritt Island, Florida Sea Breeze Flow Regimes and Their Effect on Surface Heat and Moisture Fluxes

M.T. Rubes, H.J. Cooper, and E.A. Smith
Florida State University
Tallahassee, Florida

Prepared for
George C. Marshall Space Flight Center
under Grant NAG8-916

National Aeronautics and Space Administration
Office of Management
Scientific and Technical Information Program
1993

(NASA-CR-4537) A STUDY OF THE MERRITT ISLAND, FLORIDA SEA BREEZE FLOW REGIMES AND THEIR EFFECT ON SURFACE HEAT AND MOISTURE FLUXES (Florida State Univ.) 154 p

N94-12580

Unclas

H1/47 0184988

Acknowledgments

Throughout the numerous phases of this project, many people have generously shared their expertise, thoughts and ideas with the authors. The authors would like to thank Drs. Paul Ruscher and Kevin Kloesel at Florida State University for providing valuable discussions throughout the project. Also at Florida State University, Mr. Frank Paolino and Mr. Jim Merritt, who helped in the preparation of many of the figures presented here. At Marshall Space Flight Center, the authors would like to thank Dr. Bill Crosson for his help during the field phase of the project and many subsequent discussions, and Dr. Steve Goodman for his guidance on the project development. Without their collaboration, this study would not have been possible. This research was supported by NASA grants NAG8-916 and NAG8-881.

PRECEDING PAGE BLANK NOT FILMED

Table of Contents

PRECEDING PAGE BLANK NOT FILMED

List of Figures

PRECEDING PAGE BLANK NOT FILMED

List of Tables

Summary

Surface, upper-air and satellite data collected during the Convective and Precipitation/Electrification Experiment have been analyzed as part of an investigation of the sea breeze in the vicinity of Merritt Island, Florida. Analysis of the five-minute near-surface divergence fields shows that the classical 24-hour oscillation in divergence over the island due to the direct sea breeze circulation is frequently disrupted and exhibits two distinct modes. In the first mode (referred to as Type 1), convergence persists during the nighttime as well as during the afternoon, whereas in the second mode (Type 2), the classical diurnal oscillation prevails. Upper-air data show that these two surface convergence modes are closely related to the flow conditions aloft. The first mode occurs under deep easterly flow, while the second mode occurs when westerlies predominate in the lowest seven kilometers of the atmosphere.

By defining conditions as disturbed, when large scale processes were obviously dominating the flow over the island, the forty days of observations during the field experiment were grouped into four basic classes: (1) a disturbed period at the beginning of the experiment; (2) another disturbed period at the end of the experiment; (3) an intermediate period in which the basic flow contains an easterly component (Type 1); and (4) another intermediate period in which the flow contains a westerly component (Type 2). The average speed of westward propagation of the sea breeze front for days

in the Type 1 regime was found to be 2.9 $m \cdot s^{-1}$, while for days under the Type 2 regime the mean westward propagation speed of the front was 2.7 $m \cdot s^{-1}$.

Typically, when the front reaches around 60-70 km inland, it is met by an eastward-propagating sea breeze convergence zone which is thought to originate on the west coast earlier in the day. The line of mature storms associated with the west coast front then merges with the east coast sea breeze, and storm cells propagate eastward towards the Atlantic coast. The average return speed of these convective lines for days in the Type 1 regime was found to be 14.3 $m \cdot s^{-1}$, whereas the return speed for days experiencing Type 2 flow was found to be 9.0 $m \cdot s^{-1}$. The spatial mean and variance in visible reflectance calculated from full resolution GOES satellite VIS imagery also correlated well with the concurrent behavior of the surface divergence fields, and this relationship was used to provide an objective indication of the nature of the convection over the area as seen by the satellite.

A comparison of clear day surface energy fluxes with fluxes on other days indicates that changes in magnitudes were dominated by the presence or absence of cloud. Type 1 and Type 2 regimes showed distinct temporal differences in the way the available energy was partitioned into sensible, latent and soil heat fluxes. Type 1 flow days tended to lose more available energy in the morning than Type 2 days due to earlier development of small cumulus over the island.

A composite storm of surface winds, surface energy fluxes, rainfall and satellite visible data was constructed from days when thunderstorm downdrafts passed directly over the surface flux sites. The radiative and thermodynamic fluxes into and out of the surface layer during the passage of a downdraft were quantified. A spectral transmittance for the cloud cover

resulting from the composite storm over the visible wavelengths has been calculated from the GOES VIS imagery and the surface measured radiometric fluxes. It is shown that pre-storm transmittances of 0.8 fall to values near 0.1 as the downdraft moves directly over the site, recovering to values of around 0.6 about 2.5 hours after the storm passage. This result emphasizes the close tie-in between the underlying dynamics and vertical circulation field to the optical properties of the clouds, particularly in terms of the surface radiation budget. Coincident with the time of minimum transmittance, a brief period of infrared equilibrium exists between the cloud and the ground.

Time integration of latent heat fluxes and rainfall rates into and out of the surface layer during the composite event provided an estimate of the cumulative surplus or deficit of water in the top soil layers. It is found that under post-composite storm conditions of continuous clear sky days, 3.5 days are required to evaporate back into the atmosphere the latent heat energy lost to the surface by rainfall. The e-folding time for clear day recovery is found to be 1.5 days which, when taken with the high frequency of summer rainfall, indicates that the surface may never fully recover during the summer months.

1.0 Introduction

The Florida peninsula has long been known to be an ideal environment for the study of summertime convection. Because of its peninsular shape, it develops a distinct land and sea breeze system which provides ample opportunity for the study of boundary layer forced convection. Understanding the details of the surface energy budget and its interrelated effects on the hydrological cycle and cloud-surface interactions are amongst the more important and difficult questions currently facing atmospheric science. At the heart of the problem, there is a need for a more complete and quantitative understanding of the surface energy budget and its control on heat and moisture exchanges between the land surface and the atmosphere in convective regimes of various types.

A number of studies have shown that variations in the moisture fluxes effect local mesoscale circulations. Mahfouf et al. (1987) found that a transition zone between bare soil and vegetated soil was the preferred location for the initiation of moist convection. They also showed that a vegetation canopy over a very wet or very dry surface may reduce the differences between latent and sensible heat fluxes. Ookouchi et al. (1984) found that large gradients in soil moisture were capable of producing mesoscale circulations with intensities rivaling those observed in sea breeze circulations and that even small soil moisture gradients could result in significant mesoscale overturning. Segal and Arritt (1992) suggested that intensity of sea breeze or lake breeze type circulations may be modified by nonuniformities in the surface sensible heat flux

fields. Yan and Anthes (1988) showed that gradients in land moisture in conjunction with a convectively unstable atmospheric environment could initiate convective rainfall. Segal et al. (1988) showed that the influence vegetated surfaces can have on mesoscale circulations is highly dependent on atmospheric conditions as well as the characteristics of the vegetation. An analysis of measurements obtained during the 1989 First ISLSCP Field Experiment (FIFE) by Smith et al. (1993), showed evidence of a thermally direct secondary circulation at a scale below 50 kilometers driven by gradients in soil moisture and vegetation.

The exact role played by surface fluxes of moisture in the global hydrological cycle, as well as in the initiation and maintenance of convection and mesoscale circulations, is still not completely understood. The net flow of water from ocean to land by advection of marine air masses onto continental areas and subsequent return of the water to the ocean by river flow and runoff is known at best to a factor of two or three (Chahine 1992). For example, Yeh et al. (1984) found through the use of a numerical model that irrigation practices, which are poorly monitored and documented around the world, affect not only the distribution of evapotranspiration, but also the distribution of large scale rainfall systems. Carlson et al. (1981) used satellite infrared measurements along with a one-dimensional boundary layer model to investigate the distribution of surface fluxes of latent and sensible heat over urbanized areas, where they found a significant reduction of moisture availability and an increase in sensible heat flux. More recently, Simpson et al. (1993) examined surface fluxes under deep convection off the northern coast of Australia and found that even on days when these islands were under a dense cirrus overcast, the islands were able to provide sufficient fluxes of sensible and latent heat to initiate convection.

The impact of local circulations and the surface energy budget on short-term forecasting, is also an important topic currently under study. Pielke (1974b) used a three dimensional model of a south Florida sea breeze which included surface flux parameterization, to show that differential heating between land and water is the primary factor in determining the magnitude of low level wind divergence resulting from the sea breeze circulation. Ulanski and Garstang (1978), using data obtained in south central Florida, showed that short-term forecasting of rainfall onset and rainfall accumulation may be possible given information on the surface divergence field and within that context, established a connection between rainfall and local divergence. Along these lines, Watson et al. (1991) have described an effective method for short-term prediction of lightning at KSC based on analysis of the area-averaged surface divergence patterns. Recently, Cooper and Smith (1993) discussed the importance of short-term forecasting and its relationship to local scale surface processes around the Cape Canaveral, Florida area.

1.1 Scientific Objectives and Relevance of Study

There are two primary scientific objectives of this study. The first is to quantify, in detail, the interaction between sea breeze initiated surface convergence and the simultaneously observed generation and decay of cumuliform clouds over Merritt Island in eastern central Florida. The second is to determine the interrelated effects of this convective activity on the surface energy budget, with special focus on the heat and moisture fluxes. Convective activity associated with surface convergence along with the non-linear interactions between surface fluxes and convective activity play integral parts in short term forecasting. Improvements in short term forecasting of convective thunderstorms are of paramount importance everywhere. This is particularly

true in central Florida around the Kennedy Space Center, where thunderstorms often cause disruptions in launch operations and other activities being carried out by the National Aeronautical and Space Administration (NASA). In addition, knowledge gained from the study of surface fluxes in sea and land breeze type circulations is important in other areas of meteorology such as pollution dispersion and transport and cloud-surface parameterization in General Circulation Models (GCMs).

1.2 Meteorological Background

During the summer months, central and south Florida can be classified as a quasi-tropical climate regime characterized by afternoon thunderstorms embedded in mesoscale regions of low level convergence. These patterns of low level convergence are initiated by sea and land breezes. The Florida sea breeze has been extensively studied and documented since the 1940's. Sea breezes, in general, have been described in detail in ancient literature dating as far back as 800 B. C. in the Homeric epics *Iliad* and *Odyssey* (Neumann 1973).

Both observational and numerical studies of the Florida sea breeze agree that a primary determinant of location, strength and pattern of convective activity associated with the sea breeze front is the prevailing direction of the synoptic flow (Foote 1991). The sea breeze and the associated spatial pattern of convection can have markedly different characteristics dependent on whether the ambient flow is onshore, offshore or parallel to the shore. Byers and Rodebush (1948) and Byers and Braham (1949) were amongst the first to suggest that low level convergence was a necessary condition for the initialization of convective activity. They also concluded that the synoptic flow could then act as a catalyst to initiate convection or act to suppress any convection forming in the sea breeze circulations. Gentry and Moore (1954) further analyzed the pattern of convective

activity in terms of the direction of synoptic flow and in terms of the time of day that the flow was occurring, and found that the locations of summer showers are controlled primarily by areas of convergence formed by the sea breeze.

When considering the eastern shore of Florida, cases where the prevailing low level flow patterns are onshore, offshore or parallel to the shore must be examined separately. Prevailing offshore flow from the east coast, that is, flow from the southwest, is usually unstable and has more moisture and larger vertical velocities than flow from other directions (Foote 1991). This is primarily due to the modification of air masses by the warm waters of the Gulf of Mexico. This flow pattern can occur as much as 50 % of the time during the months of July and August and often initiates the most intense convection (Watson and Blanchard 1984). Intense convection generally occurs because the prevailing flow is opposing the sea breeze flow such that the release of instability develops at the leading edge of the sea breeze front. Prevailing onshore flow for the east coast, that is, from the east, usually generates less intense convection than southwesterly flow over Merritt Island. This is because the large scale motions merge with the sea breeze and push the sea breeze front further inland. This flow is normally characterized by a shallow low level moist layer with relatively drier conditions aloft. This flow pattern occurs more often in August and September. Flow that parallels the coast is possible at any time during the year and makes up about 5% of all days. This type of flow, whether it is northerly or southerly, has very little influence on developing convection (Watson et al. 1991).

Northwesterly flow does not cross large water bodies before reaching the Cape and is therefore characterized by dry continental air. This flow pattern occurs about 5 % of the time during the summer months. Southeasterly flow is generally characterized by a deeper moisture profile than northwesterly or

northeasterly flows and occurs as much as 25 % of the time during the summer. This flow regime often aids in the initiation and development of convection. Calm conditions occur only about 10 % of the time. These conditions offer the greatest challenge to forecasters because the sea breeze can act alone or with river breezes stemming from the Indian and Banana Rivers to form convection around the Cape Canaveral area. Table 1 summarizes these flow regimes, how often they occurred for the summers of 1987 through 1990, and whether the influence they had on the development of convection is positive, negative or neutral; see Foote (1991), Holle et al. (1992), Blanchard and Lopez (1985), and Watson et al. (1991).

Research into the nature of Florida convection has been continuous throughout the post-war era, including scale-interaction studies which analyze how the convection is affected by synoptic scale flow. These include both observational and theoretical studies. Large, in depth observational studies of thunderstorms in the Florida Peninsula first started with the Thunderstorm Project in the summer of 1946. Byers and Rodebush (1948) investigated thunderstorms during this project and showed that temperature and humidity soundings failed to completely explain the occurrence or nonoccurrence of thunderstorms. They also suggested that large scale horizontal convergence in the low levels was a necessary condition for initiation of convection. Gentry and Moore (1954) found that spatial and diurnal variations in rain showers near the Florida coast is related to the direction and speed of the prevailing wind. Frank et al. (1967) analyzed spatial and temporal variations in radar echoes in south Florida and found them highly correlated with sea breeze patterns. Ulanski and Garstang (1978) showed a strong statistical relationship between low level convergence which may precede the onset of rain by as much as 60 minutes.

Table 1: Distribution of flow patterns at Cape Canaveral and how the flow affects convective activity for June through September of 1987 to 1990 (after Holle et al. 1992).

Flow Regime	Number of Days	Convective Influence
All	455	
NE	87	Negative
SE	59	Positive
SO	59	Neutral
SW	142	Positive
NW	15	Negative
NO	19	Neutral
Calm	74	Neutral

Burpee (1979) found a negative correlation between surface convergence and area-averaged rainfall as a result of less low level convergence in the afternoons and early evenings for days that had considerable rainfall. Cooper et al. (1982) analyzed time series of deep convective events occurring in south Florida and found a five step pattern repeated for each individual event. They then postulated the existence of a feedback effect in which storm flows triggering new convection amplified the convection embedded in regions of mesoscale convergence. Watson and Blanchard (1984) found a correlation factor of 0.75 between the change in low level convergence and rainfall for 75 convective rainfall events over south Florida during 1975. Watson et al. (1991) have utilized surface convergence patterns as a short-term predictor for cloud-to-ground lightning strikes associated with deep convection around the Kennedy Space Center.

There have also been many theoretical studies of the Florida sea breeze and its associated convection. Most agree well with observational studies. Estoque (1962) used a two layer model utilizing the hydrostatic assumption to simulate different scenarios of synoptic flow. He found that the direction of the prevailing flow could alter the distance inland to which the sea breeze front would travel and the intensity of the direct sea breeze circulation. Neumann and Mahrer (1971) modified Estoque's (1962) model by replacing Estoque's imposed constant vertical speeds with formulations which calculated the vertical velocities in response to dynamic conditions. Pielke (1974a) developed a multilevel three dimensional model of the sea breeze for south Florida that included detailed boundary layer and surface flux parameterizations, and a synoptic scale basic state. He also compared the results obtained using two-dimensional and three-dimensional models, and demonstrated that a two

dimensional model cannot accurately simulate sea breeze development over south Florida (Pielke 1974a). However, two dimensional model results have continued to be reported; e.g. Walsh (1974), Bechtold et al. (1991) and Arritt (1993). Walsh (1974) used a general coastal sea breeze model which enabled him to show that the vertical component of a direct sea breeze circulation could account for several percent of the globally averaged vertical flux of sensible heat. Mahrer and Pielke (1977) utilized a two-dimensional hydrostatic model which included simple parameterizations for the surface heat budget and shortwave/longwave radiative processes to examine large scale topographical effects on developing mesoscale circulations. They found that in the case where a mountain/valley wind could act together with a sea breeze, the most intense circulations were established. Bechtold et al. (1991) studied the effects of synoptic flow on a two dimensional model of an inland sea breeze type circulation forced by vegetative differences in the ground cover and found that an inland sea breeze type circulation is less influenced by the effects of the prevailing flow than is an actual sea breeze. In addition, Yan and Anthes (1987) performed two-dimensional numerical modeling experiments of sea breezes at different latitudes to determine whether latitude can have a major effect on the sea breeze through Coriolis effects. They found that at increasing distance from the equator, the Coriolis force may be more important than the reversal of horizontal temperature gradients from day and night in producing large sea breezes. Dalu and Pielke (1989) have found similar latitudinal effects. Xian and Pielke (1991) also used a two dimensional model to examine general sea breeze flows and how they are effected by environmental thermal stratification, synoptic flow and latitude. They found that a strip of land 150 km wide produced the maximum sea breeze convergence, that sea breeze intensity tends to be strongest

around 20° latitude, and that the strongest merged sea breezes occur in conditions of zero synoptic flow. Zhong et al. (1991) used a three-dimensional mesoscale model applied to the Merritt Island area to examine the interaction between the Indian River breeze and the Atlantic Ocean sea breeze. They found that while the horizontal components of the two circulations showed large differences, the vertical structures were quite similar. They also found that the river breeze tended to remain stationary, whereas the sea breeze often propagated inland a considerable distance.

1.3 Meteorological Field Experiments in Florida

There have been three large meteorological field experiments in Florida that have been directed towards the study of local convection; the Thunderstorm Project of the 1940's, the Florida Area Cumulus Experiment (FACE) in the 1970's, and the Convective and Precipitation/Electrification Experiment (CaPE) during 1991. All three of these major experiments took place during the summer months, and while each had its own set of particular objectives and goals, they all shared a common aim, in that they were designed to study convection and thunderstorms.

The first major experiment was The Thunderstorm Project which took place during the summer of 1946. The U. S. Weather Bureau deployed a network of temperature and humidity sensors in south Florida along with a pilot-balloon network for the investigation of convection and low level convergence. The findings of this experiment showed conclusively that low level convergence in the Florida peninsula developed practically every afternoon during the summer months as a result of the sea breeze circulation. It was also suggested that the merging of the east coast sea breeze front with the west coast sea breeze front

could explain the high frequency of thunderstorms in the interior of the Florida peninsula.

The Florida Area Cumulus Experiment (FACE) took place in the southern part of Florida just south of Lake Okeechobee during the summers of 1971, 1973, and 1975. The initial objectives mainly concerned the effects of seeding supercooled cumuli with silver iodide to determine if artificial seeding practices could enhance rainfall rates. The data set consisted of data from the Miami WSR-57 S-band weather radar and in addition, measurements from a mesonet of rain gauges and surface anemometers (Ulanski and Garstang 1978). Woodley et al. (1982) reported increases in both locations and dispersion characteristics of rainfall patterns due to the seeding. In addition to rainfall analyses, other studies have been conducted with FACE surface wind data to show connections between rainfall and low level convergence; Cooper et al. (1982) and Watson and Blanchard (1984).

The most recent large scale experiment in Florida was the Convective and Precipitation/Electrification Experiment (CaPE) which took place during July and August, 1991 over the Cape Canaveral area of east central Florida. Figure 1(a) shows a map of Florida with the CaPE study area outlined. Figure 1(b) is an enlargement of the CaPE study area and shows the locations of Merritt Island, the Indian and Banana Rivers, Cape Canaveral, and the St. Johns river basin. CaPE was a multi-agency and international project with the main objective of better understanding the short-term forecasting of lightning and thunderstorms in the general area of KSC. Various CaPE investigators deployed different networks of meteorological stations which employed a wide variety of instrumentation including sub-surface temperature and moisture sensors, mesonet and upper-air wind systems, radars, and a number of aircraft mounted

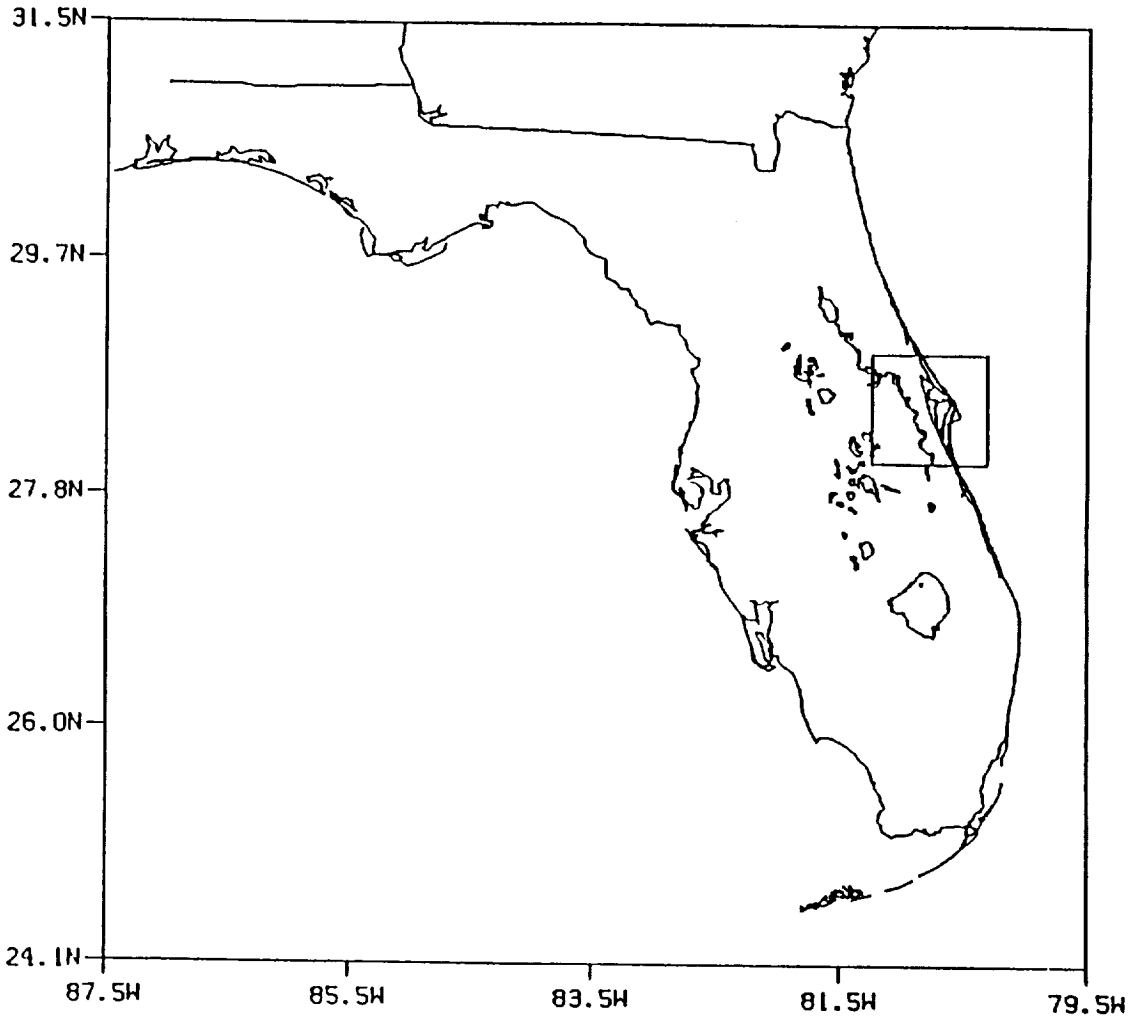

Figure 1a: Map of Florida with the CaPE study area outlined.

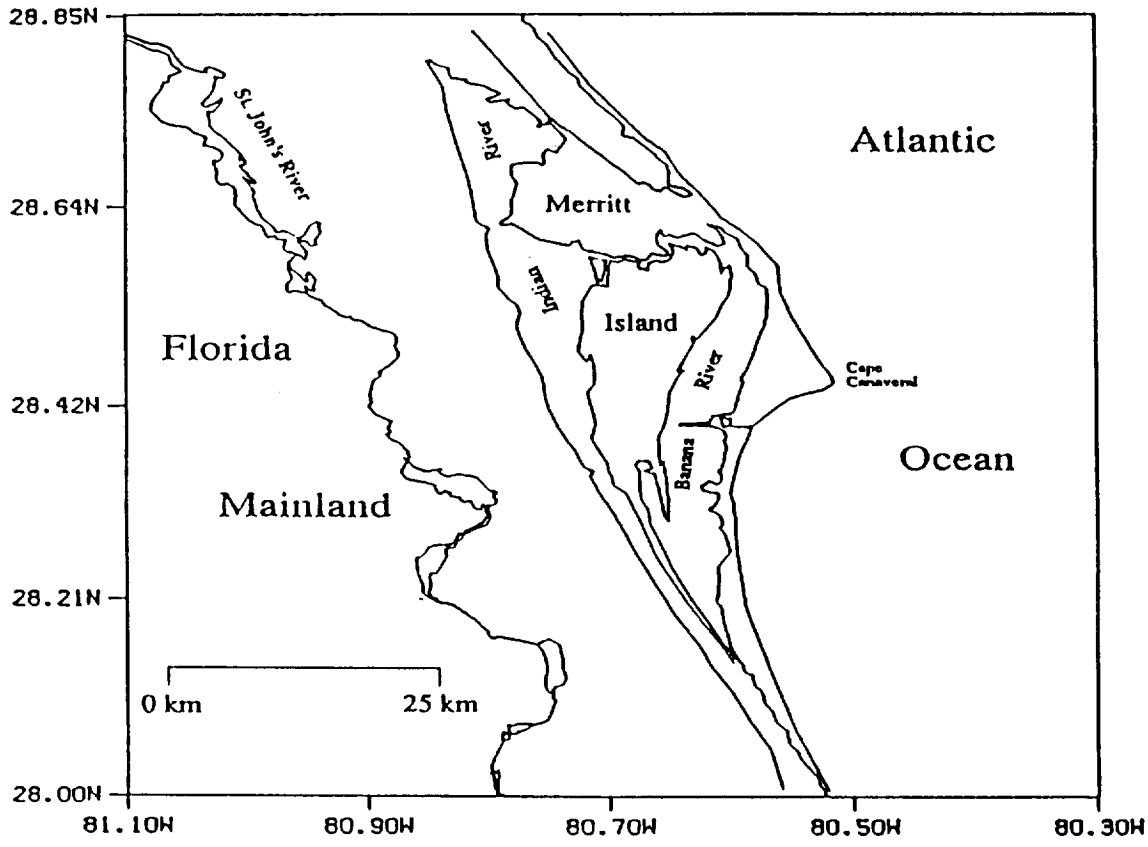

Figure 1b: Map of the CaPE study area with geographical features labeled.

sensors. Various types of shortwave, longwave and microwave satellite measurements were collected and added to the database. Figure 2 is an enlargement of the CaPE area in Figure 1(a), showing the stations for each network deployed, and the locations of the other types of instrumentation (Foote, 1991). The National Center for Atmospheric Research (NCAR) deployed 47 Portable Automated Mesonet (PAM) Stations around the CaPE area. At five minute intervals, these stations recorded wind direction and speed at a height of 9 meters in addition to surface rainfall. KSC had a pre-existing operational mesonet of 52 wind towers mounted at 16.5 meters with wind direction and speed recorded as 5-minute averages. A seven-station surface energy budget mesonet was also deployed. The Florida State University (FSU) Surface Radiation and Energy Budget Stations (SREBS), the University of Georgia (UG) flux measuring systems, and the National Aeronautical and Space Administration/Marshall Space Flight Center (NASA/MSFC) Bowen ratio and eddy correlation systems are marked by large F's in Figure 2. The FSU sites are the only flux sites on Merritt island. The instrumentation at these sites were designed to retrieve all major components of the surface energy budget (Smith et al. 1993).

An upper-air sounding network encompassing much of the CaPE study area was also in operation. The NCAR Cross-Chain LORAN Atmospheric Sounding System (CLASS) was employed at six locations and subsequently launched approximately 800 soundings during the experiment. The Cape Canaveral Air Force Station (CCAFS) also released radiosondes in addition to constant volume Jimspheres. The Jimspheres were tracked by radar to provide high resolution upper air wind measurements. The National Weather Service (NWS) office in Ruskin, just south of Tampa Bay, and Lowell University's site in

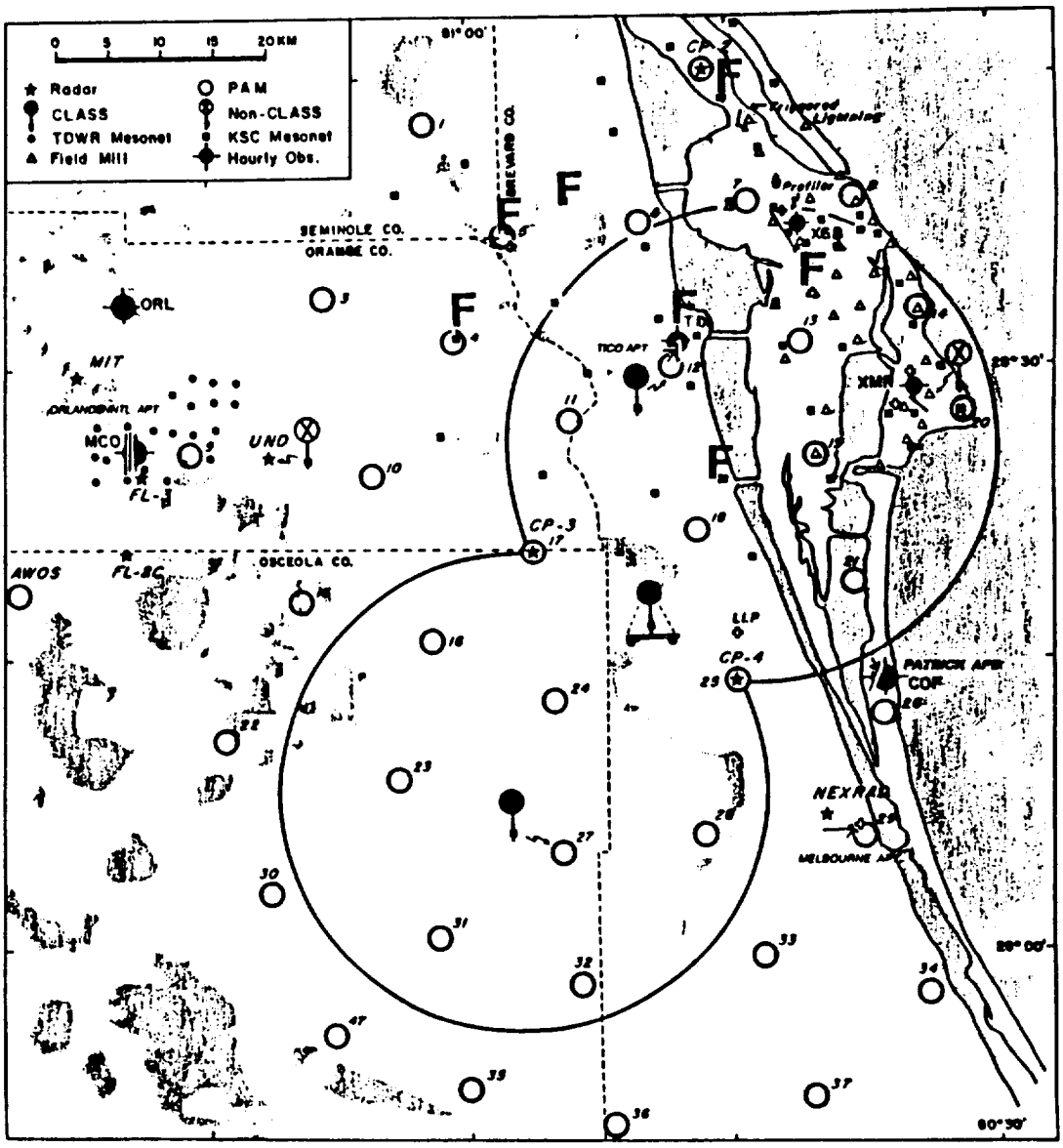

Figure 2: Close-up of the CaPE study area with the different networks indicated by the different symbols as noted by the key in the upper left hand corner. The FSU Flux sites are the two large F's in the eastern most part of the image. (Foote, 1991)

Orlando also gathered radiosonde data.

Researchers participating in CaPE also had access to radar data from several different sources. A total of six radars were dedicated to the project with four additional ones providing support when possible. NCAR provided 2 Doppler radars and 1 matched beam, dual wavelength and dual polarized radar (the S/X band multi-paramter CP-2 system). The New Mexico Institute of Mining and Technology provided 1 dual polarization X band radar. There were also mobile airborne radar units, 1 ground based and 1 airborne. The airborne unit was a Lockheed Orion aircraft operated by the National Oceanographic and Atmospheric Administration (NOAA). It was equipped with a horizontally scanning non-coherent radar in the lower fuselage and a vertically scanning Doppler radar in the tail section. The ground based mobile radar was a 3-mm pulsed coherent unit with full polarimetric and Doppler capabilities operated by the University of Massachusetts. Four additional weather radars in the south Florida area provided coverage as time and current weather permitted. These radars were: (1) WSR-88D at Melbourne; (2) WSR 74C at Patrick AFB; (3) MIT Lincoln Laboratory FL-2C C-band Doppler near Orlando; and (4) the University of North Dakota C-band Doppler, also near Orlando.

Eight research aircraft with various instrumentation were used during CaPE. NCAR flew a Beechcraft King Air 200 for low level mapping and cloud penetration, a Schweizer SGS 2-32 Sailplane for cloud penetration and a Cessna 180 to tow the sailplane. NASA supplied a Learjet 28/29 for overflights and cloud penetrations, a Lockheed ER-2 for remote sensing and high altitude overflights, and a Saberliner T-39 for remote sensing and overflights. The University of Wyoming flew an additional Beechcraft King Air 200 for low level mapping and cloud penetration. The South Dakota School of Mines and

Technology flew a North American T-28 for storm and cloud penetrations, and NOAA flew a Lockheed Orion WP-3D (P-3 radar) for cloud penetrations and dual Doppler scans.

Various agencies recorded satellite data during CaPE, including FSU and NASA/MSFC. The principle satellite data used in this study were derived from the GOES-7 geosynchronous satellite. The GOES-7 primary instrument is the Visible and Infrared Spin-Scan Radiometer (VISSR) which produces day and night infrared images and daytime visible images. The VISSR Atmospheric Sounder (VAS) also provided 6.7 μm measurements that can be used to calculate mid-tropospheric water vapor content. The NOAA polar orbiting satellites equipped with the Advanced Very High Resolution Radiometer (AVHRR) provided data at one kilometer resolution of the CaPE area and at four kilometer resolution at a global scale. The French Systeme Pour l'Observation de la Terre (SPOT) satellite provided three images of varying cloud cover during the experiment with its High Resolution Visible (HRV) imager (20 meter footprint size). In addition, a limited data set was made available from the People's Republic of China based on their sun synchronous Earth Resources Satellite carrying a Multi-Spectral Scanner sensor.

2.0 Description of Data Sets

Five of the data sets collected during CaPE were used in this analysis; (1) the CCAFS upper air soundings; (2) the NCAR PAM mesonet wind data; (3) the KSC mesonet wind data; (4) the FSU SREBS data; and (5) the GOES visible satellite imagery archived by the FSU-DRGS system.

2.1 Radiosonde Data

The CaPE rawinsonde network was designed to study both the small and large scale aspects of central Florida weather. The CaPE rawinsonde network consisted of six fixed and one mobile NCAR Cross-Chain LORAN Atmospheric Sounding Systems (CLASS), the Cape Canaveral Meteorological Sounding System (MSS), the National Weather Service launch site in Tampa, and the Lowell University sounding system located at the Orlando Airport.

A CLASS sounding system uses the Vaisala RS-80L LORAN radiosonde to profile temperature, pressure, humidity, and winds. Approximately 800 CLASS soundings were released during CaPE.

The MSS soundings used a VIZ radiosonde and tracking antenna for elevation levels. These soundings were released from the Cape Canaveral Air Force Station (CCAFS) balloon facility Monday through Friday three times a day at 1015, 1800 and 2215 UTC. During the weekend they were released twice daily at 1015 and 2215 UTC. These soundings consisted of vertical profiles of temperature, pressure, relative humidity, wind speed and direction. All data were processed by the USAF into 100 foot resolution. Only the CCAFS soundings were utilized in this study.

2.2 Portable Automated Mesonet Station Data

During CaPE, NCAR deployed 47 second generation PAM II stations on Merritt Island and the adjacent mainland (See Figure 3). These stations were used to collect one-minute averages of rainfall, temperature, pressure, wind speed and direction. A select few of the 47 stations (11) also recorded direct solar radiation data while 8 more of the 47 stations collected surface temperature and soil temperature at 10 and 50 cm depths. The wind measurements were taken at 9 meters using an orthogonal-array anemometer system. The rain gauge was a standard tipping bucket type. The data were transmitted every 3 minutes to the GOES satellite and from there transmitted to the CaPE Field Operations Center. Table 2 is a list of the PAM sites by identification number also giving the position of each tower. After reviewing the data collected at the PAM II stations, NCAR personnel made the decision that rain measurements from PAM sites 1, 11, 32, and 36 had technical problems during the experiment and that the rainfall data at these stations should be considered questionable. These stations were therefore excluded from any calculations presented here.

2.3 Kennedy Space Center Mesonet Station Data

The United States Air Force (USAF) and KSC maintain and operate a network of 52 instrument towers in the vicinity of Cape Canaveral (See Figure 3). Wind speed and direction at all of the sites are measured by propeller anemometers at a height of approximately 16.5 meters (54 ft). Some of the towers measure wind speed and direction at other levels above 16.5 meters, as well as at the 16.5 meter level. Air temperature is also measured and recorded at 44 of the 52 sites while 21 of the sites record humidity. Only one of the 52 sites records pressure and none of the KSC/USAF sites record rainfall. The data were averaged over five minute periods for the duration of CaPE. One of the KSC

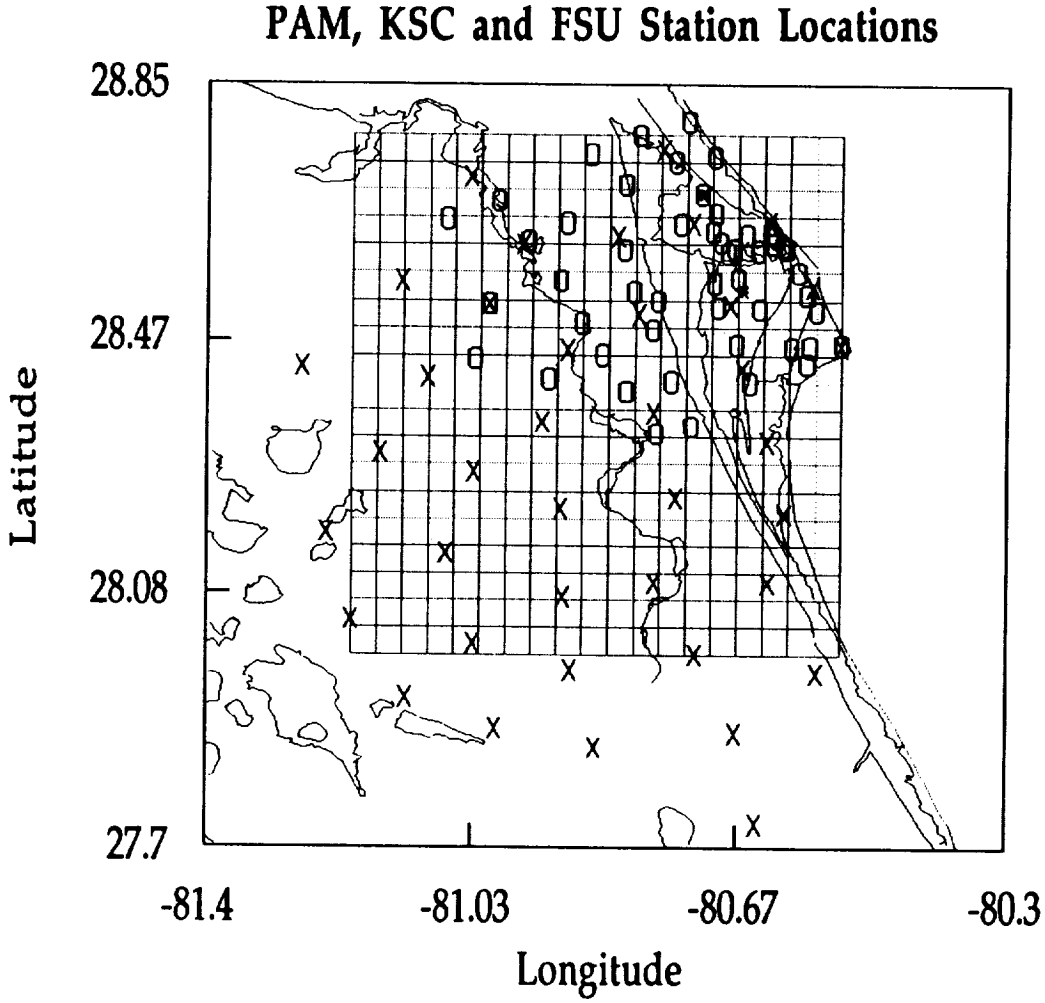

Figure 3: Similar to 2 but with the bivariate spatial interpolation grid overlaid on top of the area. X's are PAM stations, O's are KSC stations and * are the two FSU flux sites.

Table 2: PAM station identification numbers and the station locations.

Station	Latitude	Longitude	Station	Latitude	Longitude
PAM01	28.7133	-81.0367	PAM02	28.7531	-80.7714
PAM03	28.5569	-81.1314	PAM04	28.5217	-81.0103
PAM05	28.6111	-80.9650	PAM06	28.6225	-80.8336
PAM07	28.6419	-80.7300	PAM08	28.6436	-80.6253
PAM09	28.4283	-81.2689	PAM10	28.4117	-81.0947
PAM11	28.4531	-80.9028	PAM12	28.5064	-80.8047
PAM13	28.5194	-80.6794	PAM14	28.5489	-80.5675
PAM15	28.2975	-81.1600	PAM16	28.2692	-81.0314
PAM17	28.3433	-80.9361	PAM18	28.3594	-80.7833
PAM19	28.4256	-80.6617	PAM20	28.4597	-80.5275
PAM21	28.3133	-80.6269	PAM22	28.1767	-81.2347
PAM23	28.1444	-81.0683	PAM24	28.2122	-80.9117
PAM25	28.2292	-80.7533	PAM26	28.2039	-80.6039
PAM27	28.0789	-80.9083	PAM28	28.0994	-80.7817
PAM29	28.0994	-80.6253	PAM30	28.0442	-81.1994
PAM31	28.0083	-81.0306	PAM32	27.9689	-80.8967
PAM33	27.9911	-80.7253	PAM34	27.9636	-80.5608
PAM35	27.8806	-81.0000	PAM36	27.8519	-80.8628
PAM37	27.8736	-80.6708	PAM38	28.1894	-82.6244
PAM39	28.2247	-82.1603	PAM40	28.2417	-81.6500
PAM41	29.0619	-82.3711	PAM42	29.1942	-81.0522
PAM43	27.7372	-80.6406	PAM44	27.7000	-82.4000
PAM45	28.7306	-81.8733	PAM46	27.6708	-81.5928
PAM47	27.9275	-81.1250			

wind towers was co-located with an NCAR PAM II site (PAM II 20). Table 3 provides a list of the KSC Mesonet sites by identification number also giving the geographical positions of each tower. The locations of the KSC towers is also shown in Figure 3.

2.4 Calculation of Divergence From the PAM and KSC Networks

The Cape Canaveral area of Central Florida extends from 80.50 to 81.30 West longitude and from 27.70 to 28.80 North latitude. This is the domain covered by the PAM network. This is also the basic CaPE study area as seen in Figure 3. The smaller KSC station array, which is considered to be a convective scale network, is a subset of the larger PAM area, and is approximately bounded by -80.50 to -81.10 West longitude and 28.30 to 28.80 North latitude. The smaller NASA network has a much higher density of stations than the larger NCAR network. Hereafter the NCAR network will be referred to as the PAM network, whereas the NASA network will be referred to as the KSC network.

The calculation of low level divergence is accomplished using a grid consisting of 20 X 20 elements of size 3.5 by 4.5 km^2 and was designed such that both the PAM and KSC networks were contained within the 70 km by 90 km grid. It may be pointed out here that the size of the PAM mesonetwork is comparable to the size of other mesonetworks deployed elsewhere; for example the FIFE 1987-1989 network and the HAPEX-2 Sahel network near Niamey, Niger in West Africa. Figure 3 shows the CaPE area with the overlaying grid and the PAM and KSC stations. The wind data was processed using the NCAR bivariate interpolation scheme. Appendix 1 provides a description of this scheme. The wind data from both networks were processed for every five minute period of the entire 40 day period of the CaPE experiment. The wind data were reported in terms of u and v components. The components are separately interpolated to

Table 3: KSC station identification numbers and station locations. Shaded boxes indicate that the station was not operational during CaPE.

Station	Latitude	Longitude	Station	Latitude	Longitude
K0001	28.4338	-80.5734	K0003	28.4635	-80.5283
K0005	28.5130	-80.5613	K0108	28.5359	-80.5748
K0110	28.5697	-80.5864	K0112	28.6141	-80.6203
K0303	28.4600	-80.5712	K0311	28.6027	-80.6414
K0313	28.6256	-80.6571	K0403	28.4581	-80.5945
K0412	28.6063	-80.6739	K0415	28.6586	-80.6998
K0506	28.5158	-80.6400	K0509	28.5623	-80.6694
K0714	28.6431	-80.7482	K0803	28.4632	-80.6702
K0419	28.7366	-80.7547	K0417	28.6869	-80.7192
K1007	28.5272	-80.7793	K0709	28.5544	-80.7018
K0805	28.5184	-80.6962	K0917	28.7014	-80.8228
K1012	28.6056	-80.8248	K1108	28.5421	-80.8118
K0513	28.6308	-80.7027	K0511	28.5986	-80.6816
K0512	28.6160	-80.6931	K0393	28.6105	-80.6069
K0394	28.6057	-80.6016	K0397	28.6294	-80.6235
K0398	28.6248	-80.6182	K2016	28.6489	-81.0693
K1617	28.6762	-80.9987	K0819	28.7464	-80.8707
K0421	28.7755	-80.8043	K0022	28.7975	-80.7378
K1612	28.6173	-80.9581	K1215	28.6445	-80.9034
K0019	28.7435	-80.7005	K2008	28.5231	-81.0099
K1609	28.5583	-80.9132	K2202	28.4417	-81.0291
K1605	28.4960	-80.8843	K1500	28.4114	-80.9284
K1502	28.4475	-80.8538	K1204	28.4843	-80.7856
K9001	28.3932	-80.8212	K1000	28.4079	-80.7604
K9105	28.3288	-80.7802	K9404	28.3382	-80.7321
K0300	28.4048	-80.6519			

the grid points using the interpolation scheme. The result is 400 points of u and v data from which a value of divergence at the center of each individual grid box can be calculated. Selected parts of the grid that were data sparse were eliminated from calculations. Figure 4 shows the gridded area with the eliminated boxes shaded for the PAM network. Figure 5 shows the gridded area with the eliminated boxes shaded for the KSC network. Using a simple analytical wind field, the layout of the stations was tested under the interpolation scheme and found to produce satisfactory results. A description of this calibration scheme and the testing procedures can be found in Appendix 2.

For the purpose of analyzing the interactions between the various small scale circulations expected in the Cape Canaveral area, the divergence grid is divided into regions based on the boundaries between land and water. This is done for each of the two networks. The PAM mesoscale network is divided into five regions. Table 4 shows the five regions and the relative number of grid boxes enclosed in each region. Figure 6 shows the PAM divisions based on surface topography. The smaller KSC network is likewise divided into four regions. Table 5 describes this division. Figure 7 shows the smaller convective scale KSC network broken down into regions. In both cases there is a final region which is made up of the sum of all the sub-regions.

In order to ensure that the calculations were providing realistic results, area-averaged divergence was calculated over both networks for the 40-day experimental period with the results over Merritt Island inter-compared. Figure 8 shows the mean diurnal area-averaged divergence for the PAM network plotted against the mean diurnal area-averaged divergence from the KSC network. The high correlation ($r = 0.9404$) between the two variables indicates a consistency between the two calculations using the two independent data sets.

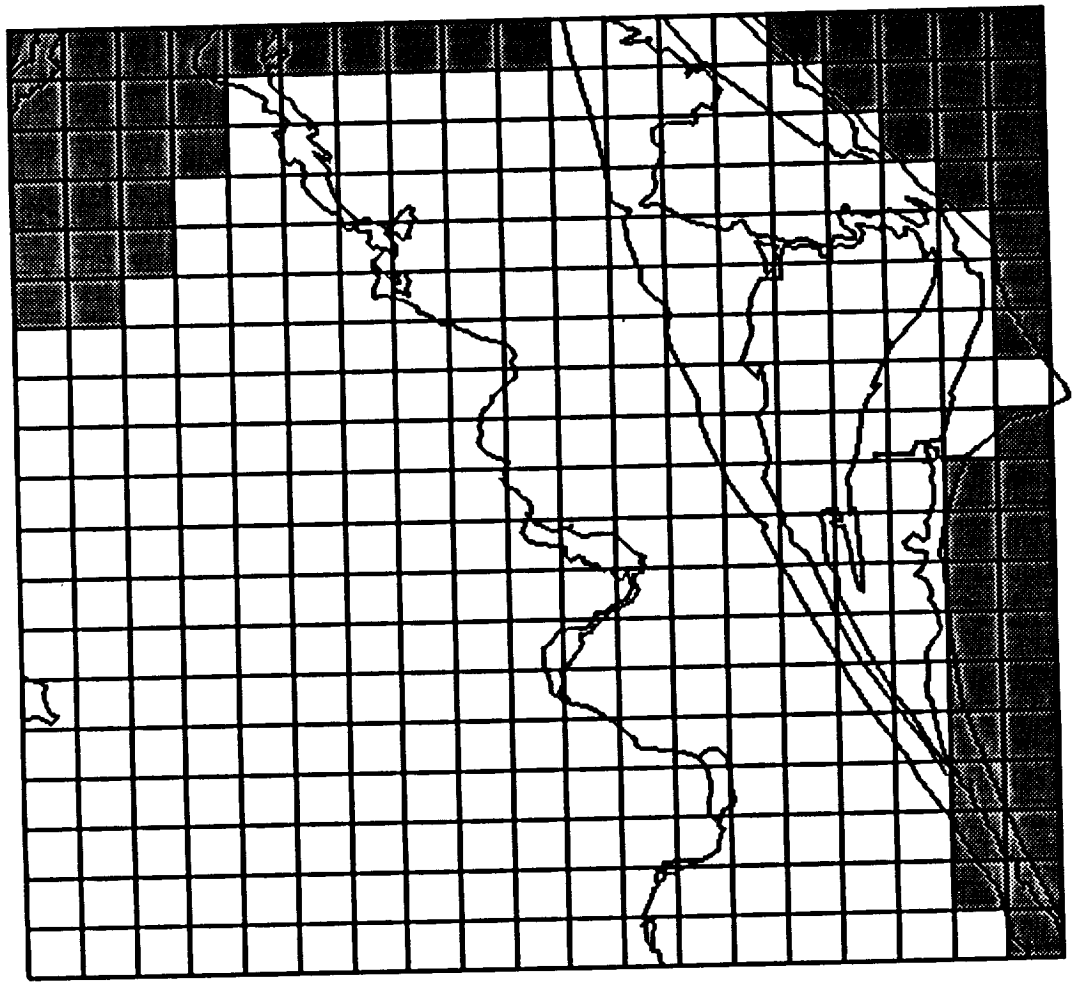

Figure 4: Gridded CaPE study area for the PAM network. Shaded boxes indicate that these areas were eliminated from the area-averaged divergence calculations using the PAM data set.

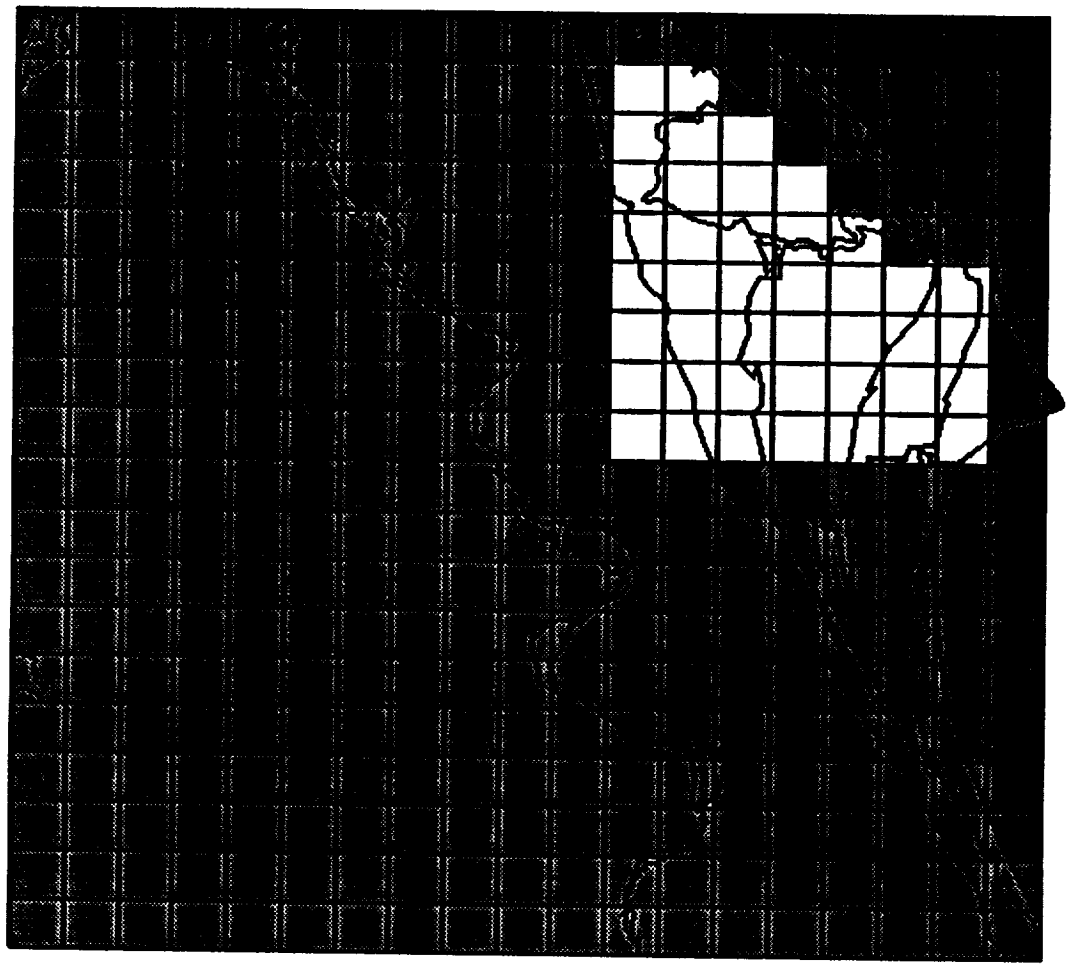

Figure 5: Gridded CaPE study area for the KSC network. Shaded boxes indicate that these areas were eliminated from the area-averaged divergence calculations using the KSC data set.

Table 4: PAM block distribution.

Region	Number of Blocks
Mainland	25
Indian River	15
Merritt Island	16
Banana River	3
Total Network	298

PAM Divisions

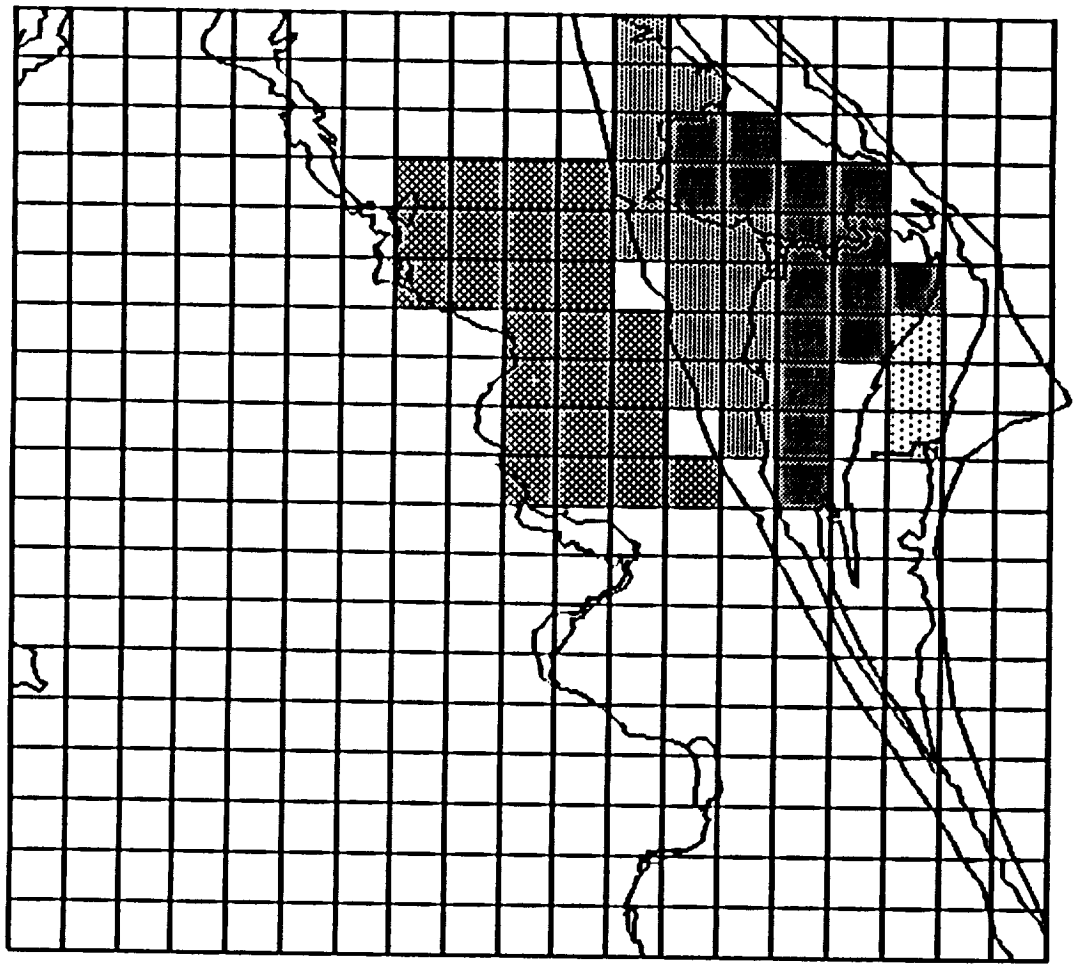

Figure 6: Divisions in the PAM network as broken down by topographical features in the CaPE study area. Areas include the Mainland, the Indian and Banana Rivers, and Merritt Island.

Table 5: KSC grid block distribution

Region	Number of Blocks
Indian River	14
Merritt Island	15
Banana River	36
Total Network	42

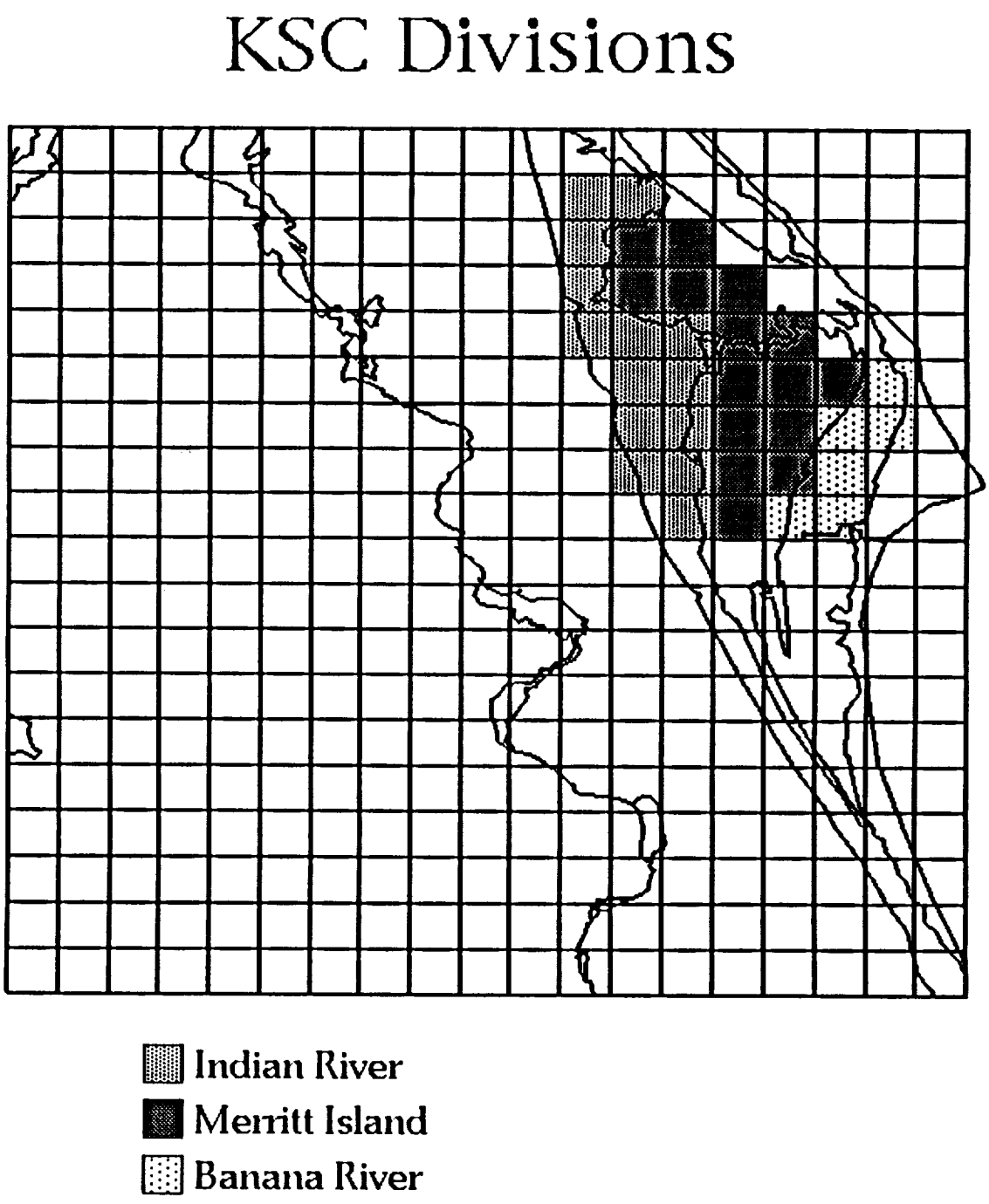

Figure 7: Divisions in the KSC network as broken down by topographical features in the CaPE study area. Areas include the Indian and Banana Rivers and Merritt Island.

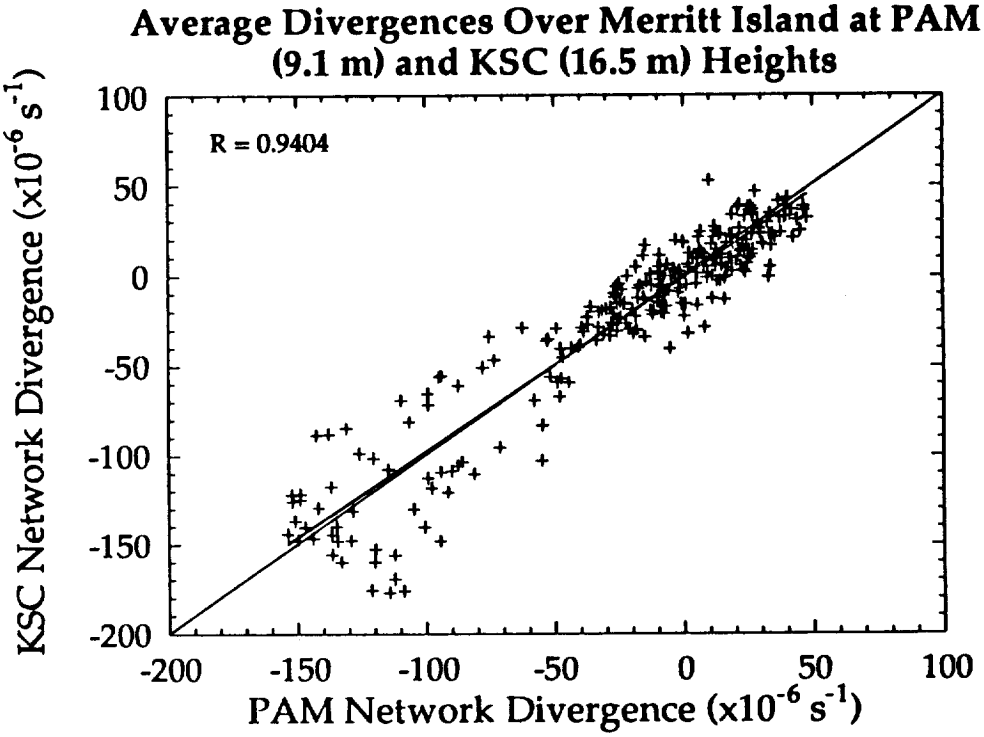

Figure 8: 40-day averaged KSC network calculated area-averaged divergence over Merritt Island compared to 40-day averaged PAM network calculated area-averaged divergence. The line from the upper right corner to the lower left corner is the 1 to 1 fit.

2.5 Surface Radiation and Energy Budget Station Data

The Florida State University Surface Radiation and Energy Budget System (SREBS) is a self contained measurement system that is similar to that used during the First ISLSCP Field Experiment in 1987 and 1989. For a complete and detailed description of the data collection procedures and calculations of the surface fluxes using the FSU-SREBS, see Smith et al. (1992). The system has been designed to retrieve all major components of the surface radiation and total energy budget along with other measured and derived parameters which describe the meteorological and hydrological properties of the surface, sub-surface, and atmospheric surface layer. The system consists of five major sub-systems that are designed to monitor specific components of the near-surface environment. These are: (1) the Bowen Ratio sub-system; (2) the radiation sub-system; (3) the meteorological sub-system; (4) the soil monitoring sub-system; and (5) the data-acquisition electronics sub-system. Figure 9 provides a schematic diagram of the SREBS station.

The Bowen Ratio system uses fine wire unshielded thermocouples along with a chilled mirror dew point hygrometer to measure surface layer temperature and moisture gradients. These sensors are used to evaluate the surface Bowen Ratio, which partitions the available energy (i.e., net radiation minus soil heat flux) into sensible and latent heating. This system is called a Dew-10 and is manufactured by Campbell Scientific, Inc. (CSI) in Logan, Utah. The unit consists of two sensor arms which are suspended at two levels over the plant canopy, and on which are extended copper-constantan fine-wire thermocouples which sense fluctuations in ambient air temperature. Intakes on each arm are used to feed air to the hygrometer of the unit where the dewpoints at the two levels are calculated. The measurements thus establish temperature

Florida State University Surface Radiation and Energy Budget Station

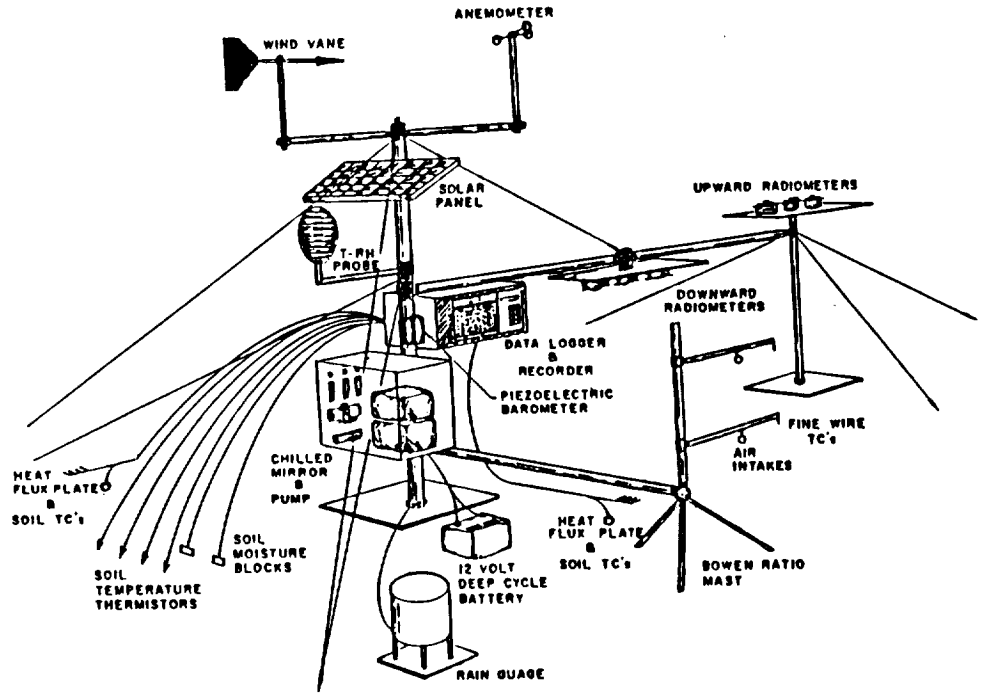

Figure 9: Schematic Diagram of the FSU Surface Radiation Energy Budget Stations (SREBS) deployed during CaPE, diagramming all major subsystems.

and dewpoint at two levels above the canopy from which the temperature and moisture gradients are obtained. The intakes alternate on three minute cycles, drawing air into the upper and lower mixing chambers within the Dew-10 main housing unit where it is allowed to reach an equilibrium temperature. The air is then pumped into the mirror chamber where it is cooled until saturation on the mirror occurs. Condensate formed on the mirror is detected by a reduction in reflectance of a collimated light source pointed at the mirror; the temperature at which this occurs is by definition the dew point temperature. The system is susceptible to condensation forming in the feed lines in situations of very high humidity. During CaPE, early morning (before 900 AM EDT) and late evening (after 1100 PM EDT) humidities were often near 100%. By use of an independent hygristor mounted nearby, the Dew-10 pump was toggled off automatically when the humidity rose above a set high humidity level and then reactivated when the humidity fell below the cutoff level. As a result, during most of the early mornings and early evenings, the so called transition periods, atmospheric moisture data are not available from the SREBS stations. The hygristor used to determine when to toggle the Dew-10 pump on and off could not be used in the flux calculations because of its slow response time.

The radiation system consists of upward and downward facing radiometers set approximately two meters above ground level. There was an average depth of 25 cm of shrub below the radiometers. The radiometers consist of matched pairs of broad band pyranometers and pyrgeometers, along with a pair of filtered pyranometers. The pyranometers are temperature compensated Eppley Precision Spectral Pyranometers (PSPs) using Suprasil-W domes to block wavelengths beyond 3.5 μm. The filtered pyranometers can be used with Schott colored glass outer domes to filter out shortwave radiation below one of five

selected wavelengths (.395, .495, .610, .695, .780 μm). A 0.695 μm filter was used throughout CaPE. The pyrgeometers are Eppley Precision Infrared Radiometers (PIRs) using polished silicone domes which block transmission of radiation below 3.5 μm. These radiometers are utilized to determine net shortwave radiation, net near-infrared radiation, net total solar radiation, net longwave radiation, and total net radiation, as well as the individual upwelling and downwelling components.

The meteorological system consists of a three cup anemometer, windvane, barometer, solid state temperature-humidity sensor, and a tipping bucket raingauge. The vane and anemometer were set three meters above ground level during CaPE. The temperature sensor and the humidity sensor were secured to the main mast of the tripod supporting the wind instruments at a height of 2.75 meters. A 0.254 mm resolution tipping raingauge was placed at ground level in an open area within the general site area.

The soil monitoring sub-system consists of soil temperature, soil moisture and soil heat flux sensors. These instruments are used to provide total soil heat flux and vertical temperature and moisture gradients within the first 40 cm of soil. Two heat flux plates wired in parallel are used to determine the 5 cm soil heat fluxes. There are also two sets of four leg thermocouple probes placed parallel above the soil heat flux plates for the calculation of ground heat retention. In addition, there are four soil thermistors placed nominally at 2, 8, 20, and 40 cm depths to provide detailed soil temperature profiles. Two gypsum soil moisture blocks placed at 5 and 20 cm depths provide a continuous record of soil moisture and its near surface and deep components.

The data acquisition system is a Campbell Scientific CR-7 datalogger. The datalogger continuously monitors all sensors, recording averages of sensor

samples at 6 minute intervals on a standard cassette tape. The datalogger is a totally portable, weather resistant and self-contained unit. The CR-7 itself is contained in a two piece fiberglass enclosure unit utilizing C-clamp type closing devices and a thick rubber gasket between the two halves. The datalogger is then further encased by mounting the fiberglass back piece containing the datalogger itself in a water-resistant steel enclosure to provide further protection from the high levels of humidity and rain associated with summertime conditions in central Florida. The outer enclosure was also gasket sealed, using turnscrew locks to seal out moisture. During the pre-experiment testing phase of the equipment, it was noticed that the dark color of the outer enclosure was causing abnormally high temperatures within the datalogger. Painting the entire surface of the box with a high gloss white paint eliminated this problem. A 12 volt marine battery powers the Dew-10 pump, the flow regulators and intake valve switches. A 10 watt unregulated solar panel is used to recharge a battery pack within the datalogger while a 20 watt unregulated solar panel is used to recharge the 12 volt external battery.

2.6 The FSU GOES-7 Visible Satellite Data

Florida State University received and archived GOES images using the FSU Direct Readout Ground System (FSU-DRGS) for the entire period of CaPE (Smith and Fuelberg 1989). The major portion of the satellite data collected during CaPE was composed of GOES-7 visible (0.5 to 0.7 μm) radiometric images at 30 minute intervals, which were used to calculate the average reflectance over the PAM and KSC surface wind networks during daylight hours throughout the experimental period. The area-average of reflectance was found on two different spatial scales; (1) a mesoscale area extending over the PAM network and which

covers an area of approximately 1500 km^2; and (2) a smaller, convective scale region bounded by the KSC anemometer network.

The visible reflectance observed by the satellite is calculated directly from the counts associated with each 1x1 km resolution pixel within a satellite image, and in accordance with the linear response characteristics of photomultipliers (E. Smith, personal communication, 1993). The reflectance, (R), is a function of solar zenith angle, (θ_o):

$$R(\Theta_o) = a_o + \frac{a_1 \pi C_L}{2 F_o \cos\Theta_o D^2} \quad (1)$$

where a_o is a bias value of 0.005, a_1 is the calibration coefficient (0.8188) and C_L is a linearized count (C) given by:

$$C_L = C^2\left(\frac{255.0}{3969.0}\right) \quad (2)$$

Here F_o is the spectral TOA solar constant between 0.5 and 0.7 μm (the spectral band sensed by the GOES-VIS instrument). D is the ratio of the mean earth-sun distance to the actual earth-sun distance which is a function of Julian day. The reflectance is therefore calculated as a function of digitized count, Julian day and solar zenith angle, which in turn is a function of the date, time of day, and position in the satellite image. The reflectance is found for every pixel over the two different mesonetwork areas and is related to the total cloud cover over each network. An average reflectance is then calculated over each network area. In addition to average reflectance, the spatial variance of reflectance samples is also calculated over each of the network areas.

By using the area-average image reflectance values in conjunction with the spatial variance of reflectance and the area-averaged surface wind divergence at corresponding times, a relationship between reflectance and surface wind divergence is derived, thus linking the surface wind activity to cloud coverage

estimated by satellite. The surface wind field is in turn linked to the magnitude of the surface flux, providing an indirect assessment of the relationships between cloudiness and the surface fluxes.

3.0 Sea Breeze Wind Field Analysis

In this section, the wind fields within the sea breeze convergence zones are examined. The connection between the low level wind fields and the upper-air flow is established from analysis of the CCAFS upper-air soundings. Then the PAM and KSC divergence is correlated with the soundings and with GOES visible imagery leading to the classification of days in terms of the local circulations over Merritt Island. An investigation of the formation, propagation and decay of the sea breeze convergence zones is discussed.

3.1 CCAFS Sounding Analysis

The initial stage of analysis was centered around examination of the experimental data on weekly time scales to determine if synoptic scale features would leave a detectable signal. This was done by compositing the daily soundings from CCAFS into a time-height cross section which considers all 40 days of the experiment. Analyses were performed based on the u and v components of the winds aloft and moist static energy departures from the averaged daily soundings. The average soundings used in the departure calculations were derived by calculating average soundings based on their release times (i.e., morning, midday or evening). Figures 10-12 show the wind component cross sections to a height of 18 km and the moist static energy cross-sections to 13 km.

The u component (Figure 10) shows a definite pattern throughout the experiment characterized by two prominent periods of deep easterly flow, one from the 18th through the 23rd of July, and the other from the 4th through the

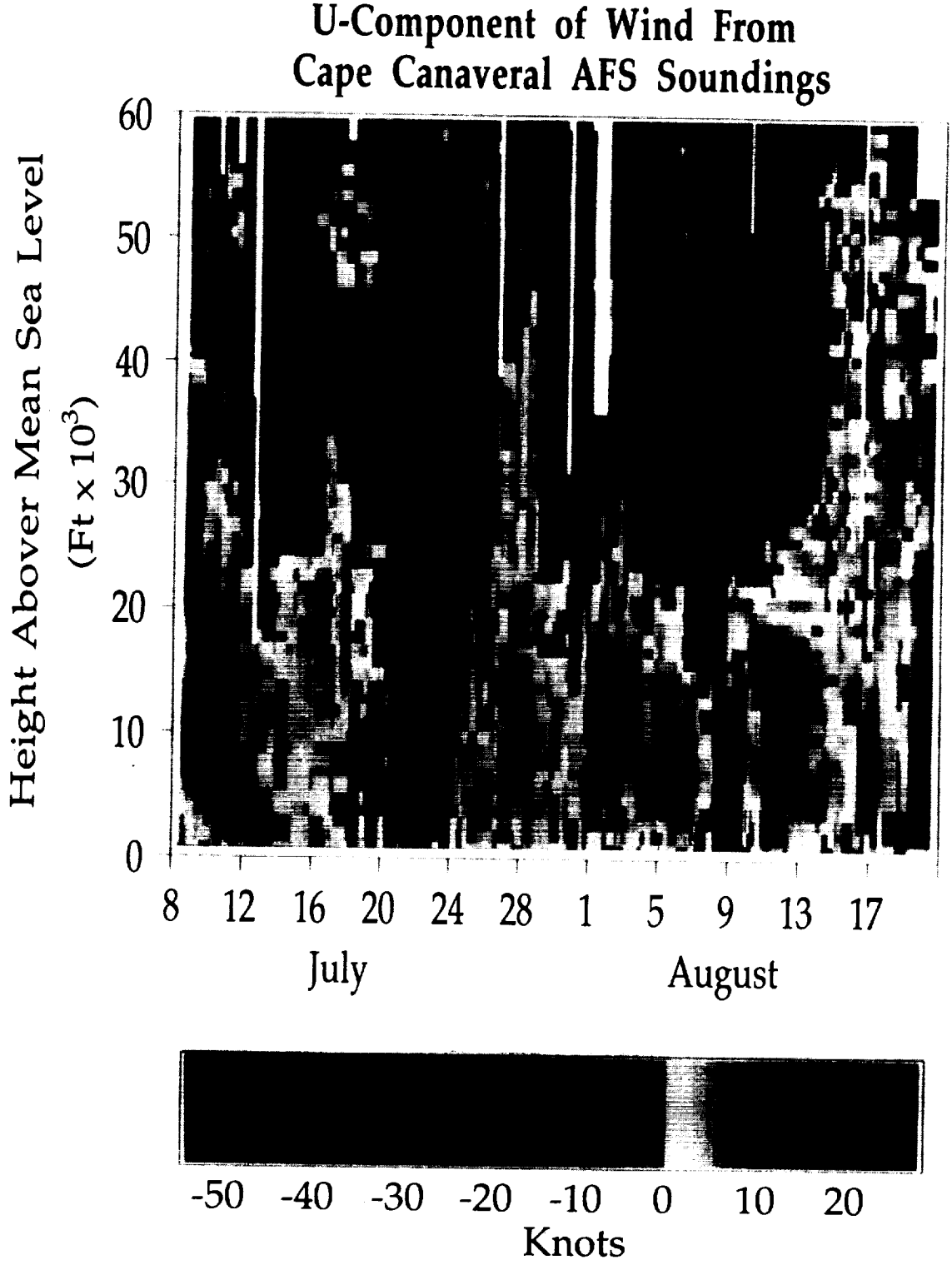

Figure 10: The 40-day time-height cross section of the u-component of wind as calculated from the CCAFS Soundings.

8th of August. The atmosphere from ground to around 7 kilometers shows three regimes of pronounced westerly flow, one from the 14th through 17th of July, the second from July 25th through the 4th of August, and the third from the 8th through the 15th of August. The period at the beginning of the experiment from the 8th to the 14th of July shows moderately deep westerly flow. During the last three days of the time series, the wind flow was dominated by Hurricane Bob as it moved north in the Atlantic. This period exhibits similar behavior to the first days of the experiment with deep westerlies from the 16th through 18th of August. The u component of the wind exhibits these modes more clearly than does the v component (Figure 11). The flow can be roughly described as southerly in the low levels and northerly in the upper levels. There are several periods where the northerly upper level flow is sufficiently dominant for surges to reach near the surface. This can be seen during the period centered around the 21st of July and the 10th of August. Under the influence of the hurricane, this flow pattern is reversed, with strong southerlies aloft and strong northerlies in the lowest 8 kilometers.

The periodic flow patterns apparent in the wind cross sections can also be discerned in the moist static energy (ζ_e) departure cross section (Figure 12). During a period of southeasterly flow from the 15th through the 24th of July, areas of negative departure are dominant in the levels above 3 km while below there is a region of positive departure indicating that these periods are more suppressed in terms of convective activity. During a period of southwesterly flow around the 26th of July, areas of positive departure are located above areas of negative departure indicating that this period experienced deep convective activity. This reversal of positive and negative gradients occurs throughout the experiment with the reversal occurring around the 3 km level. Large positive

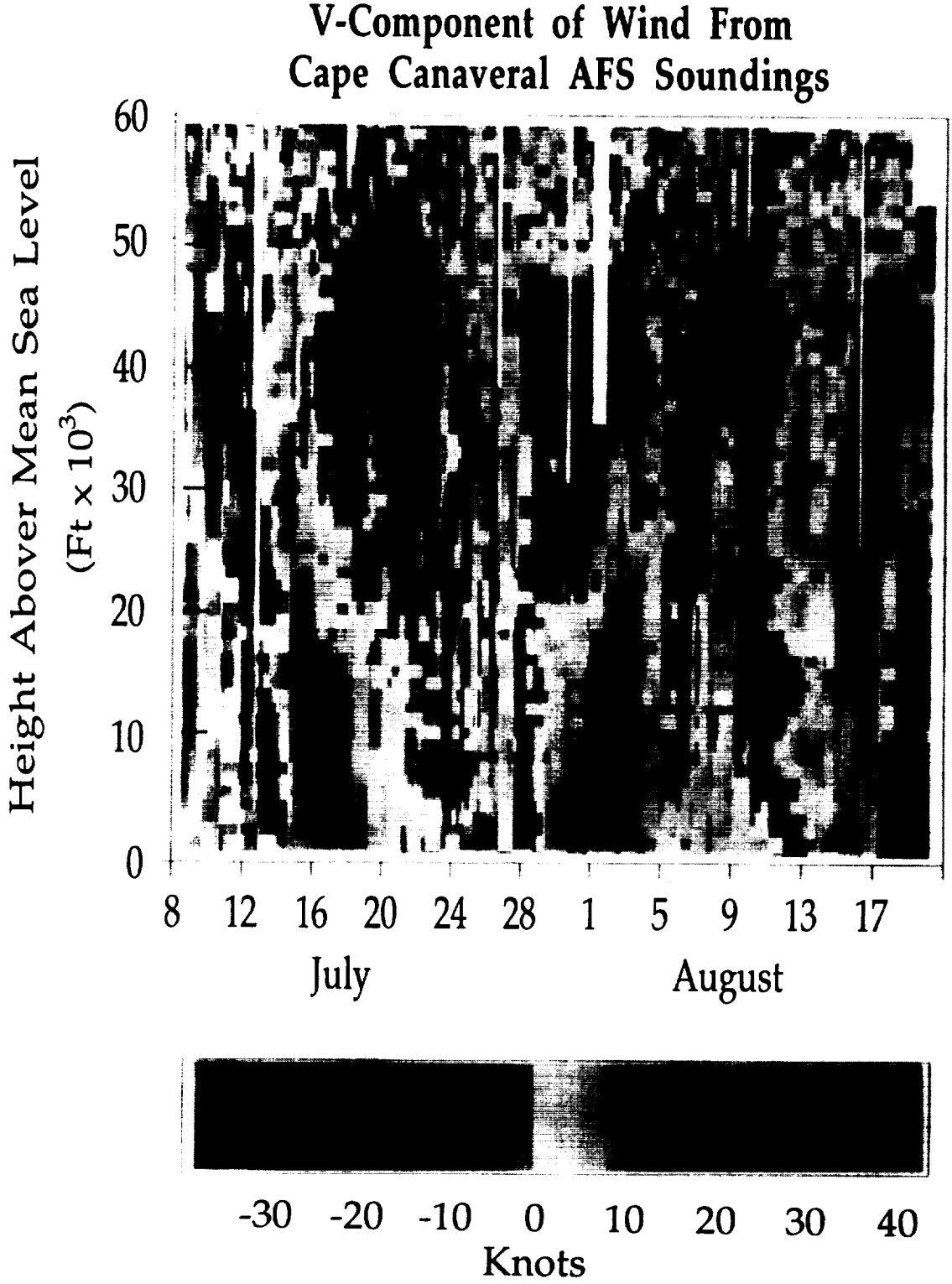

Figure 11: The 40-day time-height cross section of the v-component of wind as calculated from the CCAFS Soundings.

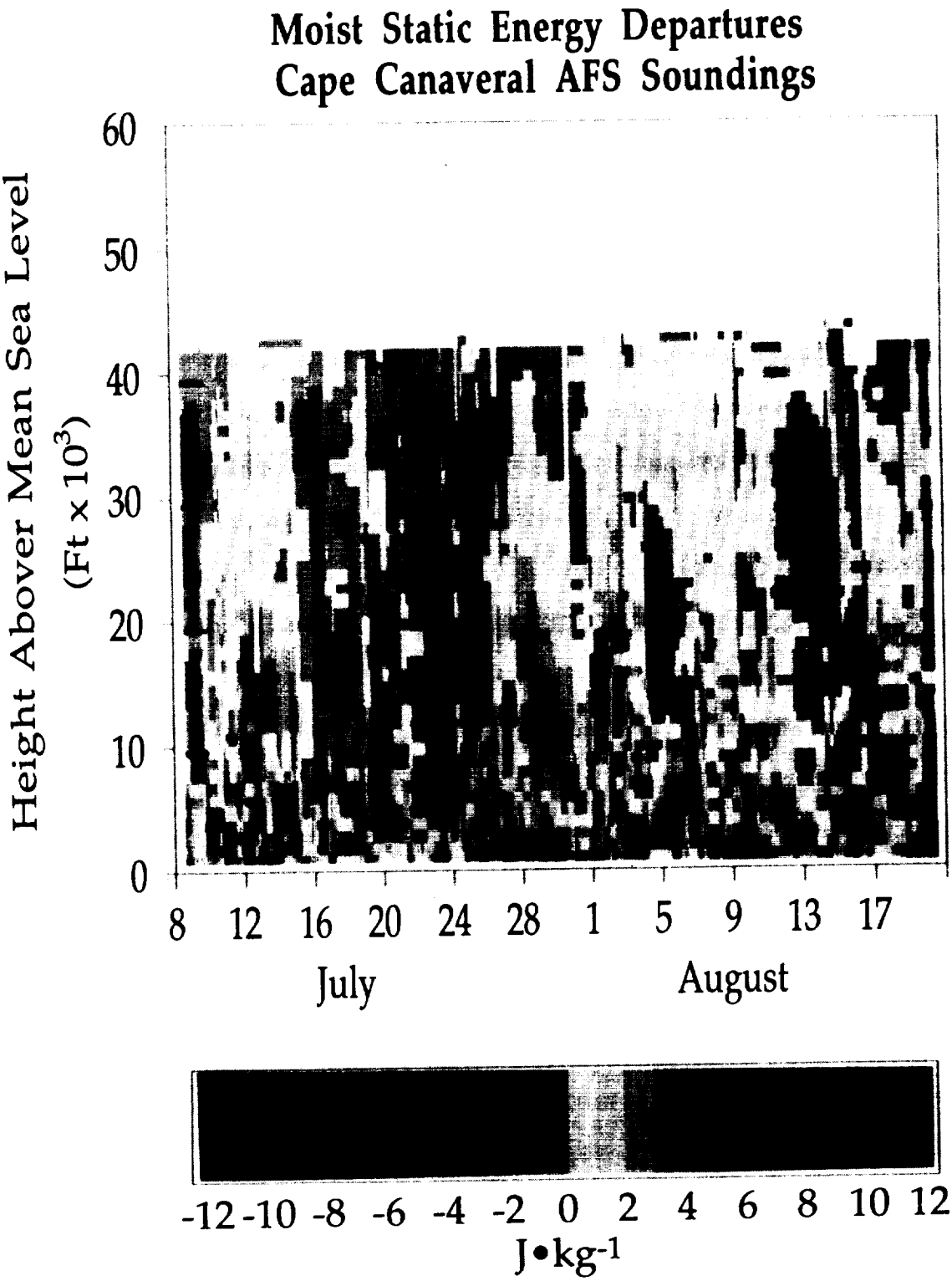

Figure 12: The 40-day time-height cross section of the departure from the 40-day mean of moist static energy as calculated from the CCAFS Soundings.

departures between 3 to 6 km around the 15th and 29th of July indicate periods of convective overturning.

Rainfall averages from the PAM network over the CaPE study area also fit the flow patterns suggested by the upper air cross-sections. Figure 13 shows the average hourly station rainfall over the PAM network during the experiment. The period from the 16th to the 24th of July is characterized by southeasterly flow aloft and ζ_e departures that indicate there should be little convective activity. The rainfall during this period is low compared to the periods of the experiment when southwesterly flow and ζ_e departures indicate that there could be convective activity, such as the 25th through the 30th of July. There is also a later period of lower rainfall between the 5th and 9th of August which is associated with deep easterly flow.

3.2 PAM and KSC Wind Field Analysis

Figures 14(a) and 14(b) show the 40 day averages of area-average divergence over the CaPE study area for the KSC and PAM networks, respectively. In both cases the total network average exhibits the behavior expected in a coastal area during the summer, that is, convergence over land during the day and divergence during the night. The PAM signals tend to be smoother than those from the KSC network due to the greater spacing between stations in the PAM Network. The KSC average is more convergent than the PAM because the KSC area is smaller. This is consistent with an area-averaged divergence calculation. However, the two networks share virtually identical areas for Merritt Island and indeed, show a very similar signal in the mean.

The Merritt Island signals for both networks demonstrate the classical sea breeze pattern for an isolated landmass. The flow over the island is divergent during the period from midnight to 0900 local daylight time (LDT) and then

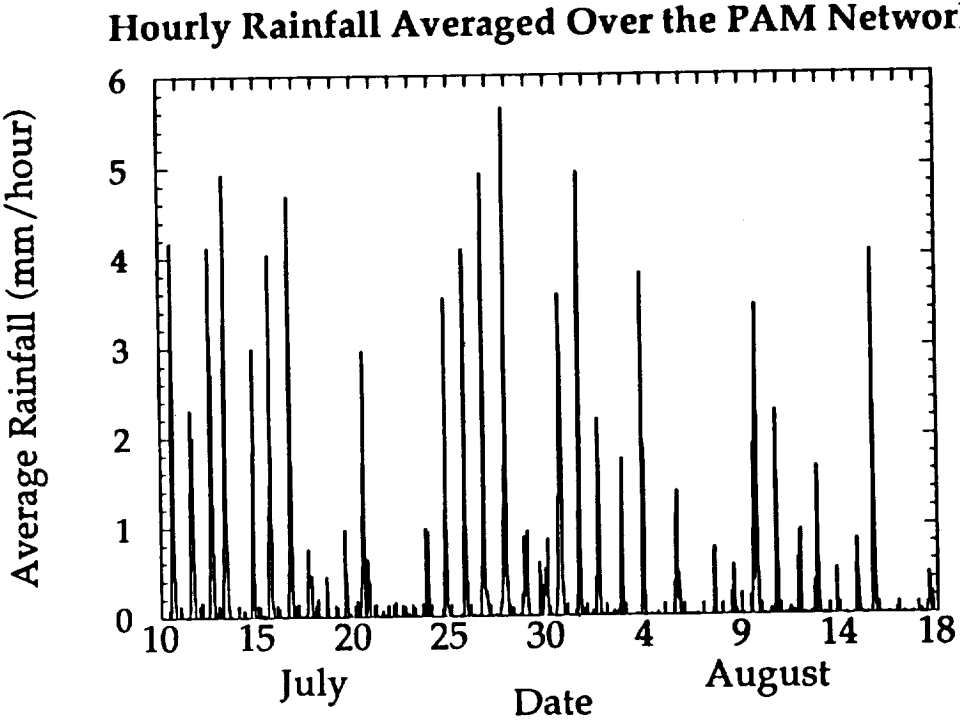

Figure 13: Hourly accumulated rainfall over the entire PAM network normalized to the number of reporting stations for the CaPE study period.

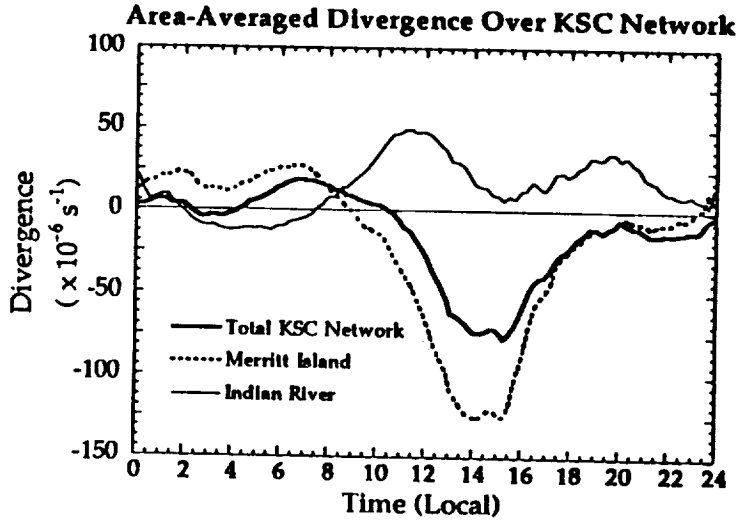

(a)

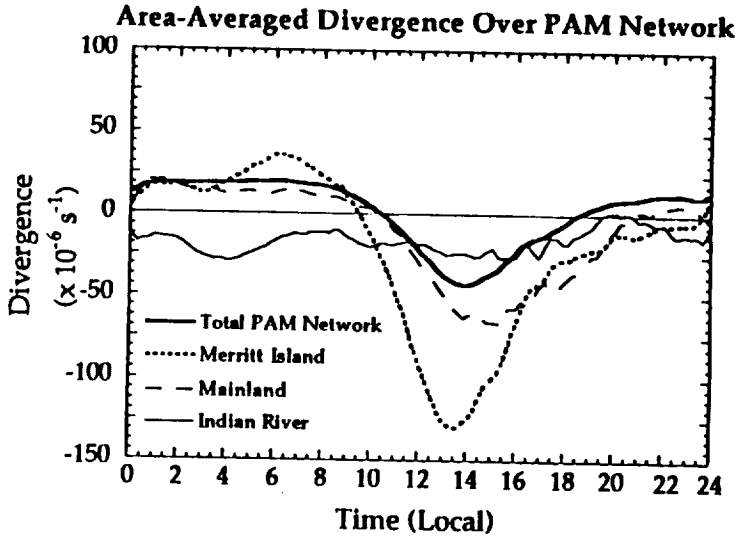

(b)

Figures 14(a) and 14(b): 40-day diurnal average of area-averaged divergence over the KSC mesonet (a) and PAM mesonet (b). Sub-grid areas displayed are Merritt Island (short dashed line), the Mainland (long dashed line), the Indian River (thin solid line), and the total KSC network (heavy solid line) as calculated from the KSC mesonet.

convergent the remaining hours of the day. Classical interpretation of this pattern implies that the air is rising over the island during the day and sinking over the island during the night. This is to be expected due to differential diurnal heating over the island-ocean system. The land mass heats more rapidly during the day than does the upper ocean layers so that the expanding and rising air mass is over the land. Conversely during the night, the water retains the absorbed heat and acts as a nocturnal heat source driving the land breeze circulation. The oceanic arm of the circulation is often seen in the visible satellite imagery as cumuliform clouds several kilometers out in the Atlantic ocean in the early morning where the convergence from the land breeze may initiate strong convection. Over either network, the strongest signals are over Merritt Island.

The Indian River demonstrates the expected behavior in the tighter KSC network, but not as well in the PAM network. This is not totally unexpected because of the lack of adequate resolution in the PAM mesonet along the river. In the KSC mesonet, the river breeze circulation acts out of phase with the Merritt Island circulation. The river is convergent during the nighttime hours from 0100 to 0800 LDT and divergent the remaining hours of the day. Classical interpretation of this secondary circulation system leads to the conclusion that air is rising over the river while it is sinking over the island during the nighttime, and sinking over the river while it is rising over the island during the daytime. Even though this classical pattern is missing from the PAM network because of station placement, the behavior of the river signal in this case can still be explained using a standard river breeze circulation theory. During the nighttime, the Indian River is convergent in the PAM network. It is also convergent during the day, however, it is somewhat less convergent than the island signal, therefore it can be interpreted as an area of relative divergence as compared to the island

signal. It is important to note that the PAM and KSC networks form completely independent data sets which show similar results.

3.3 GOES Visible Imagery and Low Level Divergence

In this section the connection between visible reflectance calculated from half hourly high resolution (1x1 km) GOES-VIS imagery and surface wind divergence measured in the networks is discussed. The hypothesis is that when the low level wind flow is converging under favorable thermodynamic conditions, cumulus clouds will develop, and when the clouds reach maturity, the surface winds react to downdrafts initiated by convective rainfall. Figure 15 is an image of the Cape Canaveral area showing the areas from which the satellite data were extracted for comparison with the winds in the PAM (large box) and KSC (small box) mesonets. These areas were designed to approximately coincide with the location of the PAM and KSC networks. Each half-hour image was visually checked and it was found that the networks were adequately covered with a single exception. The lone exception was the 11th of July when the satellite navigation was inaccurate to the extent that this day had to be excluded from the calculations.

Forty day averages of reflectance reveal the existence of the well documented afternoon convective cloudiness in Florida. Figures 16(a) and 16(b) display average reflectance and spatial variance of reflectance over the PAM and KSC networks. The solid lines indicate the area-average reflectance for the networks. Over both networks, the reflectance increases as the day progresses. Initially, this is due to small cumulus developing from surface heating during the morning hours. Over both networks, the peak values of reflectance have been attained by mid-afternoon and the reflectance stays near those peak values, indicating wide spread cloud coverage. This is characteristic of cumulus

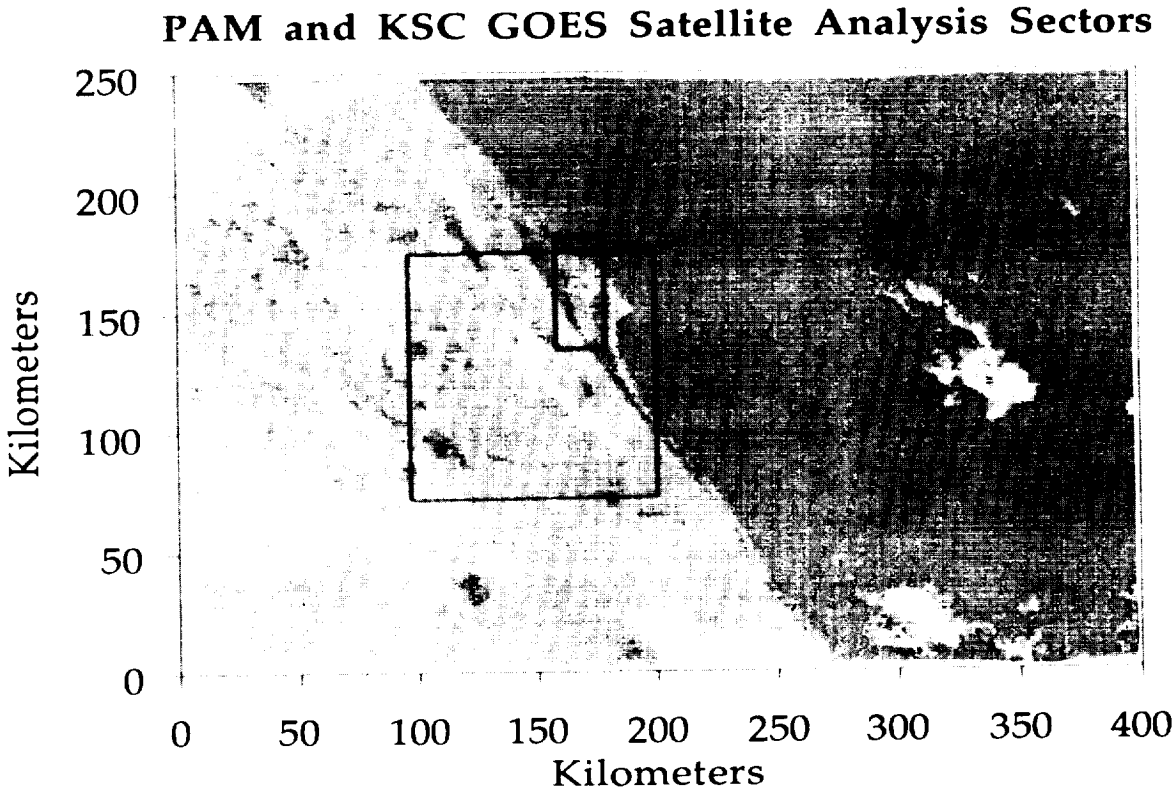

Figure 15: Enhanced visible satellite image of the CaPE study area with boxed regions representing areas over which satellite derived parameters were calculated. The larger box represents the area encompassed by the PAM network and the smaller box represents the area encompassed by the KSC network.

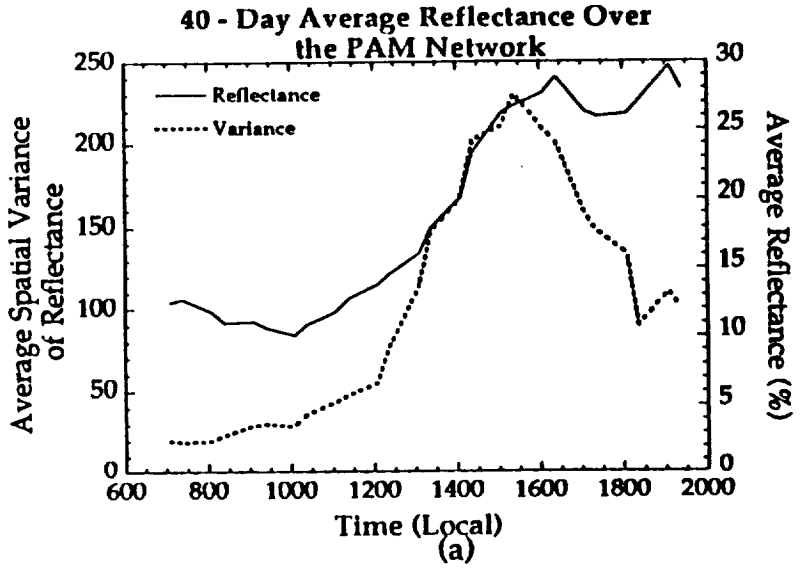

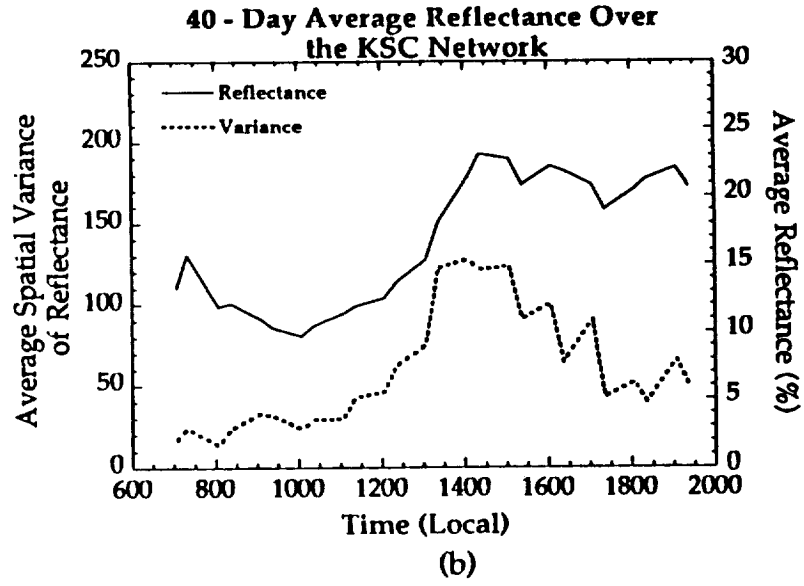

Figures 16(a) and 16(b): 40-day diurnal average of visible reflectance (solid line) and spatial variance of visible reflectance (dashed line) calculated over the PAM network (a) and KSC network (b).

developing into cumulonimbus, dissipating out and leaving the highly reflective anvils behind to maintain the high area-averaged reflectance values. The dashed lines represent the diurnal pattern in spatial variance of reflectance over the networks. As the cumuli are developing, the spatial variance of reflectance over the network area rapidly increases due to the appearance of a large number of individual cloud elements interspersed with patches of ground in the satellite image. This generally occurs between 1000 and 1300 LDT. When the cumulus fully develop into mature, raining cumulonimbus clouds with widespread anvils, the spatial variance decreases due to uniformity of the cloud cover as seen by the satellite. The variance is lower in the KSC network because the area is smaller than the PAM network and therefore more likely to be uniformly covered by clouds that would only partly obscure the PAM network. The lower values of reflectance in the afternoon over the KSC network indicate that cloud coverage is not as widespread over Merritt Island as it is over the mainland during the afternoon. This is because the sea breeze circulation and its associated convection has generally propagated onto the mainland by that time.

Careful examination and comparison of Figures 14(a), 14(b), 16(a), and 16(b) show that over the PAM network, the surface divergence is closely related to a rapid increase in reflectance and spatial variance of reflectance. Active cumulonimbi are associated with a peak reflectance and variance, followed by maintenance of high reflectance values and a rapid drop-off in spatial variance. The peak surface wind divergence in the PAM network occurs a full hour before the peak satellite signal. Over the KSC network, the peak satellite signal and peak surface divergence are coincident, indicating a 'scaling' lag in the larger network between surface winds and satellite imagery. These patterns in the

satellite reflectance also correspond to the mean spatial variance in the surface wind fields, and in turn, to the average rainfall measured in the surface network.

Figures 17(a) and 17(b) show how the average divergence correlates with the average network rainfall and with the spatial variance in divergence over both networks. The average spatial variance of divergence can be regarded as a measure of the mean vertical perturbation kinetic energy over the network and it follows that the maximum rainfall should occur near the time of the maximum variance in divergence over the net. This is clearly observed in Figure 17(a) for the PAM network.

In Figure 17(b), for the KSC network, the peak accumulated rainfall occurs near the time of maximum convergence. As observed in the previous figures, the KSC network, with its higher spatial resolution, generates a noisier signal than does the PAM network. The KSC network also shows maximum rainfall occurring coincident with the peak in the spatial variance of divergence, around 1300 LDT. The rainfall over the KSC network is substantially less than the rainfall over the PAM network because there are more stations recording rainfall in the PAM network, over a greater area.

In order to check consistency of the satellite analysis and the surface wind analysis, the relationships between 40-day averages of spatial variance of reflectance and area-averaged divergence over the PAM and KSC networks were examined. The results are shown in Figures 18(a) and 18(b). The two types of information show a high correlation in the mean, which was not unexpected because, as the spatial variance in the vertical wind speed over the network increases, one can generally conclude that it is a result of downdrafts associated with convective activity. As variance in divergence increases, the variance in reflectance over the satellite scene is also expected to increase. At low levels of

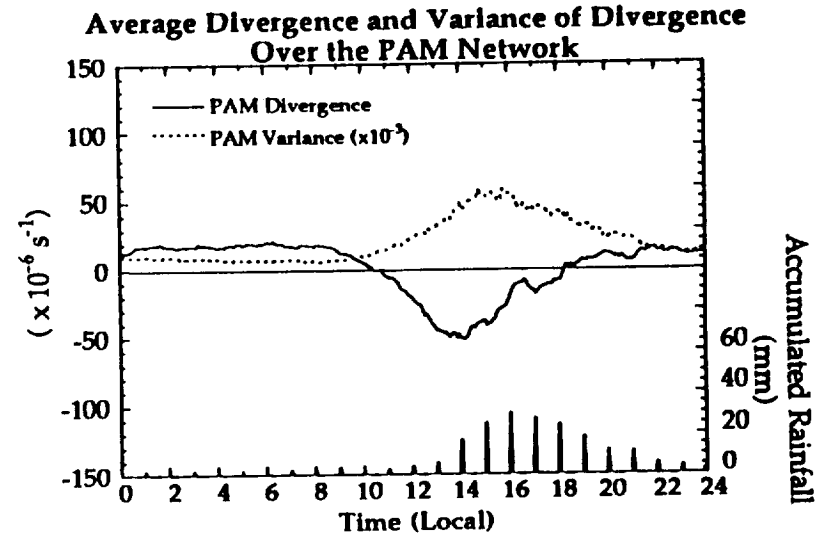

(a)

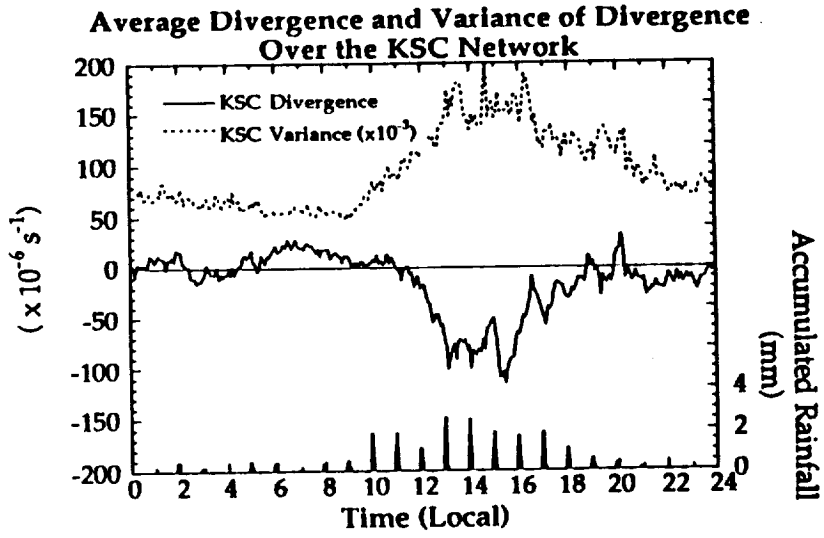

(b)

Figures 17(a) and 17(b): 40-day diurnal average of divergence (solid line), spatial variance of divergence (dashed line) and hourly accumulative rainfall over the PAM network (a) and KSC network (b).

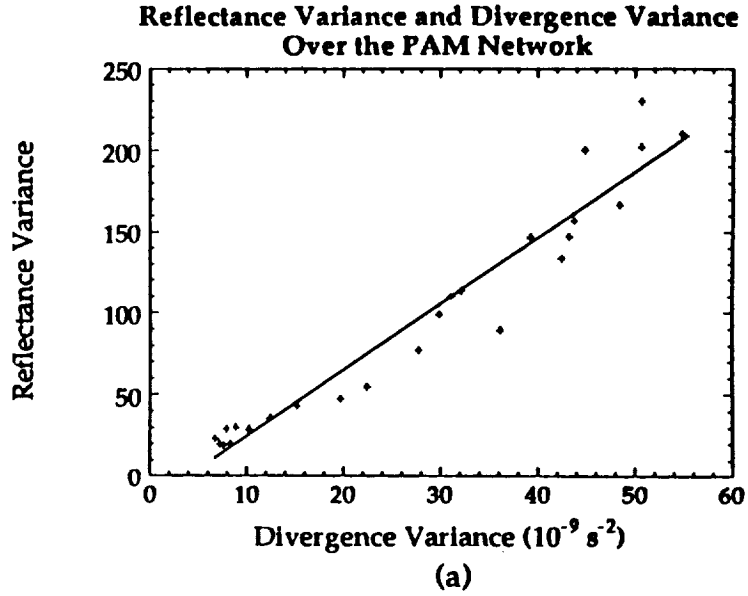

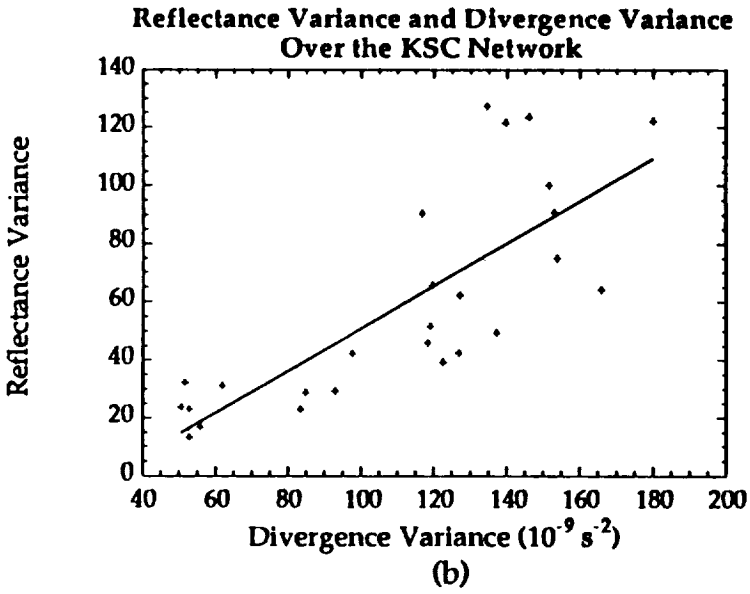

Figures 18(a) and 18(b): Correlation of 40 day averages of spatial variance of reflectance and spatial variances of divergence ($x10^3$) from the PAM network (a) and KSC network (b). Line is a least-squares best fit.

reflectance variance, the satellite image scene is either dominated by anvil cloud, associated with little variance in reflectance or mostly clear. In the case where it is mostly clear, one would expect the surface wind field to be generally unperturbed. When the satellite scene is filled by anvil cloud, the surface below is most likely in the stable, suppressed region in the lee of the active parts of the system. For the 40-day average, the correlation was found to be slightly higher in the PAM network because the PAM network has inherently less noise in the signal. The correlation coefficients between the satellite and the spatial variance in the vertical wind speeds at the surface for the PAM and KSC networks were found to be 0.97 and 0.86, respectively. These exceptionally high correlation coefficients provide evidence of a strong physical relationship between surface convergence of air and the growth of cumulus clouds.

The regression equation for the best fit line for divergence variance ($\overline{w'^2}$), and reflectance variance over the PAM network is:

$$\overline{\sigma_R^2} = 4.05 \cdot \left(\overline{w'^2}\right) - 16.4 \tag{3}$$

and over the KSC network:

$$\overline{\sigma_R^2} = 0.73 \cdot \left(\overline{w'^2}\right) - 22.2 \tag{4}$$

where the units of $\overline{w'^2}$ are s^{-2}. Figures 19(a) and 19(b) show the divergence variance correlated with rainrate (from Figure 17) over the two networks. Regression equations for Figure 19 yield:

$$\overline{w'^2} = 1.65 \cdot \overline{RR} + 7.9 \tag{5}$$

for the PAM network and:

$$\overline{w'^2} = 32.25 \cdot \overline{RR} + 66.0 \tag{6}$$

for the KSC network where the units of rainrate are $mm \bullet hr^{-1}$. Combining equations (3) with (5), and (4) with (6) gives:

$$\overline{\sigma_R^2} = 6.68 \cdot \overline{RR} + 15.5 \tag{7}$$

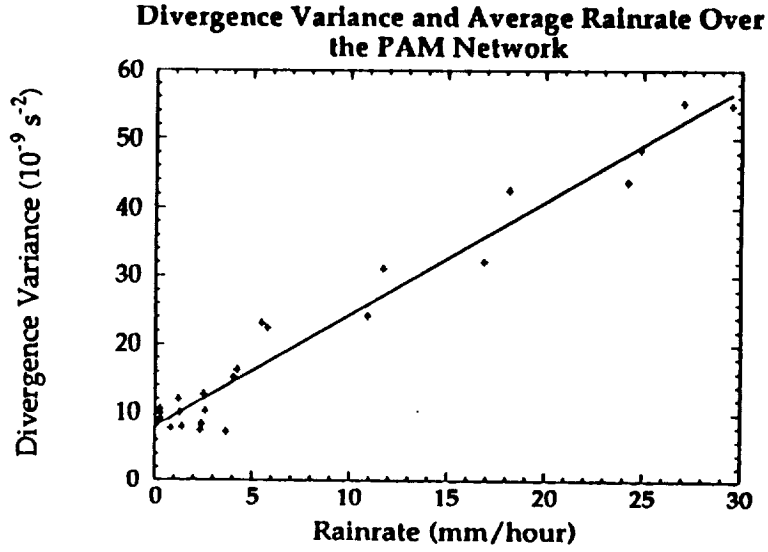

(a)

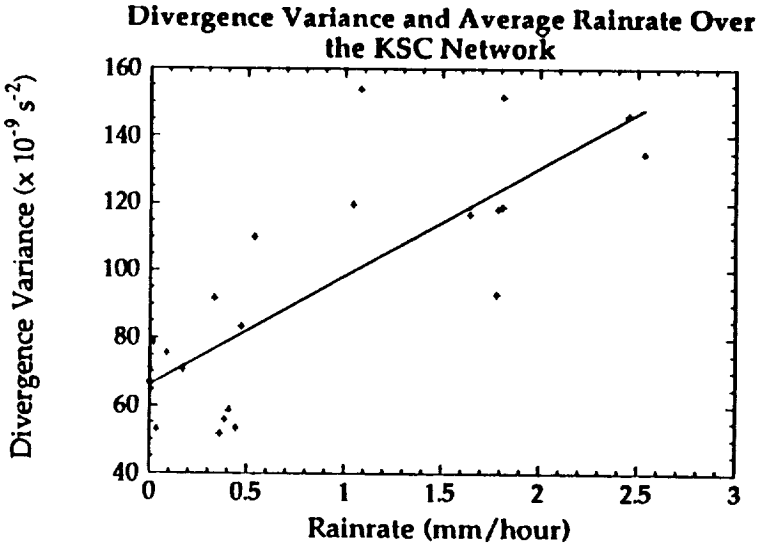

(b)

Figures 19(a) and 19(b): Correlation of 40 day average of spatial variance of divergence (x10^3) and 40 day average of hourly rain rate from the PAM network (a) and KSC network (b). Line is a least-squares best fit.

over the PAM network and:

$$\overline{\sigma_R^2} = 23.54 \cdot \overline{RR} + 26.2 \tag{8}$$

over the KSC network.

Rainrate was not directly correlated with reflectance because the wind perturbations caused by the convection represent a spatially continuous field, unlike areal rainfall which is a spatially discrete field in a convective regime such as south Florida during the summer. In addition, the satellite cloud cover effect on reflectance appears to be related to the wind fields, even when there is no rain measured. Over the PAM network, it was found that the maximum rainrate followed the minimum variance of divergence by about 1 hour while in the KSC network, the maximum rainrate was found to lead the minimum divergence variance by about 2 hours.

3.4 The Flow Classification Scheme

In order to perform detailed analysis of the surface fluxes, it was first necessary to categorize each day in terms of the local circulations immediately effecting the FSU flux sites on the island, and to group those days having similar local flow characteristics. This was done by comparing the spatially averaged vertical wind speeds measured by the independently instrumented PAM and KSC mesonetworks over Merritt Island. The average vertical speed was calculated from the area-averaged divergence. It is assumed that the horizontal divergence varies linearly with height between two levels near to the ground. That is:

$$\nabla_H \cdot \overrightarrow{v(z)} = m \cdot z + c \tag{9}$$

or, with rearrangement of terms:

$$c = \nabla_H \cdot \overrightarrow{v(z)} - m \cdot z \tag{10}$$

where z is vertical height and $\nabla_H \cdot \overrightarrow{v(z)}$ is the divergence of the horizontal wind speed. Taking z_0 to be the lower level and z_1 to be the upper level, the slope, m, is given by:

$$m = \left[\frac{\nabla_H \cdot \overrightarrow{v(z_1)} - \nabla_H \cdot \overrightarrow{v(z_0)}}{z_1 - z_0} \right] \tag{11}$$

Given that

$$\int_{z_0}^{z_1} \nabla_H \cdot \overrightarrow{v(z)}\, dz = - \int_{z_0}^{z_1} \frac{\partial w(z)}{\partial z} dz \tag{12}$$

where w(z) is the vertical wind speed. Substituting equation (9) into the left hand side of (12) yields:

$$\int_{z_0}^{z_1} m \cdot z + c \;\; dz = - \int_{z_0}^{z_1} \frac{\partial w(z)}{\partial z} dz \tag{13}$$

Integration of both sides and rearranging yields:

$$w(z_1) = w(z_0) - \frac{m}{2} \left(z_1^2 - z_0^2 \right) - c \cdot (z_1 - z_0) \tag{14}$$

If we take $z_0 = 0$ for ground level and apply the boundary condition of $w(0) = 0$, then equation (14) reduces to:

$$w(z_1) = - \frac{m}{2} \left(z_1^2 \right) - c \cdot (z_1) \tag{15}$$

Substituting for m from equation (11) into equation (15) yields:

$$w(z_1) = - \frac{\nabla_H \cdot \overrightarrow{v(z_1)}\, z_1^2}{2 \cdot z_1} \tag{16}$$

If z_1 is taken to be the height of the PAM wind towers (z_p), then the vertical velocity at that height can be given by:

$$w(z_p) = - \frac{\nabla_H \cdot \overrightarrow{v(z_p)}\, z_p}{2} \tag{17}$$

If z_2 is taken to be the height of the KSC wind towers (z_k), then the vertical velocity at the upper level can be found from substituting equation (17) into equation (14), yielding:

$$w(z_k) = w(z_p) - \frac{m}{2}\left(z_k^2 - z_p^2\right) - c\cdot\left(z_k - z_p\right) \qquad (18)$$

By examining the vertical velocities at the two levels, a scheme for classification of the flow was developed, and consistency between the measurements in the two networks was checked.

Figures 20(a) and 20(b) show how the vertical speeds over Merritt Island at the two levels compared on two selected days. Visual inspection of the satellite imagery revealed that the 26th of July contained a large storm system which dominated the network and that the 6th of August was cloud free over Merritt Island. As expected, the storm day shows much larger mean vertical speeds than the clear day. In both cases, the larger speeds are associated with the upper height. The clear day is mostly confined to low positive values, indicating that the island maintained low level convergence. Interpretation of figures such as 20(a) and 20(b), for each of the 40 experimental days, leads to a classification scheme. The four quadrants in Figure 20(b) have been labeled I through IV. In both cases in Figure 20, most of the points are contained within quadrants I or III. Quadrant I corresponds to points where both the upper and lower velocities are positive, while quadrant III corresponds to points where both the upper and lower velocities are negative. In comparison, few points on these two days fall into quadrants II or IV. Quadrant IV corresponds to points where the upper velocities are negative and the lower velocities are positive, while quadrant II corresponds to points where the upper velocities are positive and the lower velocities are negative. The quadrants where the velocities at the two heights match signs are defined as "coupled" and the quadrants where the velocities at the two heights differ in sign are defined as "un-coupled". This immediately leads to a 4-way classification scheme for the flow over the island based on the

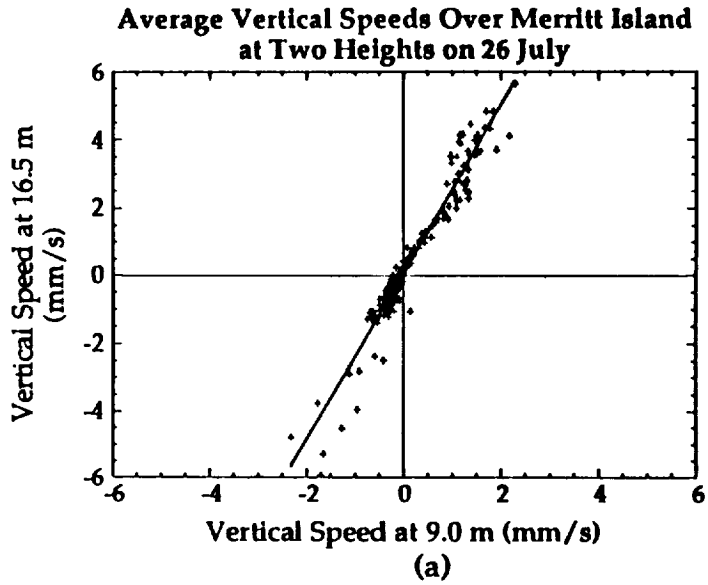

(a)

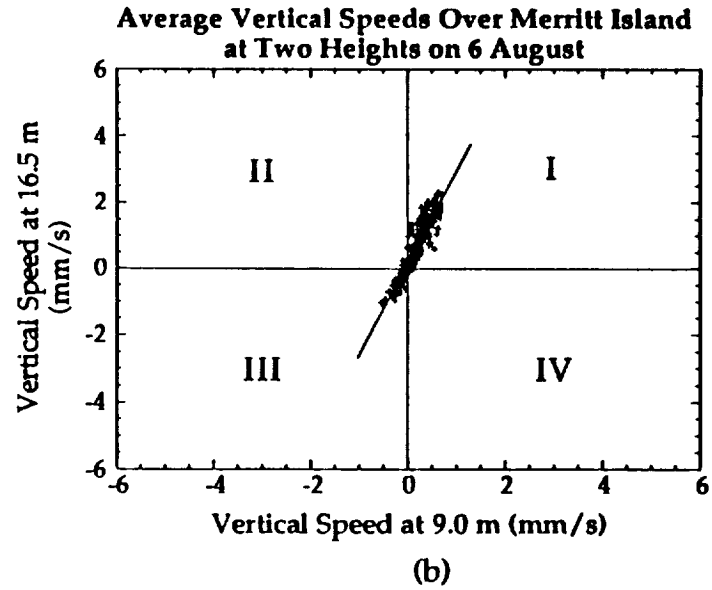

(b)

Figures 20(a) and 20(b): Vertical speeds as determined at the PAM (9.0 m) and KSC (16.5m) levels over Merritt Island for the 26th of July (a) and the 6th of August (b). Line is a least-squares best fit. Quadrants are numbered in (b) in the traditional manner.

two networks being coupled or un-coupled. Figure 21 depicts these 4 possibilities in detail. This classification scheme does not allow small scale vertical circulations with eddies smaller than the resolution between the two networks. It follows that quadrant I is classified as coupled down, quadrant II is un-coupled up, quadrant III is coupled up and, quadrant IV is un-coupled down. Every 5-minute period of the experiment was classed as belonging to one of the four categories. Figures 22 (a-d) show how the flow grouped at the upper height over Merritt Island for all 5 minute area-averaged vertical wind speeds during the 40-day experimental period. In both of the coupled categories, the flow was consistently up or down. In the cases of un-coupled flow, the direction of the flow is much less clear. The negative points in un-coupled upwards and the positive points in un-coupled downward are attributed to circulations that are more complex vertically than the two levels can resolve, or to noise at low vertical wind speeds.

In Figure 22(a), the concentration of points with the highest positive vertical velocity occurs around 1500 LDT. This is consistent with the accepted idea that the island system should be converging in the afternoon hours. An additional cause of these high values are the afternoon thunderstorm outflows initiating subsequent low level convergence and the possibility of further convective activity. In Figure 22(b), the concentration of lowest mean negative vertical velocities also occurs around 1500 LDT. These can be attributed solely to thunderstorm downdrafts resulting from afternoon sea breeze initiated convective events. Even the appearance of an early storm shows up in the coupled upward and coupled downward fields at around 0800 LDT.

Inspection of Figures 22(a-d) leads to the conclusion that the coupled modes were the significant configuration over the island. In order to classify

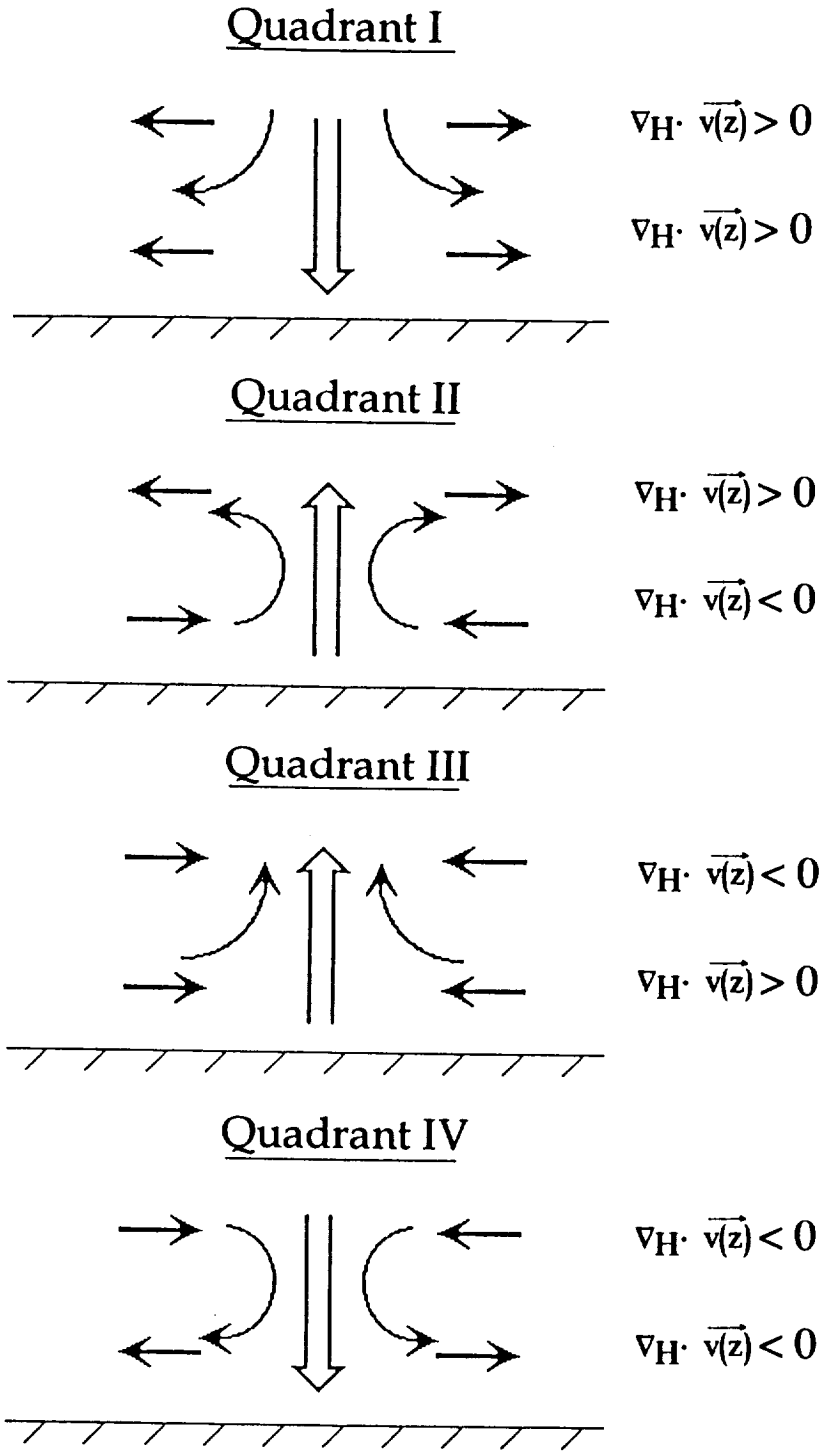

Figure 21: Probabilistic flow diagrams based on horizontal divergence for each of the four quadrants in Figures 20a and 20b. Quadrant I implies coupled downward, quadrant II implies uncoupled upward, quadrant III implies coupled upward, and quadrant IV implies uncoupled downward.

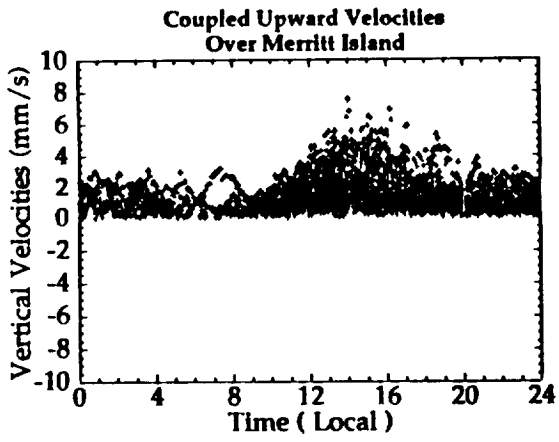

(a)

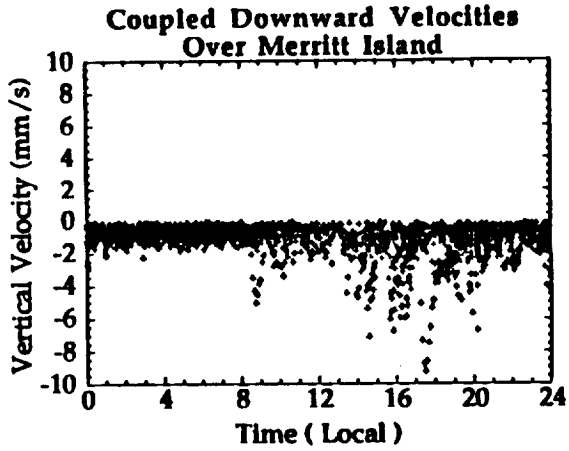

(c)

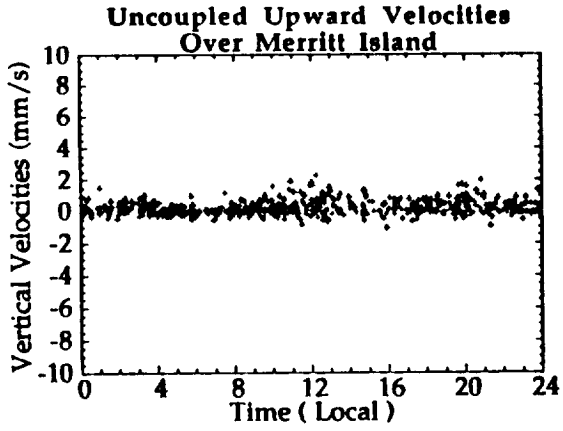

(b)

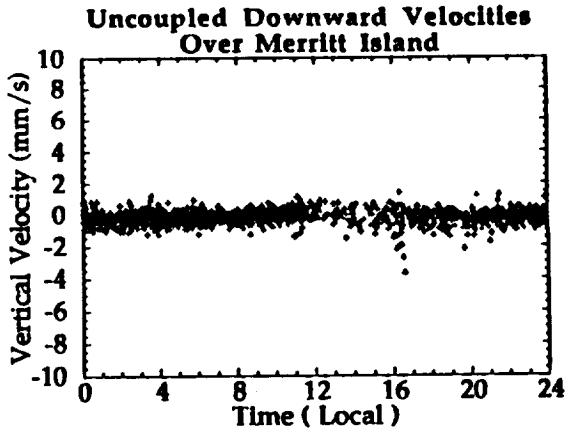

(d)

Figures 22(a) - 22(d): Vertical velocities over Merritt Island when the flow is coupled upward, i.e. when flow characteristics fall in quadrant III (a), uncoupled upward, i.e. quadrant II (b), coupled downward, i.e. quadrant I (c), uncoupled downward, i.e. quadrant IV (d).

each day separately, each 5-minute period of each day was classified into one of the 4 modes, and each day was further analyzed as to the amount of time during that day was spent in each mode. The uncoupled modes played a minor role in terms of the percentages of each day that were spent in those modes. In fact, un-coupled up never accounted for more than 15 percent of any given day, while un-coupled down occurred a significant percentage of the time only during the first few days of the experiment. As previously discussed, this period was disturbed due to early morning storms. Again around August 1st, un-coupled down was relatively important, occurring about 40 percent of the time each day. However, vertical speeds associated with un-coupled flow are inevitably close to noise levels as seen in Figures 22(b) and 22(d), and therefore only the coupled modes were given detailed consideration.

Figure 23 shows the coupled modes over the course of the experiment. There are two periods that stand out clearly, one centered around the 20th of July and another centered around the 7th of August. These are periods when the island is spending most of the day in the coupled upward mode. Both of these periods correspond to periods of southerly and southeasterly flow as shown by the CCAFS soundings in Figures 10-12. In contrast, the period surrounding the 26th of July shows that the island spent roughly the same amount of time in the coupled upward mode as it did the coupled downward mode, indicating a greater likelihood that a classical diurnal sea breeze circulation was present. This period of time corresponds to mostly southwesterly flow as determined from the sounding analyses. Other periods during the experiment can also be resolved, including the disturbed period at the beginning of the experiment and the period near the end when the networks were under the influence of hurricane Bob. Byers and Rodebush (1948) show that the expected behavior of the "classical"

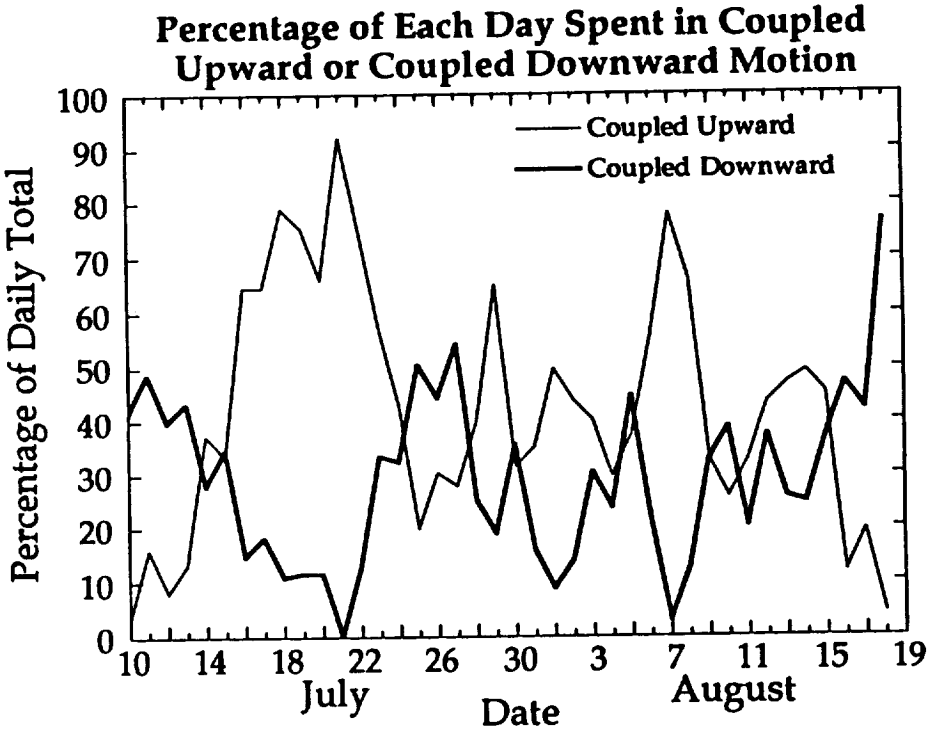

Figure 23: Percent of each day spent in coupled motions for the duration of the experiment; coupled upward (thin solid line) and coupled downward (heavy solid line).

summertime sea breeze regime over the entire Florida penninsula is one in which roughly 40% of the day is spent in coupled upward motions (low level convergence) due to heating of the surface, whereas 60% of the day is spent in coupled downward motion (low level divergence) due to the subsequent nighttime land breeze circulation. The percentage of time spent in each regime is expected to differ over the Merritt Island regime due to the interaction between the sea breeze and river breezes from the Banana and Indian Rivers (Zhong et al., 1991). Merritt Island shows a pattern in the 40 day mean divergence fields where 61% of the time is spent in the upward motion regime and 39% is spent in the downward motion regime.

Using the results from the coupled mode calculations over Merritt Island, each day of the experiment was initially classed into one of three categories. The categories were delineated by periods of time when:

1) The diurnal sea breeze oscillation is persistently modified in favor of coupled downward motion (defined as Disturbed)
2) The diurnal sea breeze oscillation is persistently modified in favor of coupled upward motion (defined as Type 1) and when:
3) The classical diurnal sea breeze oscillation prevails, that is, the island persistently spends roughly half of the day in coupled upward motion and half of the day in coupled downward motion (defined as Type 2).

Using this partitioning as a basis, five periods were identified in Figure 23. They are:

1) A period before July 13 which exhibited early morning rainfall produced by large-scale disturbances (Disturbed).
2) The period centered around July 20 (Type 1)

3) The period July 25 to August 4 (Type 2)

4) The period August 6 to August 8 (Type 1)

5) The period August 9 to August 15 (Type 2)

6) A disturbed period after August 15 (Disturbed due to hurricane Bob)

For the final step in the classification process, the morning winds from 0900 to 1200 LDT from those PAM stations which were located on the mainland were averaged to determine the morning means of wind direction and speed. From the upper air analysis, which represents the large synoptic scale flow, and the morning wind analyses of the mainland PAM stations, it became clear that Type 1 flow is generally associated with flow which has an easterly component and Type 2 flow is generally associated with flow which has a westerly component. The final classification of each day, however, was based on how much of the day was spent in each of or a combination of the coupled vertical wind speed modes as seen in Figure 23. This reflects the nature of the flow over the island which is in turn influenced by the larger scale flows. By inspection of daily satellite reflectance and variance patterns, and the area-averaged divergence over the island for each Type 1 and Type 2 day, the Type 1 and Type 2 days were further classified as active (A) or inactive (I). Active days were days where consecutive periods of convergence followed by strong divergence was observed in the wind network together with a sharp increase in average reflectance and spatial variance in reflectance. Table 6 summarizes the final classification for each day of CaPE and lists the morning averages of wind speeds and directions. The disturbed days at the beginning of the experiment and the disturbed "hurricane" days at the end are treated as special cases when the sea breeze circulation is not the dominant process.

Table 6: Final classification of CaPE days.

Date	Julian Day	Wind Speed	Wind Dir.	Day Type
10 July	191	3.19 m/s	222	Disturbed
11 July	192	3.13	260	Disturbed
12 July	193	2.54	264	Disturbed
13 July	194	2.08	253	Disturbed
14 July	195	2.99	177	2A
15 July	196	2.71	174	Transistion
16 July	197	3.40	176	1A
17 July	198	2.59	157	1A
18 July	199	1.49	165	1I
19 July	200	1.31	121	1I
20 July	201	0.79	67	1I
21 July	202	1.49	68	1I
22 July	203	1.05	7	1I
23 July	204	0.22	230	1A
24 July	205	0.96	260	1A
25 July	206	1.71	213	2A
26 July	207	1.39	228	2A
27 July	208	1.26	283	2A
28 July	209	2.09	181	2I
29 July	210	3.10	190	2I
30 July	211	3.54	188	2A
31 July	212	4.27	171	2A
1 August	213	4.50	197	2A
2 August	214	3.20	193	2A
3 August	215	0.90	235	2I
4 August	216	1.63	293	2I
5 August	217	1.08	296	Transistion
6 August	218	2.49	146	1I
7 August	219	2.84	119	1I
8 August	220	0.86	180	1I
9 August	221	2.01	256	2A
10 August	222	2.38	253	2A
11 August	223	1054	274	2I
12 August	224	1.81	229	2I
13 August	225	2.18	210	2I
14 August	226	2.90	194	2I
15 August	227	1.03	262	2A
16 August	228	2.33	360	Hurricane
17 August	229	3.69	343	Hurricane
18 August	230	3.17	296	Hurricane

3.5 Sea Breeze Propagation

Once the days had been classified, the next step determined the differences in the nature of the sea breeze convergence zones operating under the different local circulations. This was accomplished by calculating the average divergence from the PAM mesonetwork over Merritt Island and the adjacent mainland for the cases of Type 1 and Type 2 flow. Figures 24(a) and 24(b) show how the two flow regimes differ in terms of the behavior of the resultant area-averaged divergence fields. During periods of Type 1 flow, Merritt Island is constantly convergent whereas the mainland portion is divergent during the early morning hours and then convergent the remaining times. In Type 2 flow, Merritt Island and the mainland display the classical sea breeze pattern of convergence during the day and divergence during the night. This correlates well with the sounding and rainfall analyses which showed that the days of Type 1 flow tended to be more suppressed in terms of convective activity, while the Type 2 flow days were the ones which displayed the most active convective characteristics. In both types of flow, it is clear from Figures 24(a) and 24(b) that in the mean, Merritt Island is reaching peak convergence approximately 2 hours before the mainland. Figures 24(c) through 24(e) show sample views of the divergence data field as calculated from the PAM network. Figure 24(c) shows the divergence field at 1145 LDT for July 21, a typical Type 1 day. As expected, the majority of the PAM network is convergent under this easterly regime. Figure 24(d) shows the divergence field at 1300 LDT for July 29, a typical Type 2 day. The sea breeze convergence front associated with this flow is clearly visible over the southern part of Merritt Island and extending westward to the St. Johns River. Most stations to the west of the sea breeze front show a general westerly component to the flow while stations along the shore clearly show evidence of

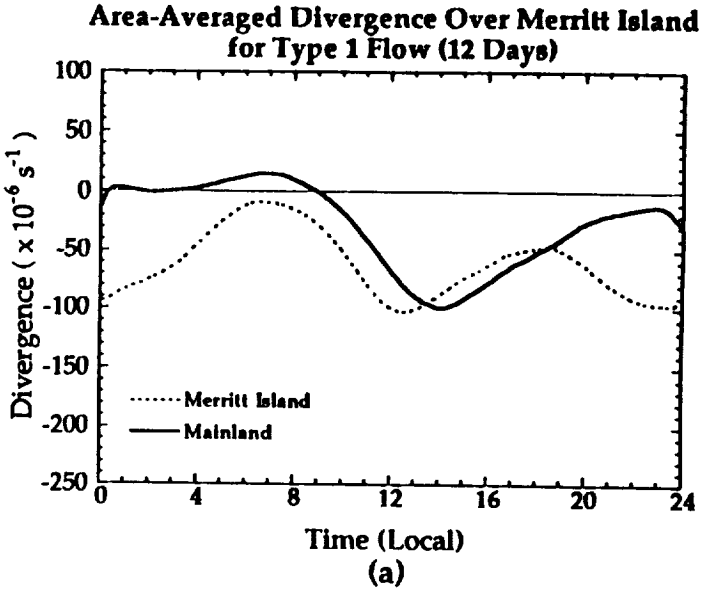

Figures 24(a) and 24(b): Area-averaged divergence over Merritt Island (dashed line) and the Mainland (solid line) diurnally averaged for all Type 1 flow days (12 days) (a) and Type 2 flow days (19 days) (b). Data taken from the PAM network.

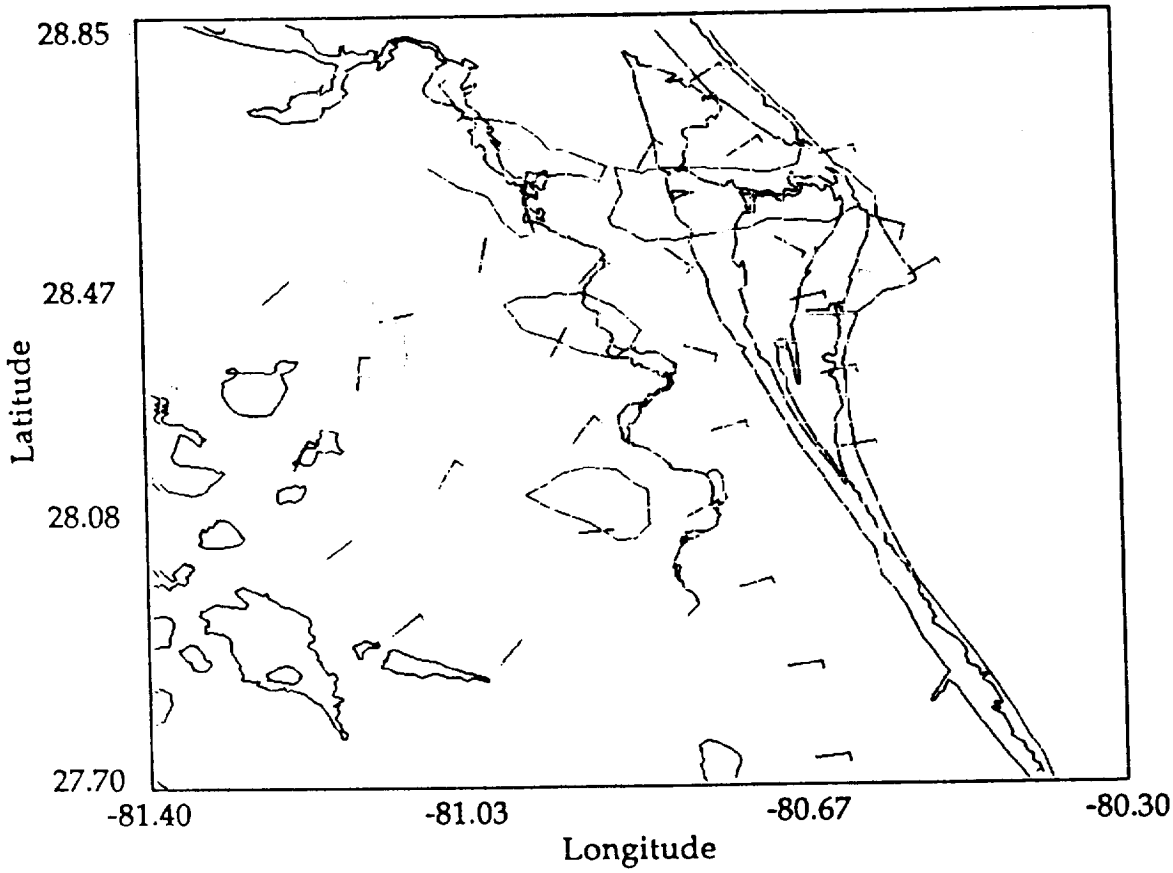

Figure 24c: Area-averaged divergence from the PAM network at 1145 LDT on July 21. A Type 1-I day.

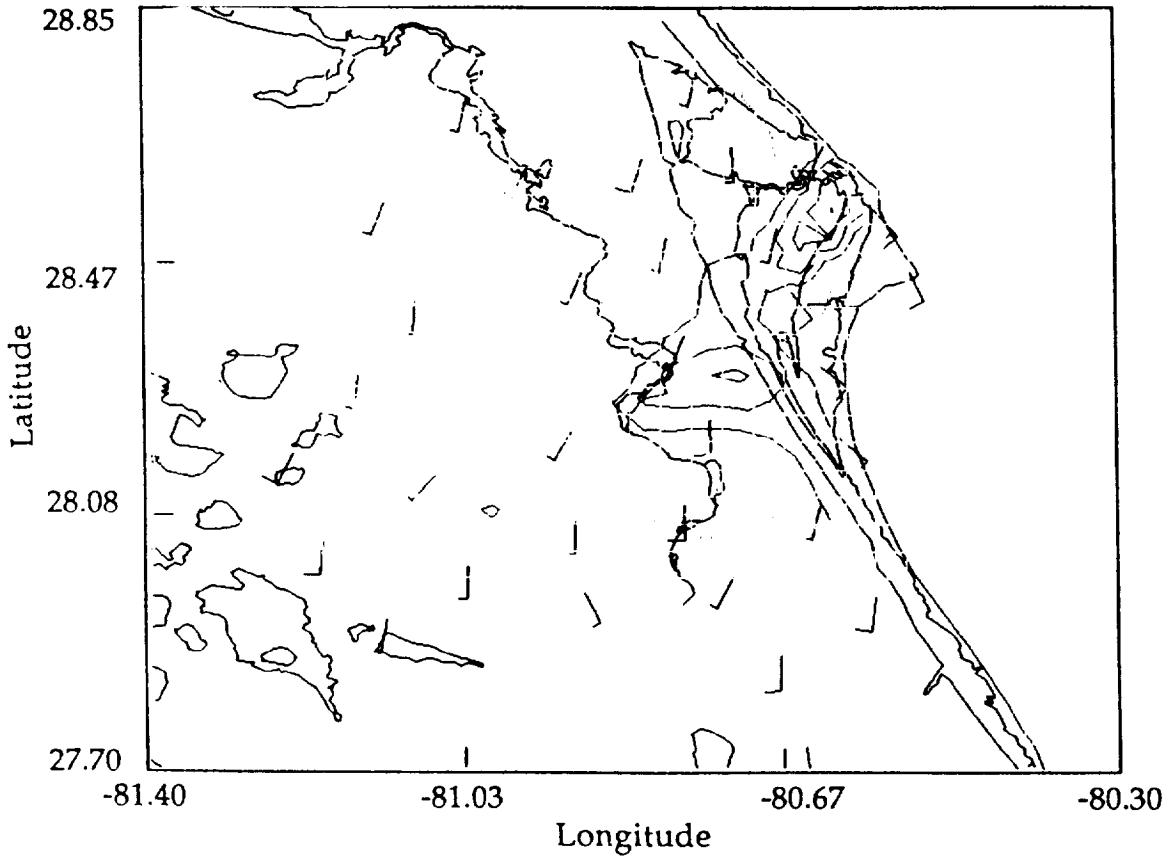

Figure 24d: Area-averaged divergence from the PAM network at 1300 LDT on July 29. A Type 2-I day.

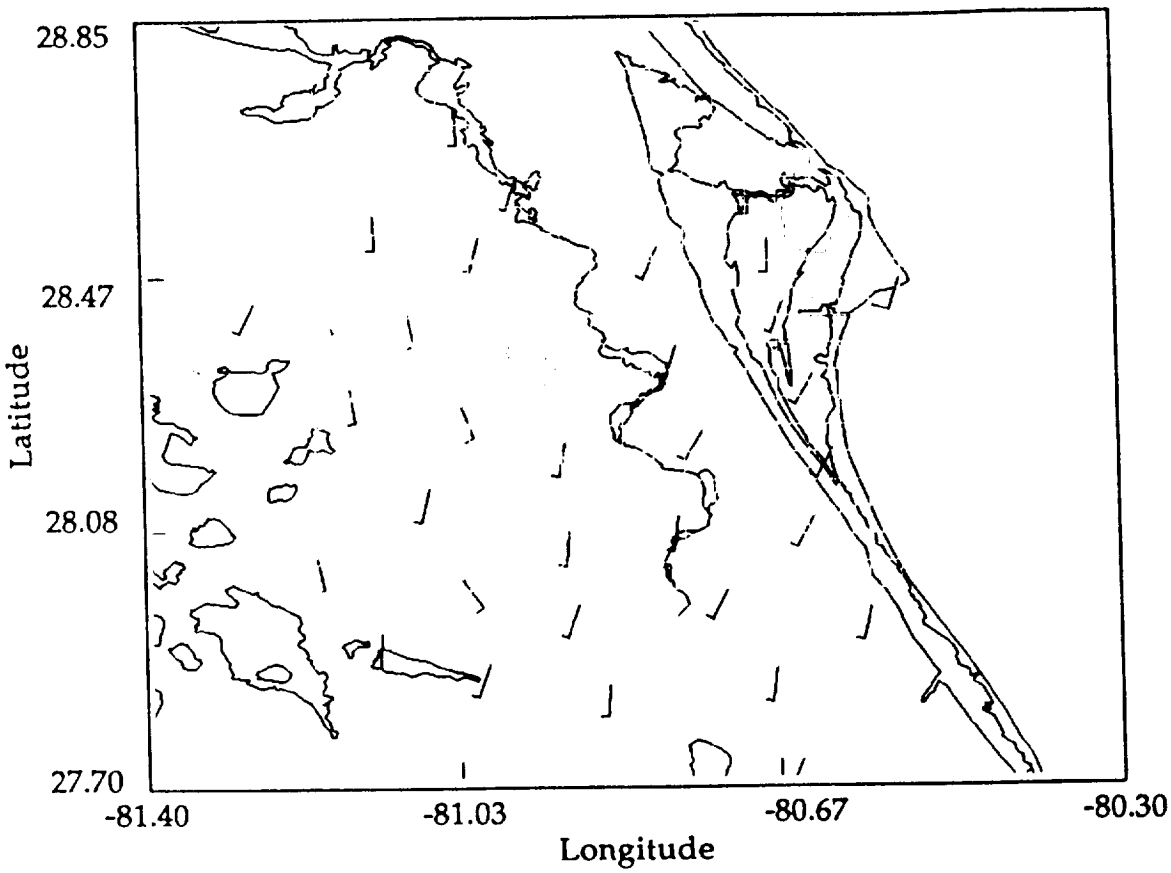

Figure 24e: Area-averaged divergence from the PAM network at 0925 LDT on August 14. A Type 2-I day.

the easterly arm of the sea breeze circulation. Figure 24(e) shows a typical nighttime divergence pattern associated with Type 2 flow. The stations on the eastward side of the mesonet show a definite westerly component as a result of the land breeze circulation.

In order to examine the propagation of the sea breeze convergence zone, north-south space-time cross sections of divergence were calculated from the PAM mesonetwork over the CaPE study area. Figures 25(a-d) show these cross sections for Type 2-A, 2-I, 1-A, and 1-I, respectively. Examination of these cross sections for Type 2-A flow show that the Merritt Island area (80.5 to 80.7 longitude) is strongly divergent during the nighttime and strongly convergent during the day. The Type 2-I flow days show a similar pattern except that the island is consistently convergent later in the day. Both of these results reflect the fact that the Type 2 flow cases are dominated by the classical sea breeze circulations. Figure 25(c), Type 1-A, shows that while the island was convergent during the day, the nighttime hours were also dominated by convergent flow. Figure 25(d) shows clearly that on days of Type 1-I flow, the island system stays in a convergent mode both night and day.

Figure 26 shows the space-time cross section for the 3rd of August. It is a typical example of a Type 2-I flow day when no active convection developed. The inland propagation of the sea breeze front can be seen as the area of convergence moving east to west from 1100 to 2000 LDT. The propagation speed was calculated by finding the slope of the line representing the maximum convergence. This was done for every day when the signal could be readily resolved. The signal does not show up as clear in the average signal because there are differences in the time of day that the sea breeze develops and propagates inland. A feature that was evident on most of the days with Type 2

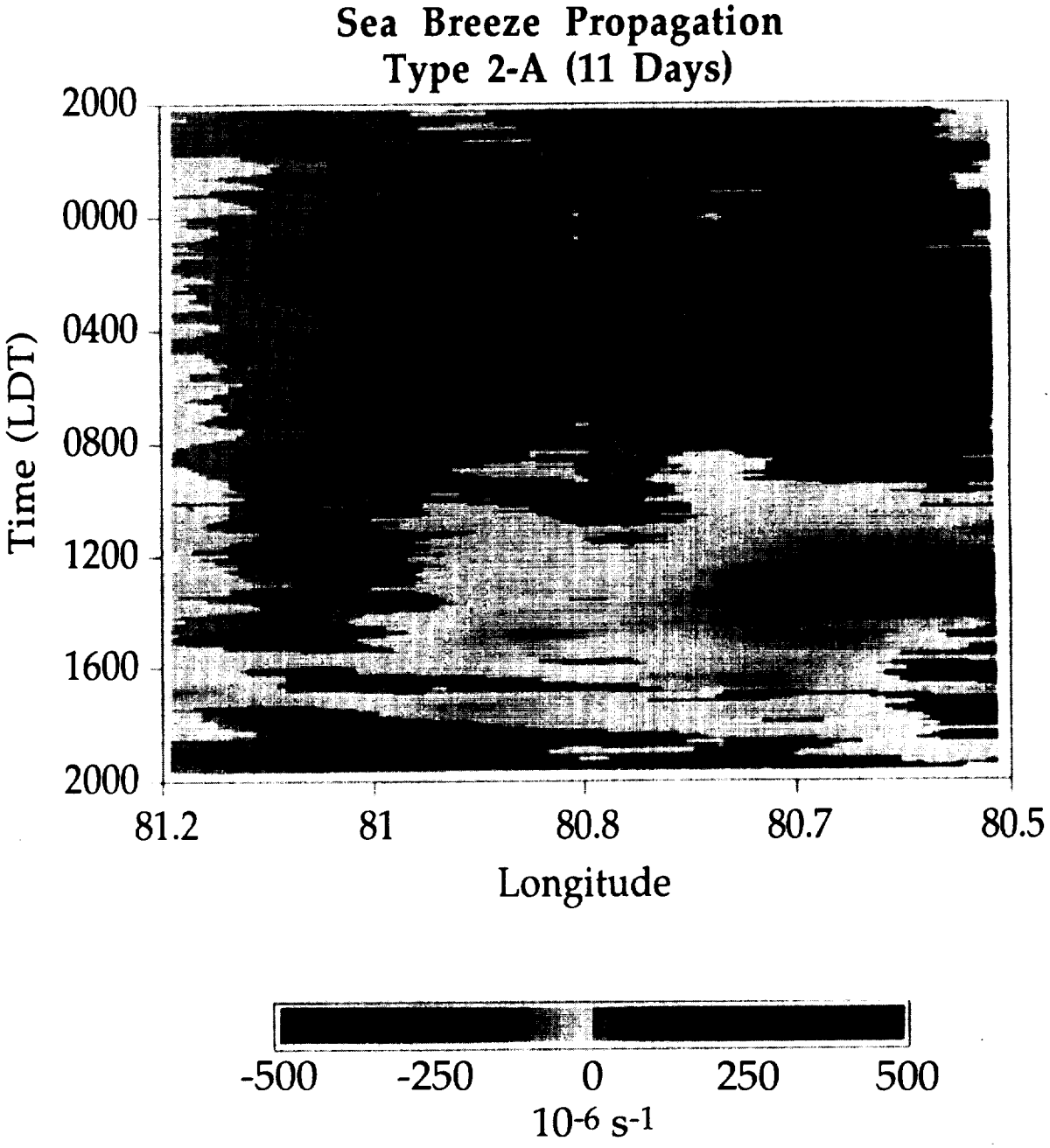

Figure 25a: Time-horizontal space cross sections of divergence over the CaPE study area diurnally averaged over all Type 2-A flow days (11 days). Red and yellow areas indicate negative divergence and blue and black areas represent positive divergence.

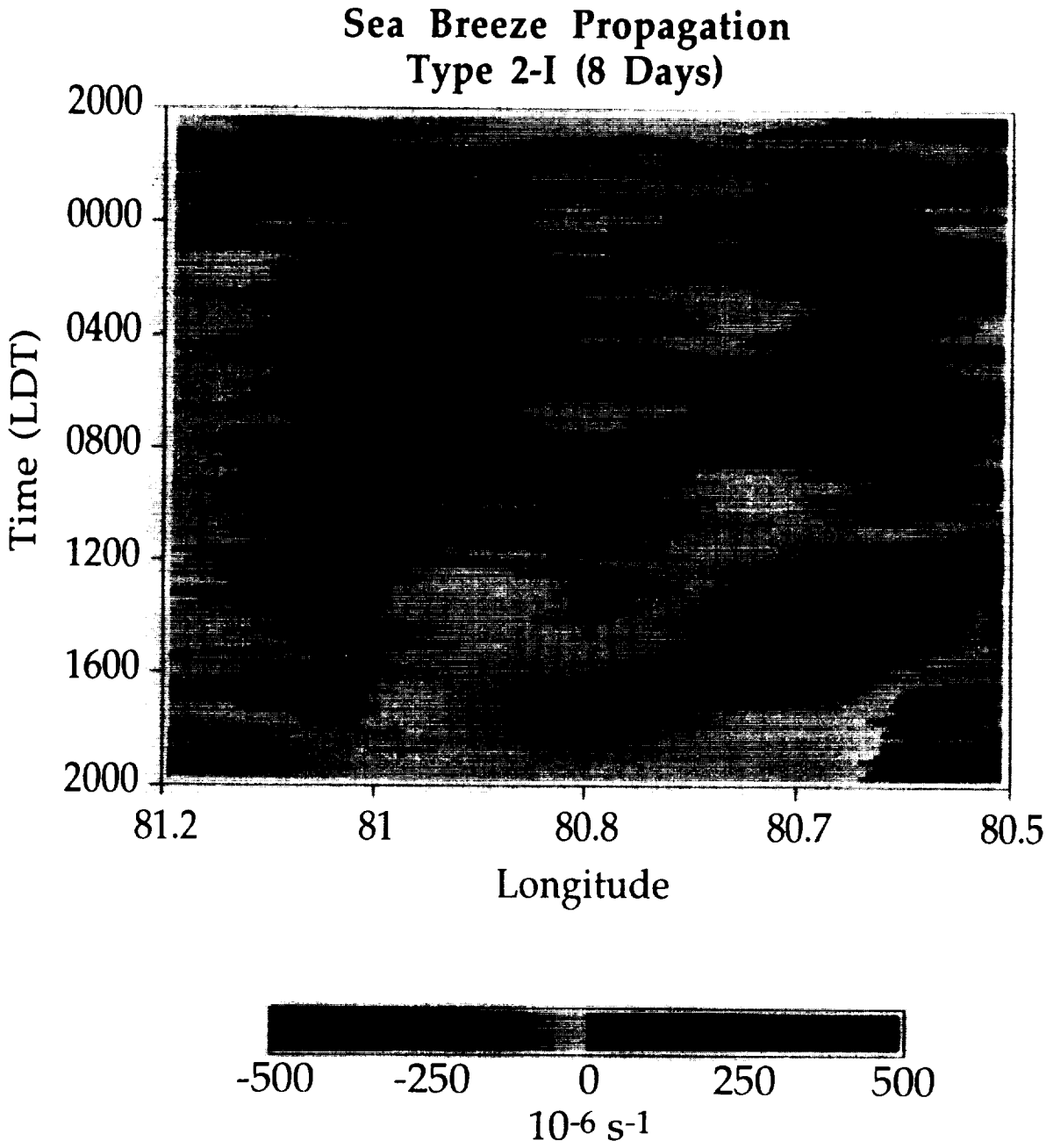

Figure 25b: Time-horizontal space cross sections of divergence over the CaPE study area diurnally averaged over all Type 2-I flow days (8 days). Red and yellow areas indicate negative divergence and blue and black areas represent positive divergence.

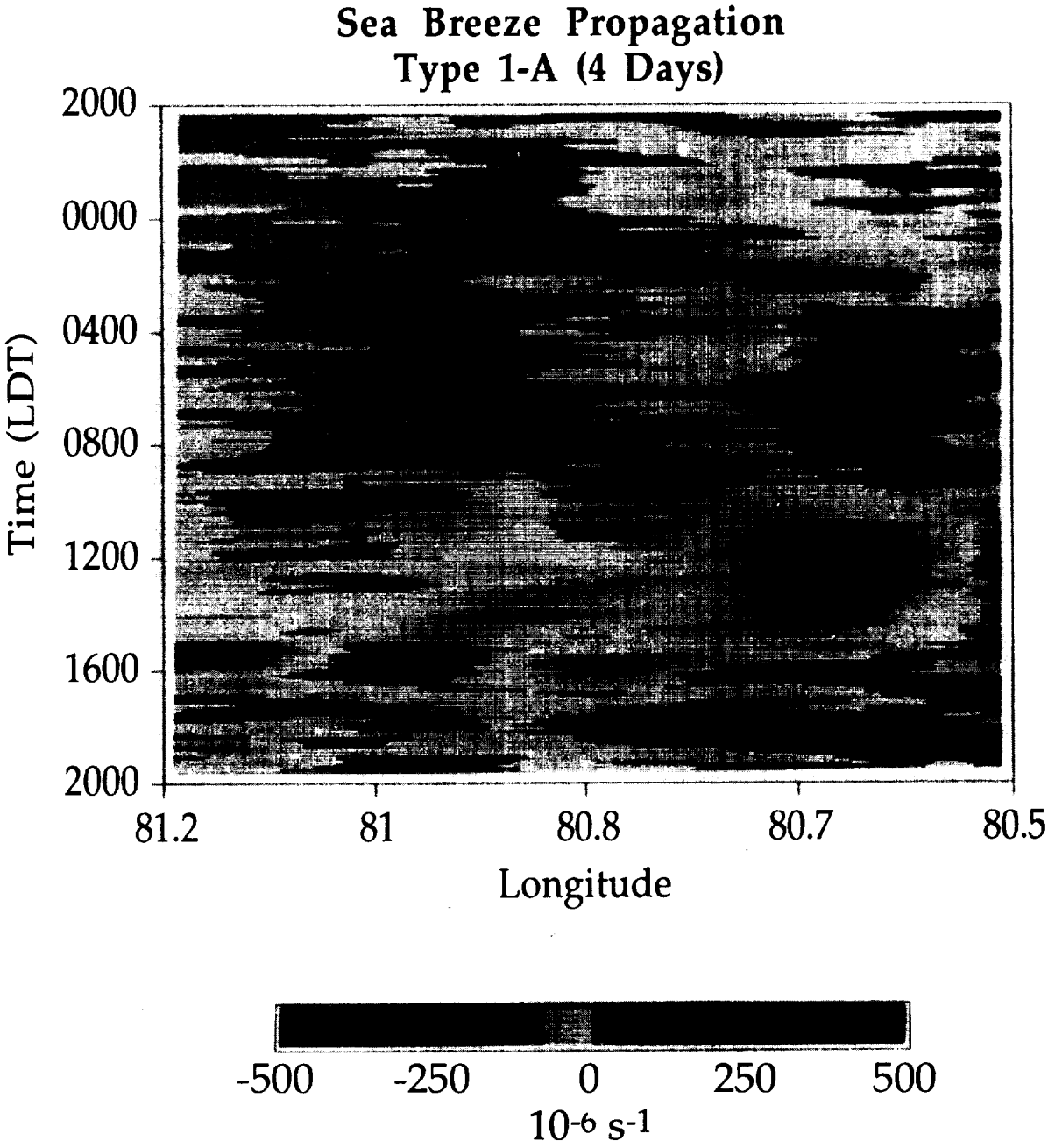

Figure 25c: Time-horizontal space cross sections of divergence over the CaPE study area diurnally averaged over all Type 1-A flow days (4 days). Red and yellow areas indicate negative divergence and blue and black areas represent positive divergence.

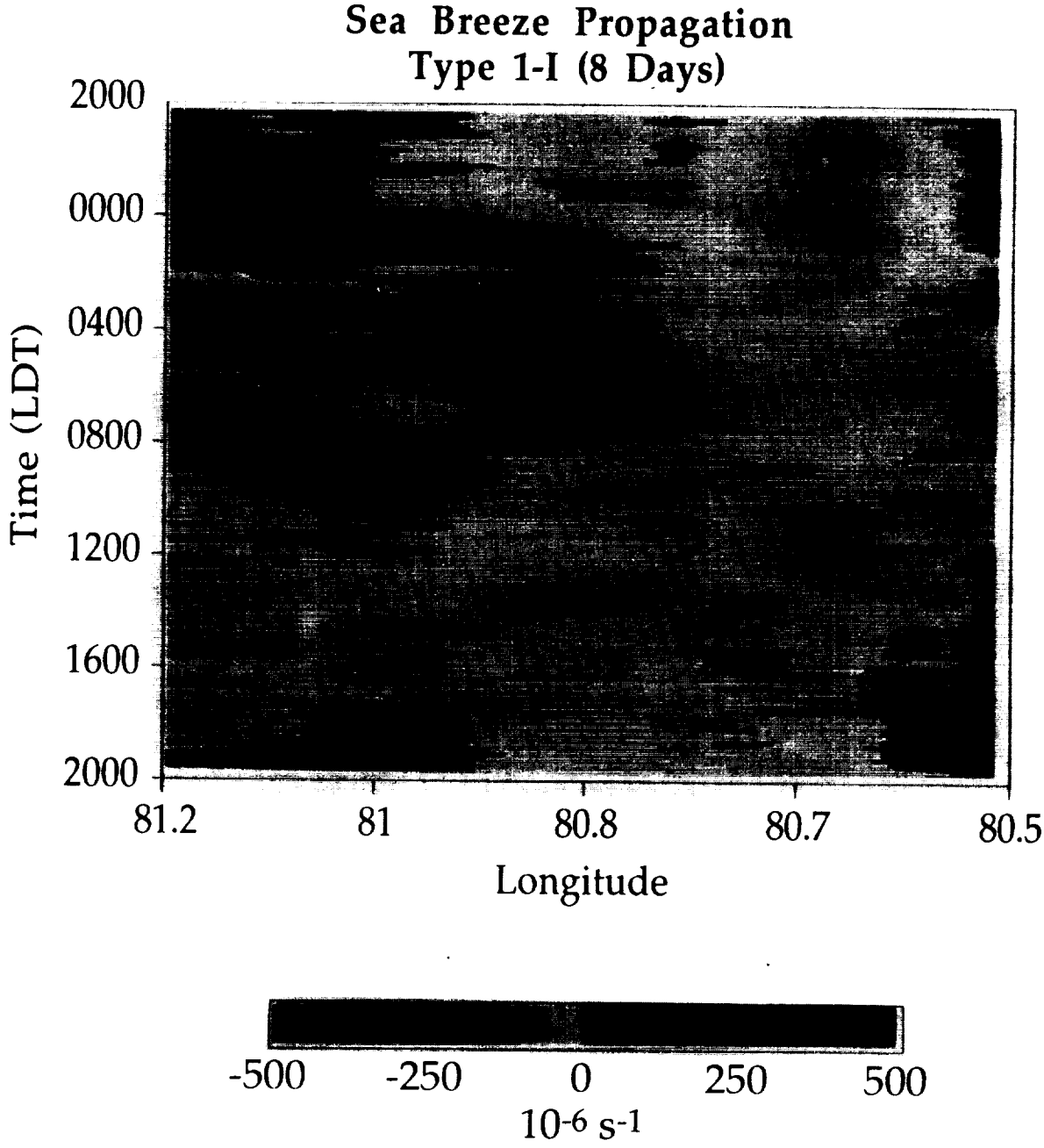

Figure 25d: Time-horizontal space cross sections of divergence over the CaPE study area diurnally averaged over all Type 1-I flow days (8 days). Red and yellow areas indicate negative divergence and blue and black areas represent positive divergence.

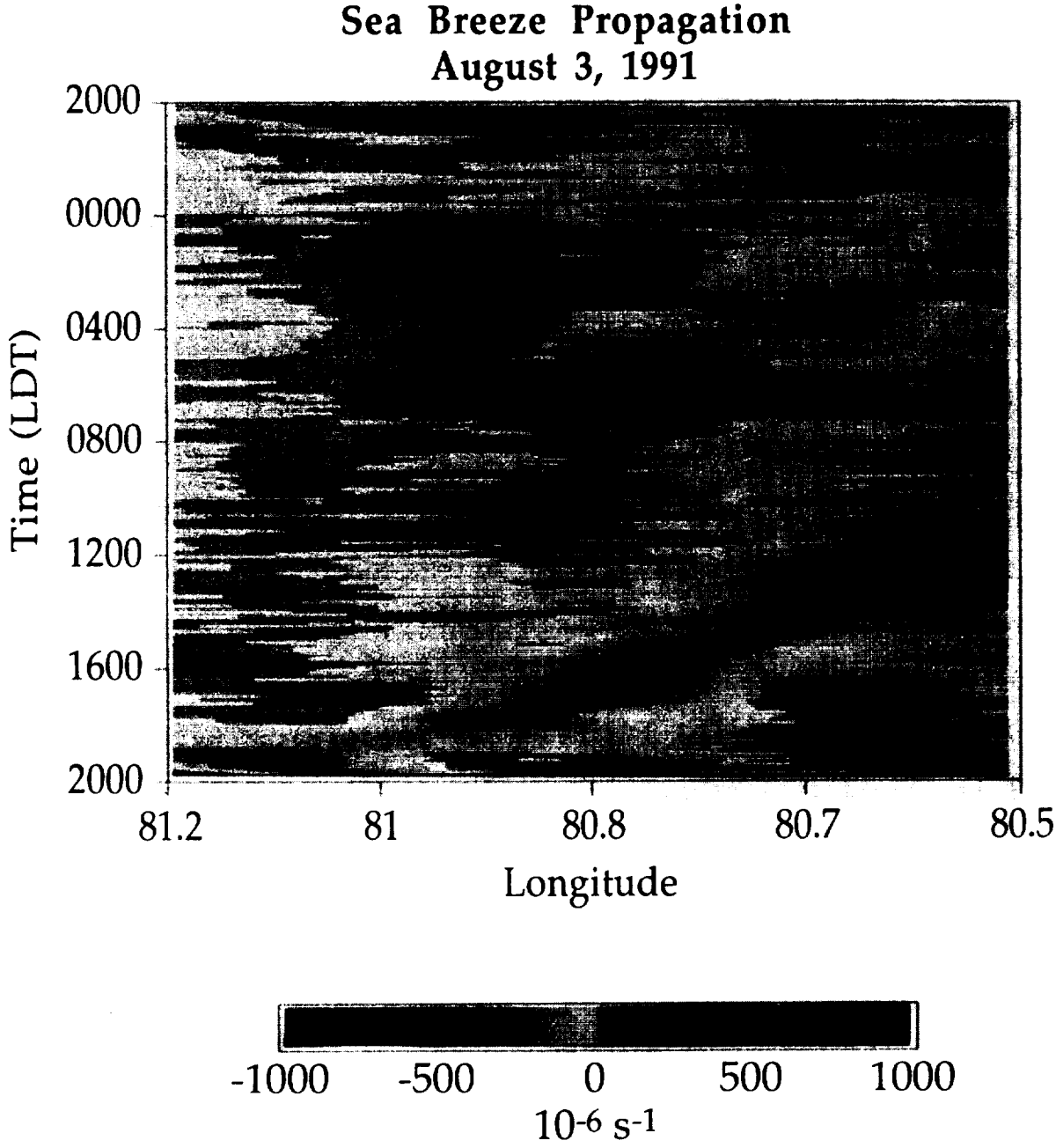

Figure 26: Time-horizontal space cross sections of divergence over the CaPE study area for August 3, 1991. Red and yellow areas indicate negative divergence and blue and black areas represent positive divergence.

flow was a belt of divergence resulting from the outflows of storms as they propagated back eastward across the network. This shows well in Figure 25(a) as the area of divergence at the very bottom of the figure centered around 81.0° west. Analysis of the return propagation speed indicates that the return areas of divergence may travel as much as 3 times faster than the sea breeze front when it moves inland from the east coast earlier in the day. This rapid return speed appears to be influenced by the prevailing large scale flow, and is most likely a result of the west coast sea breeze front merging with the east coast sea breeze and propagating eastward across the peninsula. Simpson et. al. (1980) found that 90% of rainfall in south Florida comes from merged systems such as these observed in the combined sea breezes. Simpson et. al. (1993) also found similar cases in northern Australia. The merging of the two sea breeze fronts is therefore an important rain-producing mechanism. Table 7 shows the calculated velocities for the westward propagation of the sea breeze front and the return propagation of the merged west coast and east coast sea breeze for all cases where there was a discernible signal for Type 1 flow and for Type 2 flow.

Table 7: Sea breeze convergence zone propagation westward and return speed.

Flow Regime	Sea Breeze Front (m/s)	Number of Signals for SBF	Return Front (m/s)	Number of Signals for RF
All Modes	2.91	18	11.28	13
Type 1	2.89	5	14.3	2
Type 2	2.69	11	9.04	9

4.0 Surface Flux Analysis

The nature of the surface fluxes is examined in terms of clear sky fluxes for Type 1 and Type 2 flows. It is found that the primary factor which determines day to day variations in all components of the surface energy budget is the degree of cloudiness and the timing and occurrence or non-occurrence of storms and rainfall. A composite convective event is constructed to describe the fluxes directly beneath a storm downdraft, and to define and quantify a latent heat energy recovery period.

4.1 The Surface Fluxes in Different Flow Regimes

In this section, the surface fluxes of sensible and latent heat are examined by grouping and diurnally averaging fluxes from each station on those days that were under the influence of similar flow conditions. The 6th of August, a Type 1 flow day, was the only day during CaPE that both sites remained cloud free during the day, and inspection of the fluxes at both sites for this day revealed that there was little or no difference at the two sites in terms of magnitude of net radiation under clear sky conditions. Visible satellite imagery for the 6th of August reveals a small thin cirrus area in the early morning hours which dissipates by 0900 LDT. At no point did this cloud obscure the island. During Type 2 flow regimes, the 28th of July was clear only at station 2, the south site. In order to examine how the different flow regimes may cause different partitioning of the available energy into its constituent parts, the averaged fluxes at each site for each regime were compared to clear day values for that particular regime. The magnitude of clear sky net radiation was similar at both sites, however, the

soil heat fluxes were consistently different at the two sites. The soil heat flux at the northern site (1) was consistently 50 $W \bullet m^{-2}$ greater than the soil heat flux at the southern site (2). An examination of the physical characteristics and mineralogical properties of the soils at each site indicate that the soil heat flux should be greater at the northern site. The soil at the southern site was composed primarily of sand while the soil at the northern site had a higher organic content. The measurements of soil moisture content taken during the experiment indicate that the soil at the northern site consistently contained more moisture than the soil at the southern site. This was verified by collected samples of soil and by gypsum blocks deployed at each station. This additional moisture raises the volumetric soil heat capacity which raises the soil heat flux at the northern site and therefore led to differences in the magnitudes of the soil heat fluxes at the two stations, hence, a station-dependent analysis was performed. This resulted in eight cases for clear day comparison: (1) station 1 Type 1-I; (2) station 1 Type 1-A; (3) station 1 Type 2-I; (4) station 1 Type 2-A; (5) station 2 Type 1-I; (6) station 2 Type 1-A; (7) station 2 Type 2-I; and (8) station 2 Type 2-A. Because no clear day occurred under Type 1 flow at station 2 during CaPE, clear day analysis for station 2 Type 1-I and station 2 Type 1-A could not be performed.

4.1.1 Inactive and Clear Day Comparison

Figures 27(a-f) show the comparison between clear days and inactive days for Type 1 and Type 2 flow. Figures 27(a) and 27(b) show the partial surface energy budget for station 1 and station 2 Type 1-I cases, in which the net radiation shows a decrease from clear day values well before clear day peak values are obtained. This is indicative of late morning or early afternoon cloudiness. This is most clearly seen at station 2, the inland site. The net radiation values for Type 1-I can be as much as -150 $W \bullet m^{-2}$ below that of the

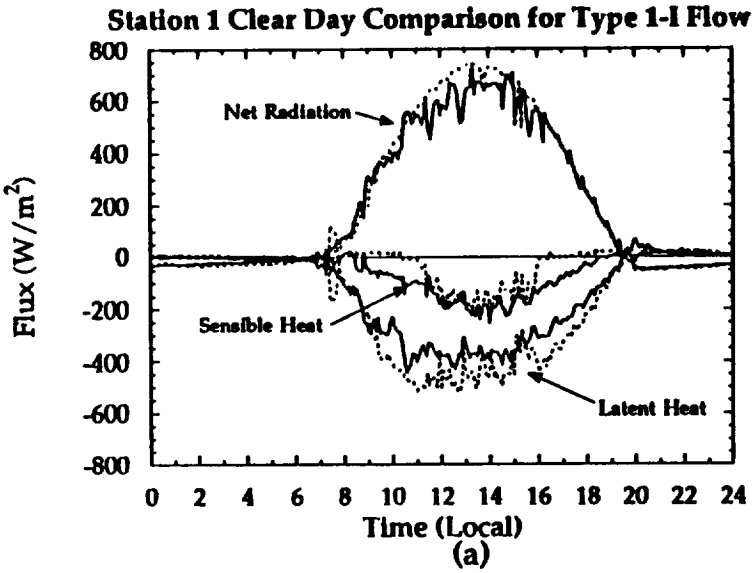

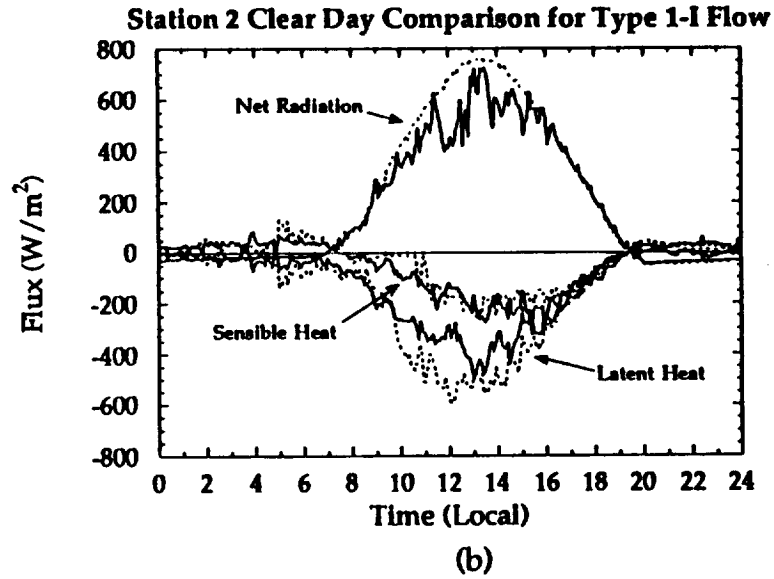

Figures 27(a) and 27(b): Comparison of average clear day values of net radiation, latent heat flux, and sensible heat flux to values on days of Station 1 (a) and Station 2 (b) Type 1-I flow. Clear sky values are dashed and the flux values are solid.

clear day between 1100 and 1500 LDT. The sensible heat fluxes show some tendency towards higher values in the morning, but show little difference in terms of magnitude or time of peak value between the clear day and Type 1-I flow during the rest of the day. In contrast, the latent heat fluxes show a large difference in magnitude and a notable difference between peak values. The station 2 Type 1-I day latent heat fluxes are more than 200 $W \bullet m^{-2}$ less than on clear days around noon and do not peak until about 1 hour after the clear day peak time. Net radiation and latent heat flux share a temporal connection that is clear in Figures 27(a) and 27(b). That is, as net radiation falls below clear sky values, so does latent heat flux, and as net radiation returns to clear sky conditions, so does the latent heat flux. Figures 27(c) and 27(d) show the percent clear sky values for net radiation and latent heat flux for the two stations under the Type 1-I flow regime. The data are only presented from 0800 to 2000 LDT because the values associated with low and noisy nighttime fluxes lead to meaningless percentage quantities. As expected from Figures 27(a) and 27(b), the net radiation and latent heat fluxes follow the same general trend of being greater than or equal to clear sky values before 0900 and less than clear sky values between 0900 and 1700. The station 1 percentage values indicate less cloud cover over the coastal site since values are closer to clear sky values than at station 2. Station 2 values reach a minimum of near 60% of clear sky values around noon.

Figure 27(e) is the partial energy budget for station 2 Type 2-I days as compared to clear sky conditions. The net radiation shows a drop off from clear sky conditions starting around 1200 LDT. This drop off is greatest around 1400 LDT and, unlike Type 1-I, it never retains the clear sky values. Likewise for the latent heat flux. The Type 2-I values decrease from clear sky conditions around

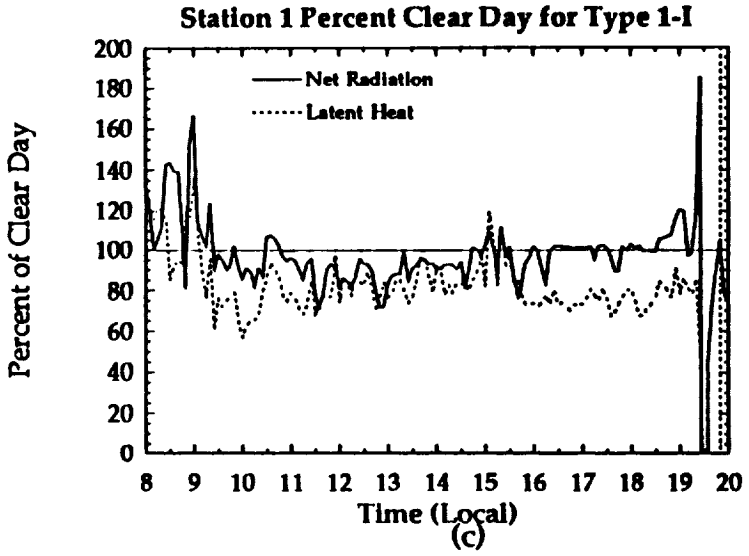

(c)

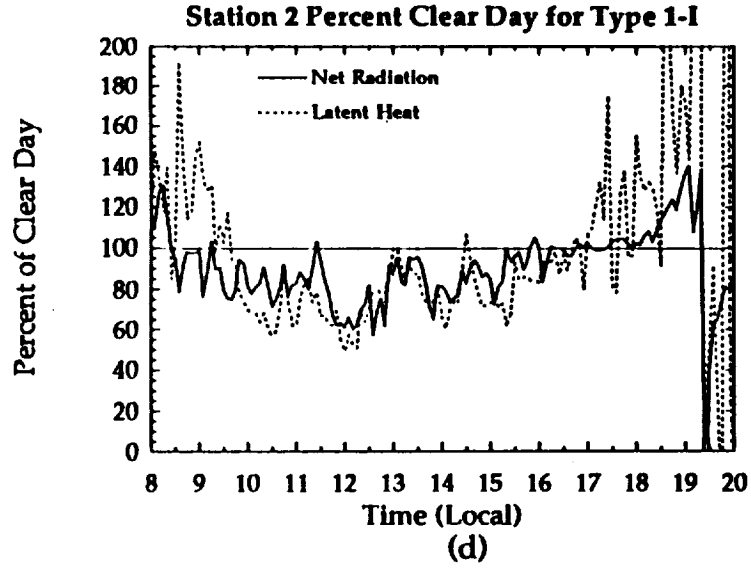

(d)

Figures 27(c) and 27(d): Station 1 (c) and Station 2 (d) percent of clear day values for net radiation and latent heat flux during Type 1-I flow.

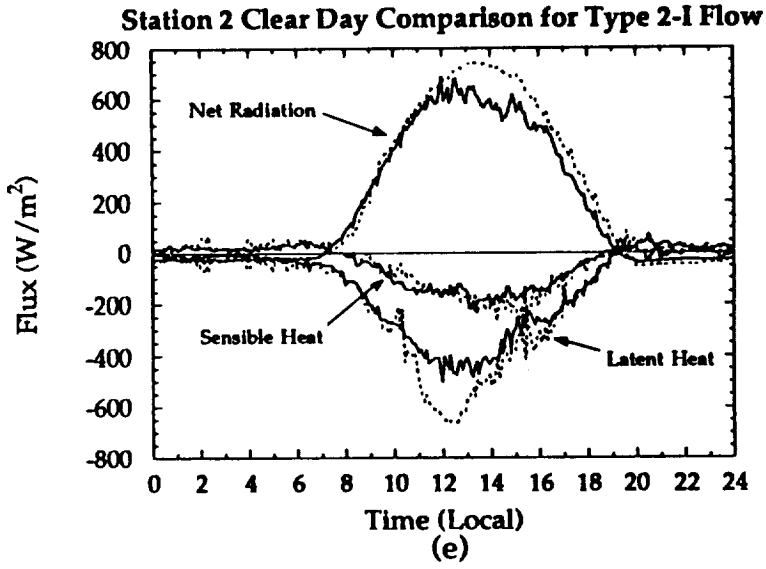

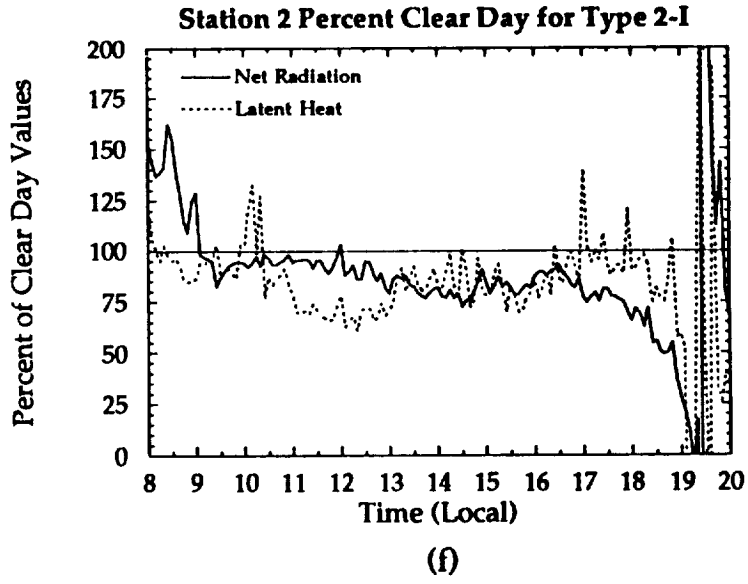

Figures 27(e) and 27(f): Comparison of average clear day values of net radiation, latent heat flux, and sensible heat flux to values on days of Station 2 Type 2-I flow. Clear sky values are dashed and the flux values are solid (e). Station 2 percent of clear day values for net radiation and latent heat flux during Type 2-I flow (f).

0900 LDT, reaching a maximum difference around 1230 LDT, and then never retaining the clear sky values. The sensible heat flux exhibits higher values than the clear sky values for the period from 0800 to 1200 LDT, and then follows along closely with the clear sky values.

The percentage of clear day values for station 2 Type 2-I flow, as seen in Figure 27(f), exhibit a very different profile from the Type 1-I flow. Starting around 0800 LDT, net radiation slowly decreases from greater than or equal to 100% of clear sky values to around 75% of clear day values near 1500 LDT. Then the rate of fall off increases, and the relative net radiation quickly drops to near 40% of the clear sky value around 1900 LDT. In the case of the latent heat fluxes, the difference between clear and non-clear days for Type 1 flow would appear to be in phase with the differential net radiation. For the Type 2-I case, however, the differential net radiation and differential latent heat fluxes are out of phase by 2-3 hours; see Figure 27(f). The greatest deficit in latent heat flux occurs around 1100-1200 LDT and is 65-75 % of the clear sky value. The greatest deficit in net radiation occurs between 1400 and 1500 LDT and is between 70-75 % of its clear sky value.

The most obvious difference in the two regimes is the time of maximum cloud cover as suggested by the net radiation profile, and, as will be seen, by the visible satellite imagery. The station 2 Type 2-I case, Figure 27(e) shows that the clouds start impacting the surface fluxes around 1200 LDT and continue through the rest of the day. By the time of inferred peak cloudiness, around 1400 LDT, the net radiation has dropped to just under 600 $W \bullet m^{-2}$. The net radiation during Type 1-I flow conditions, Figures 27(a) and 27(b), also drops to just under 600 $W \bullet m^{-2}$, however, it does this around 1200 LDT. This 2 hour differential, which appears to be a result of variation in cloudiness, can be explained in terms of the

prevailing flow generally associated with each flow type. In the case of Type 1 flow, that is generally southeasterly flow, any cloud development is advected to the west earlier in the day. In the case of Type 2 flow, which is most often southwesterly flow, the majority of the cloud coverage arrives from the west later in the day with the west coast sea breeze front as it penetrates far enough across the peninsula to meet and interact with the east coast sea breeze convergence zone. The comparison between active days showed no clear evidence for a lag as demonstrated on the inactive days. The Type 1 days showed earlier suppression of net radiation than does the Type 2 day, but due to the strong suppression of Type 2-A days, no clear lag signal can be found.

4.1.2 Active and Clear Day Comparison

The surface fluxes over the island on convectively active days were also examined relative to clear day fluxes. Figures 28(a-f) show the cases of Type 1-A and Type 2-A flows. Figures 28(a) and 28(b) show the partial energy budget for the cases of station 1 and station 2 Type 1-A flows. The greatest differential values of net radiation between clear and 1-A days, which are around 400 $W \bullet m^{-2}$ for station 1, occur just before noon. The net radiation is then able to recover to near clear day values, but then falls again and stays below clear day values for the remainder of the day. Examination of satellite imagery suggests that this is a result of cirrus anvils over the island after storms have dissipated. The sensible heat fluxes on the Type 1-A days are similar to the inactive days except they tend to stay slightly below that of clear days during the early afternoon. This is expected due to the lower amount of insolation received by the surface during convectively active days. The latent heat flux and net radiation behaves similarly in that they are lower than clear sky conditions. Up until around 0900 LDT, the latent heat flux at both sites seems to mirror clear sky conditions. By noon, there

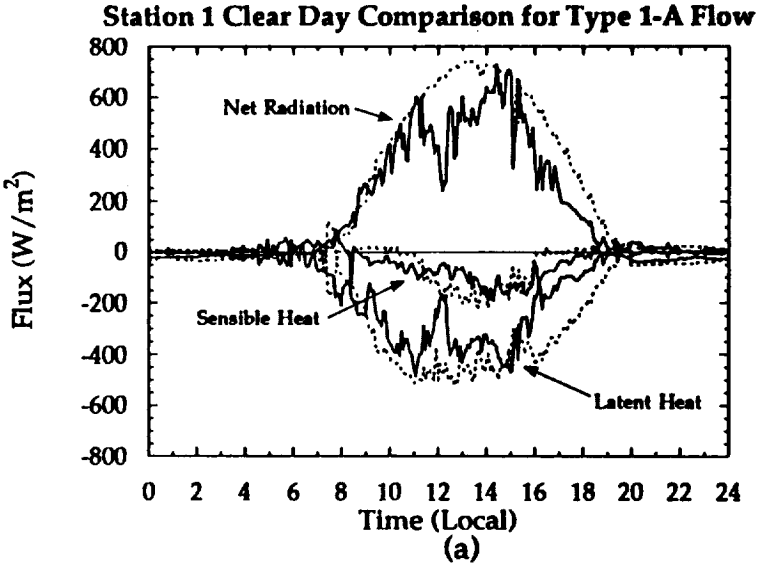

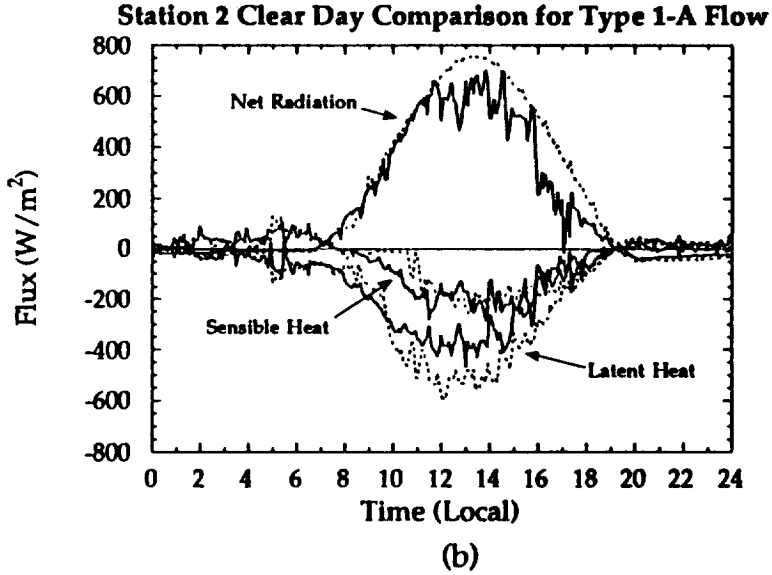

Figures 28(a) and 28(b): Comparison of average clear day values of net radiation, latent heat flux, and sensible heat flux to values on days of Station 1 (a) and Station 2 (b) Type 1-A flow. Clear sky values are dashed and the flux values are solid.

has occurred a significant departure from clear sky values. The Type 1-A days show a drop of as much as 300 $W \bullet m^{-2}$ from the clear sky values. This large deficit continues until around 1500 LDT when, for a short while, the Type 1-A values of latent heat return to clear sky values before again dropping off rapidly towards zero. This is displayed more clearly in Figures 28(c) and 28(d) which show the percentage clear day values for net radiation and latent heat flux for the two stations.

Figures 28(c) and 28(d) show how the net radiation and latent heat fluxes at each site respond in a similar manner to storms in the Type 1-A flow regime. Up until 1000 LDT, both flux values are greater than or equal to clear sky values and then descend to minimum values around 1200 LDT before returning to near clear sky values around 1500 LDT. Their minimum values at station 1 during this period are as low as 40% of clear sky values for net radiation and latent heat flux, and near 60% of clear sky values at station 2. After somewhat recovering around 1500, both flux values begin to drop and do not recover.

The Type 2-A flow displays the greatest observed departure from clear sky values. Figure 28(e) shows the partial energy budget for this regime. As early as 0900 LDT the net radiation and latent heat fluxes are below their clear sky counterparts. In fact, neither are able to retain their clear sky values at any point during daylight hours. The net radiation stays just below the clear values until about 1200 LDT when it falls to about 300 $W \bullet m^{-2}$ below the clear sky value and it remains below clear sky values for the remainder of the day. The sensible heat flux, however, is roughly the same as the clear sky value until about 1300 LDT when it falls below the clear sky value, and remains that way for the rest of the day. The latent heat flux mirrors the behavior of net radiation in that it stays near the clear values until 0800 LDT and then stays well below the clear sky

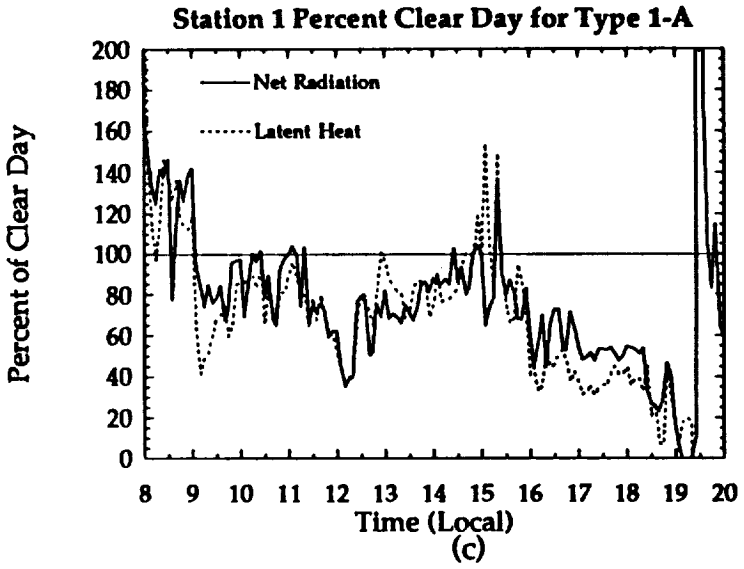

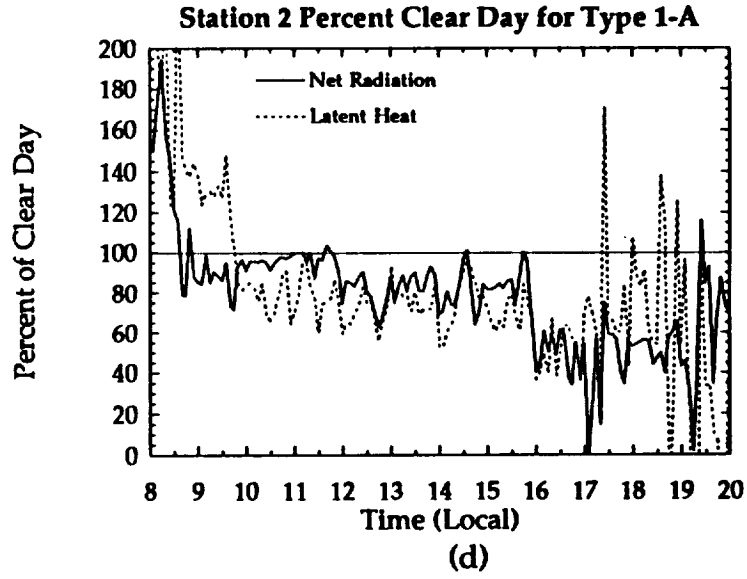

Figures 28(c) and 28(d): Station 1 (c) and Station 2 (d) percent of clear day values for net radiation and latent heat flux during Type 1-A flow.

values for the duration of the day. The maximum difference between latent heat on Type 2-A days and clear days occurs around 1200 LDT with a difference of 200 $W \bullet m^{-2}$. The minimum relative latent heat flux is reached before the rapid drop-off in net radiation.

The behavior of the fluxes can be seen more clearly in Figure 28(f), which shows the percentage of clear sky values for each flux term. Net radiation and latent heat flux again show very similar characteristics as in the Type 2-I case, with net radiation and latent heat maximum differential out of phase. By 0930 LDT they have both dropped to near 70% of clear sky values and then climb back to near 90% around 1200 LDT. They both then begin a steep decrease culminating near 1900 LDT with values as low as 15% of clear sky values. Days of Type 2 flow have been shown to produce the most intense convection, and these flux values confirm the classification, that is, the Type 2-A cases show the most marked departure from the clear sky values.

4.1.3 Soil and Sensible Heat Fluxes at the Two Stations

Sensible and soil heat fluxes were also analyzed in terms of percentage of clear sky values. Figures 29(a-f) show the results for the 4 types of regimes. Figures 29(a) and 29(b) show the cases of station 1 and station 2 Type 1-I. The sensible heat flux remains very near or above the clear sky values for the majority of the daylight hours. Soil heat flux stays near or below the clear sky values for Type 1-I flow. However, the soil heat fluxes do show some variability between the two stations.

Figures 29(c) and 29(d) show the case of Type 1-A flow. The soil heat flux differential remains above 100% for about half of the daylight hours for station 2 and mostly below clear sky values for station 1. The sensible heat flux at station 2 during Type 1-A flow remains near 100% until about 1500 LDT when it begins

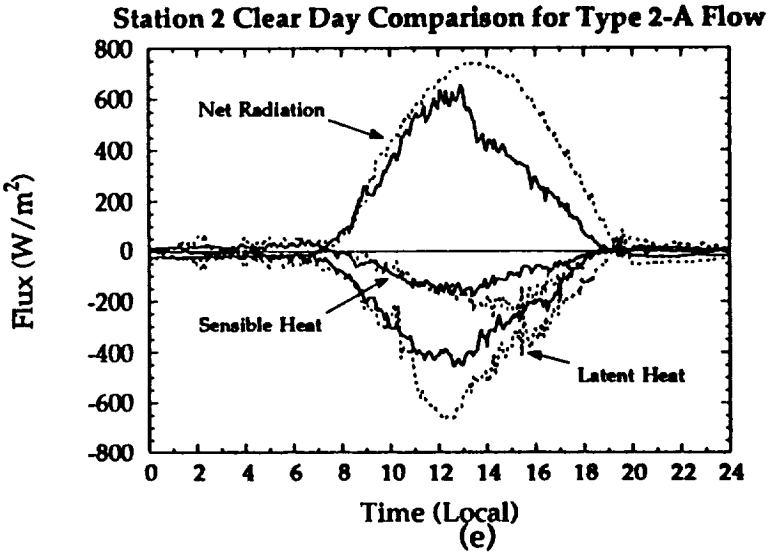

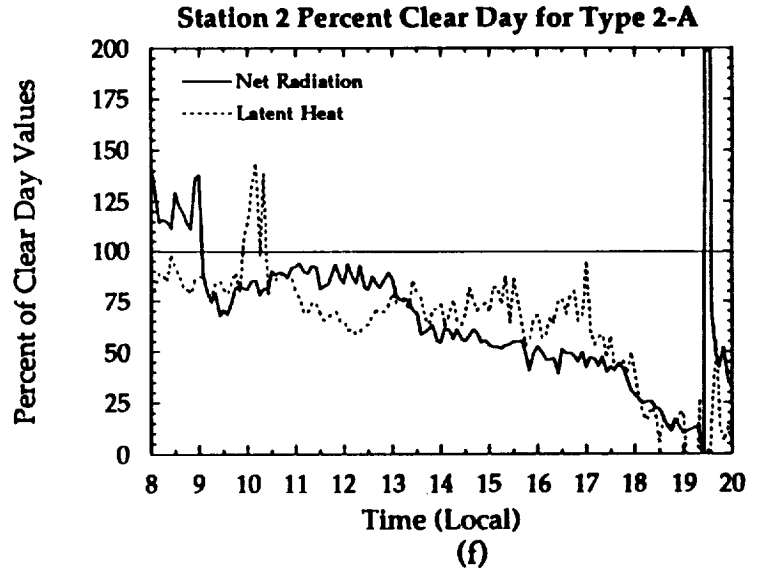

Figures 28(e) and 28(f): Comparison of average clear day values of net radiation, latent heat flux, and sensible heat flux to values on days of Station 2 Type 2-A flow. Clear sky values are dashed and the flux values are solid (e). Station 2 percent of clear day values for net radiation and latent heat flux during Type 2-A flow (f).

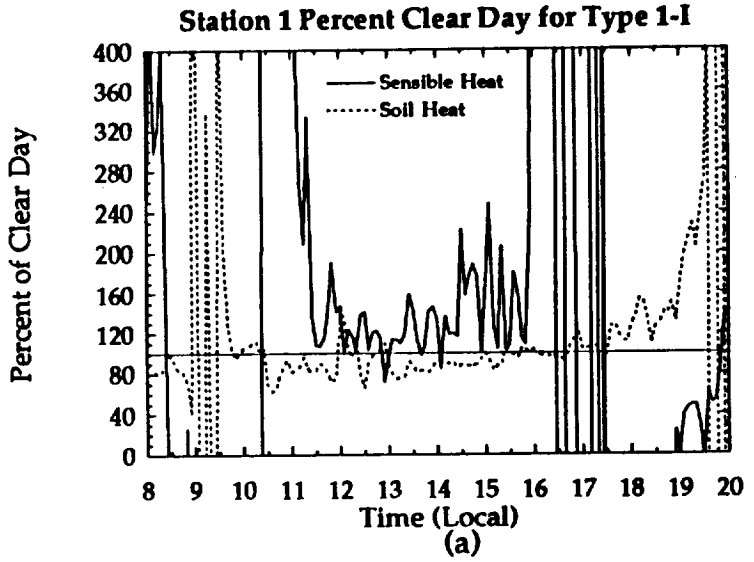

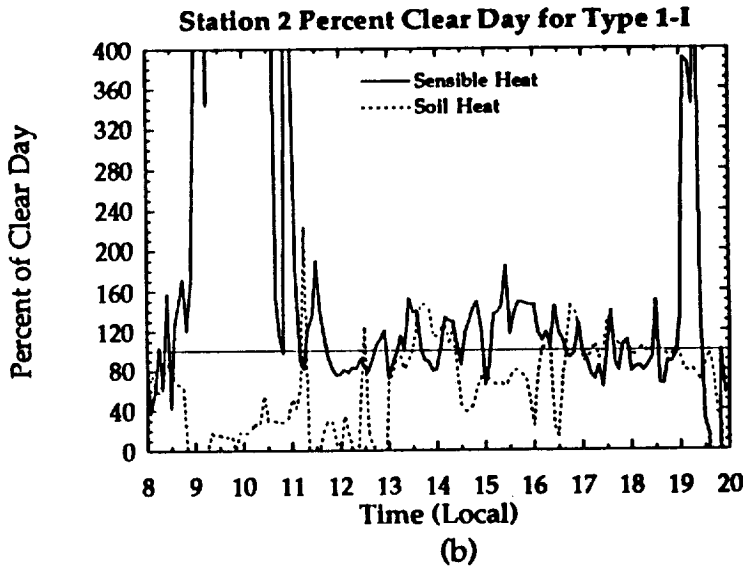

Figures 29(a) and 29(b): Percent of clear day values for sensible heat flux and soil heat flux for Station 1 (a) and Station 2 (b) Type 1-I flow.

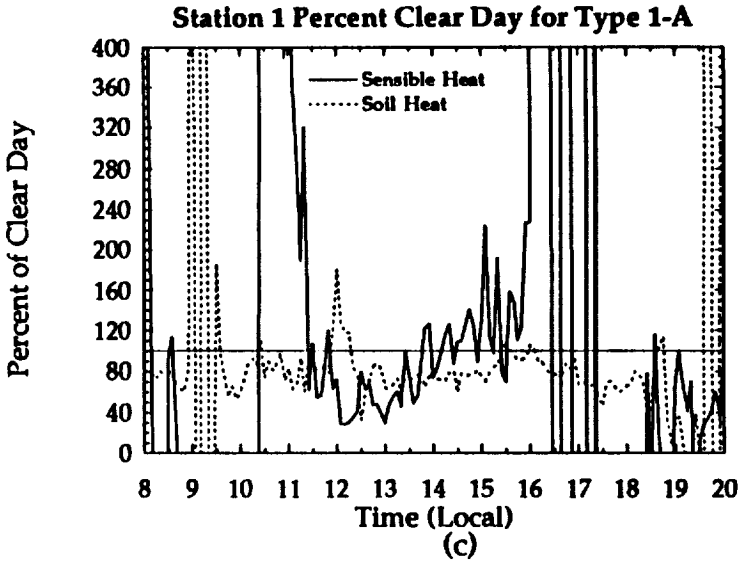

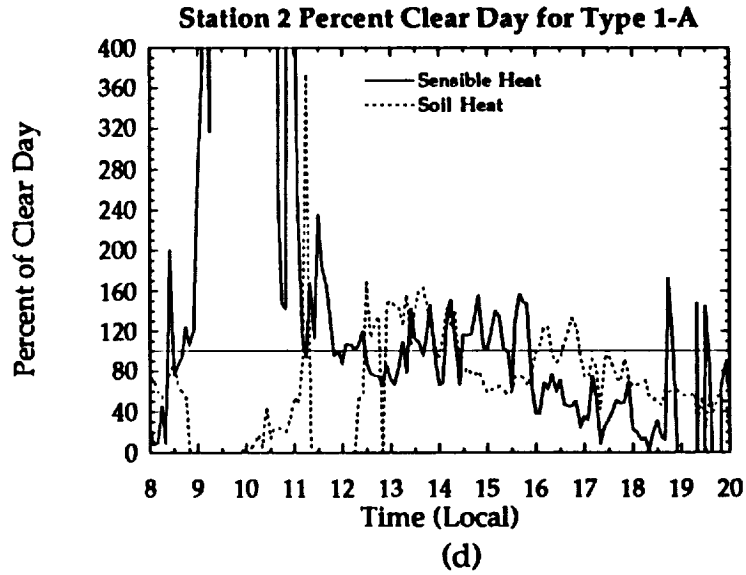

Figures 29(c) and 29(d): Percent of clear day values for sensible heat flux and soil heat flux for Station 1 (c) and Station 2 (d) Type 1-A flow.

to drop off steadily to around 40% at 1800 LDT. For station 1, the sensible heat is well below clear sky values until around 1400 LDT when it increases to above clear sky values. Figures 29(a) through 29(d) indicate a site sensitivity in the soil and sensible heat fluxes.

For station 2 Type 2-I, as seen in Figure 29(f), the soil heat flux percentages are, in general, above 100% in the morning and near or below 100% in the afternoon. The sensible heat drops below clear sky values around 1100 LDT and, in general, stays there for the remainder of the day. For the case of station 2 Type 2-A, as seen in Figure 29(e), the soil heat and sensible heat fluxes before noon tend to be 100% or more, then decreases steadily from 80% to 20% over the course of the day from 1200 to 1900 LDT. Figures 29(a) through 29(f) suggest that the soil and sensible heat fluxes respond to differences in flow regime and cloudiness, but also suggest that the soil heat fluxes may be heavily influenced by the physical properties of the soils at a given site. A summary of the total energy for each flux regime can be found in Table 8.

4.1.4 Active and Inactive Day Comparison

Because of the scarcity of cloud-free days around Merritt Island, an additional analysis based on inter-regime comparison was performed. That is, comparisons between Type 1-I and Type 1-A , and between Type 2-I and Type 2-A . Figures 30(a) and 30(b) show the partial energy budget for these comparisons. Figure 31(a) shows how net radiation and latent heat behave for active and inactive days during Type 1 flow. The values remain near each other until around 1600 LDT when the storm day values steadily decrease, reaching a minimum value of 25% around 1900 LDT. Because the magnitudes are lower than the other fluxes, sensible and soil heat fluxes are noisier signals, as seen in Figure 31(b). Like net radiation and latent heat, sensible heat and soil heat flux

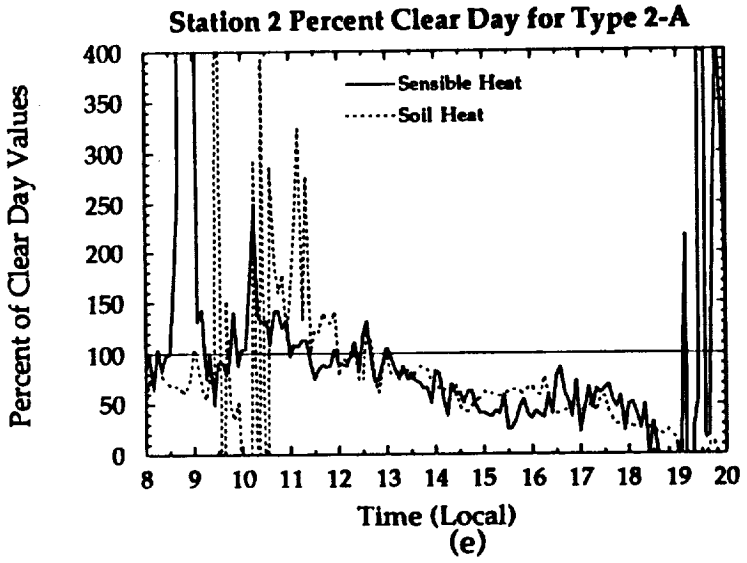

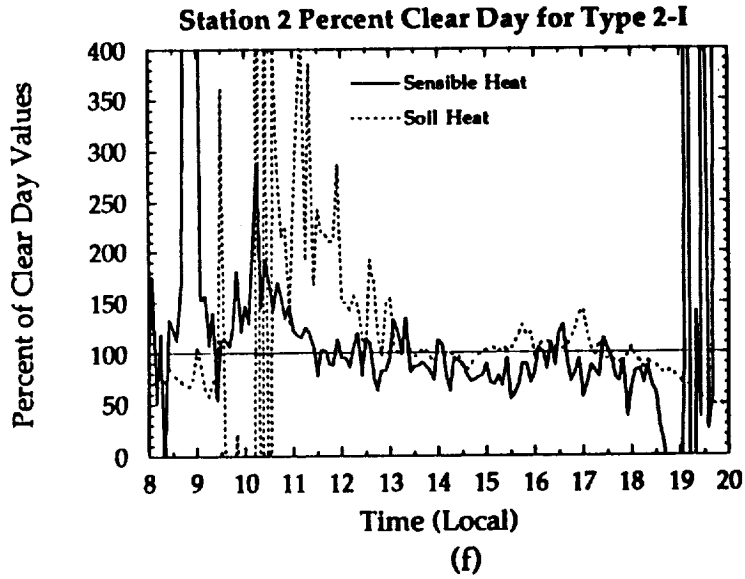

Figures 29(e) and 29(f): Percent of clear day values for sensible heat flux and soil heat flux for Station 2 Type 2-A flow (e) and Type 2-I flow (f)

Table 8: Total energy for average day for each regime. (Joules)

	Q^* (x 10^7)	QE (x 10^6)	QH (x10^6)	QG (x 10^5)
Type 1 Clear	1.81	14.20	3.93	5.61
Type 1-I	1.57	11.20	4.30	9.29
Type 1-A	1.37	10.90	3.05	6.75
Type 2 Clear	1.80	14.48	3.90	6.72
Type 2-I	1.58	11.90	3.00	9.75
Type 2-A	1.24	9.30	2.94	4.34

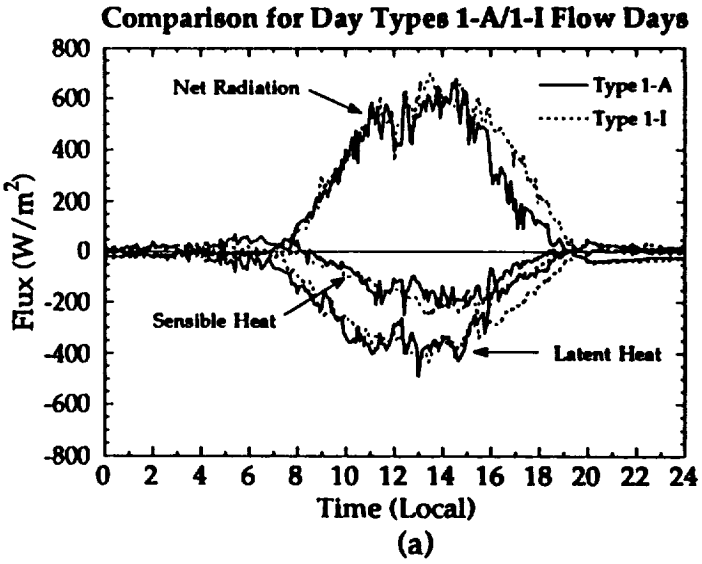

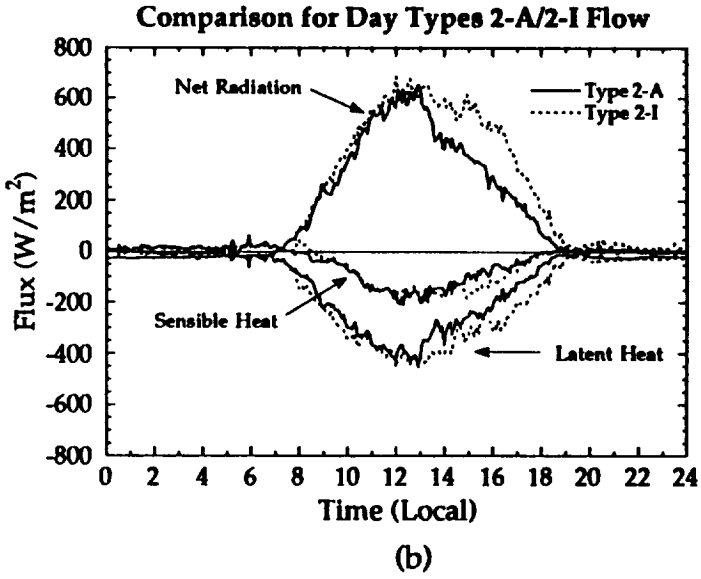

Figures 30(a) and 30(b): Comparison of Type 1-A (solid line) and 1-I flow (dashed line) for the net radiation, latent heat and sensible heat (a). Comparison of Type 2-A (solid line) and 2-I flow (dashed line) for the net radiation, latent heat and sensible heat (b).

remain near the 100% value until around 1600 LDT when they steadily decrease to around 60-70% of the inactive day values, recover between 1500 and 1600 LDT, and then steadily decrease over the next 3 hours to around 50% of inactive day values. Figure 31(c) shows the net radiation and latent heat comparisons for Type 2 flow regimes. Just as in the Type 1 flow regime, the values stay near 100% of inactive day values until around 1300 LDT when they begin a steady decrease to 30% near 1900 LDT. The sensible heat and soil heat fluxes also behave similarly in the two flow regimes as seen in Figure 31(d). All of the fluxes for active days show some deficit as compared to inactive days. This is one more indication that cloud shading, and associated rainfall, are playing the dominant role in determining fluctuations in the magnitudes of surface fluxes of latent and sensible heat.

4.1.5 Composite Diurnal Averages

Figures 32(a-f) summarize the results of the analysis of diurnal averages and show plots of mean satellite visible reflectance and variance in reflectance for the KSC satellite box in Figure 15, the mean surface fluxes measured at the FSU flux sites, the surface area-averaged wind divergence over the island and the rainfall measured at the PAM stations located on Merritt island and at the FSU flux sites. The figures also show the close connection between the satellite analysis and what is happening on the ground. The top panel shows the satellite reflectance. The second panel shows the surface fluxes. The third and bottom panels show the surface wind divergence and rainfall, respectively. Figures 32(g) and 32(h) show air temperature, u and v component of wind, and spedific humidity as measured at the FSU-SREB stations for typical days of Type 1 and Type 2 flow.

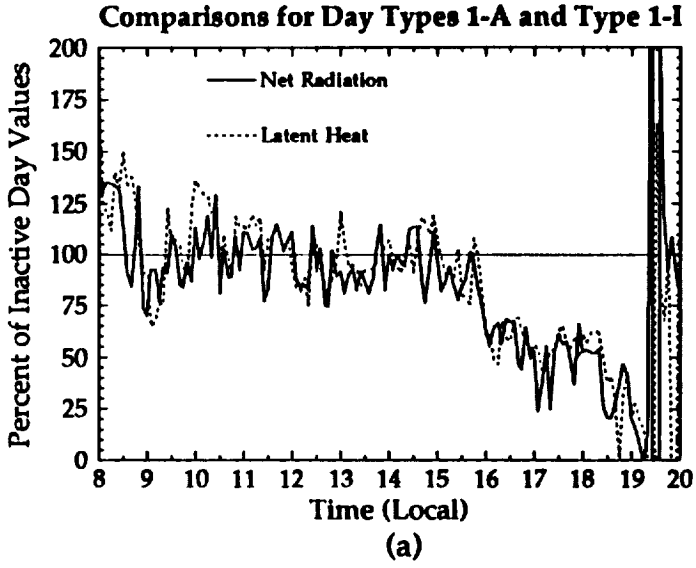

(a)

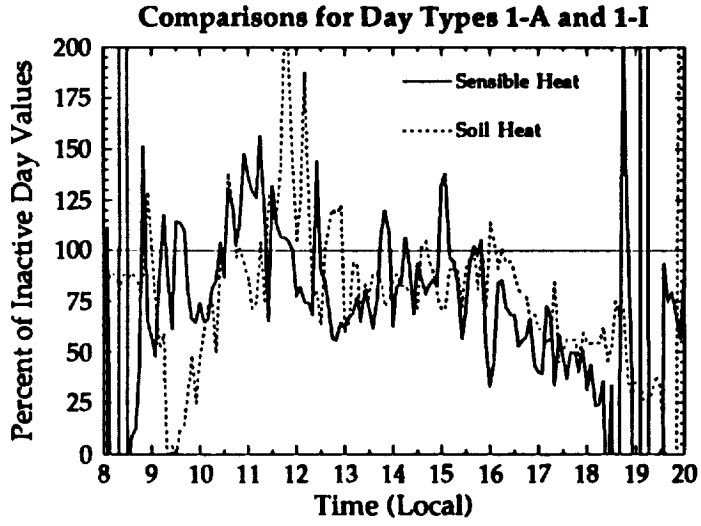

(b)

Figures 31(a) and 31(b): Percent of inactive net radiation (solid line) and latent heat flux (dashed line) for Type 1 flow (a) and percent of inactive sensible heat flux (solid line) and soil heat flux (dashed line) for Type 1 flow (b).

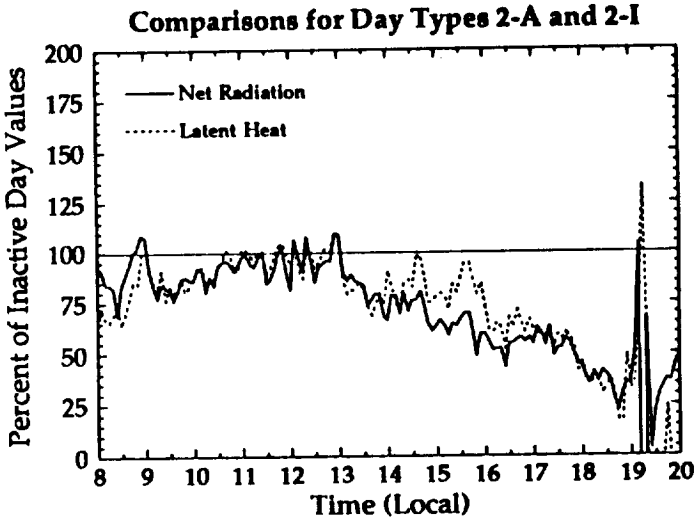

(c)

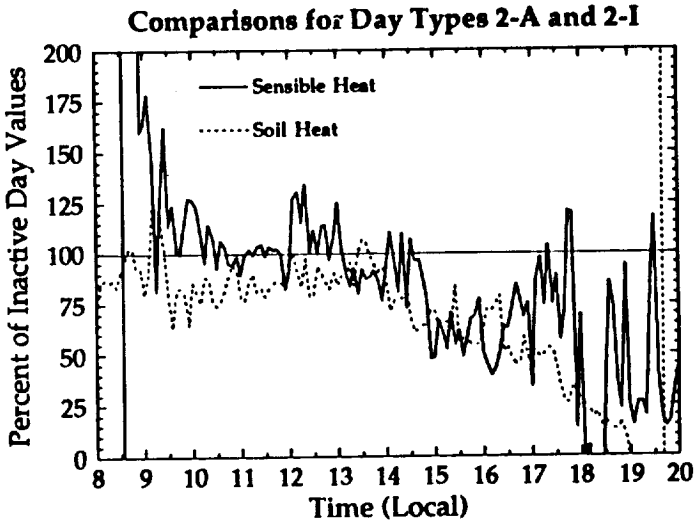

(d)

Figures 31(c) and 31(d): Percent of inactive net radiation (solid line) and latent heat flux (dashed line) for Type 2 flow (c) and percent of inactive sensible heat flux (solid line) and soil heat flux (dashed line) for Type 2 flow (d).

Figures 32(a) and 32(b) show the overall analysis for the disturbed days at the beginning of the experiment and the offshore hurricane days at the end of the experiment. The surface wind divergence shows no tendency in either case to develop a sea breeze circulation. The hurricane case is virtually rain free, whereas the disturbed case shows rainfall throughout the day. The offshore hurricane day fluxes are close to the clear day fluxes discussed above and the amount of cloud cover as seen in the top panel of Figure 32(a) is small. The disturbed day fluxes are largely suppressed, especially in the afternoon, due to heavy rainfall, while the satellite variance and average reflectance values are very high.

Figures 32(c) and 32(d) show the general situation for Type 1 flow. The active flow profiles are given in the left hand column, whereas the inactive profiles are seen in the right hand column. The satellite parameters show much less activity than on the disturbed days in Figure 32(b), but the Type 1-I reflectance analysis indicates activity in two bursts after 1200 LDT, with increasing reflectance over the island towards evening. There is some rainfall between 1700 and 1900 LDT. The twin peaks in reflectance variance are a result of early development of small cumulus fields followed by a relative clearing, which in turn is followed by larger, precipitating convective clouds and some anvil outflow in the late afternoon. The surface fluxes follow the cloud evolution, and the average reflectance maximum also suggests that the storms are smaller and occur later. There is a definite tendency towards a sea breeze circulation in the surface divergence pattern. The Type 1-I flow of Figure 32(d), shows little convection in the satellite image, some departure from clear sky net radiation before noon, a weakened sea breeze circulation and very small amounts of pre-noon rainfall.

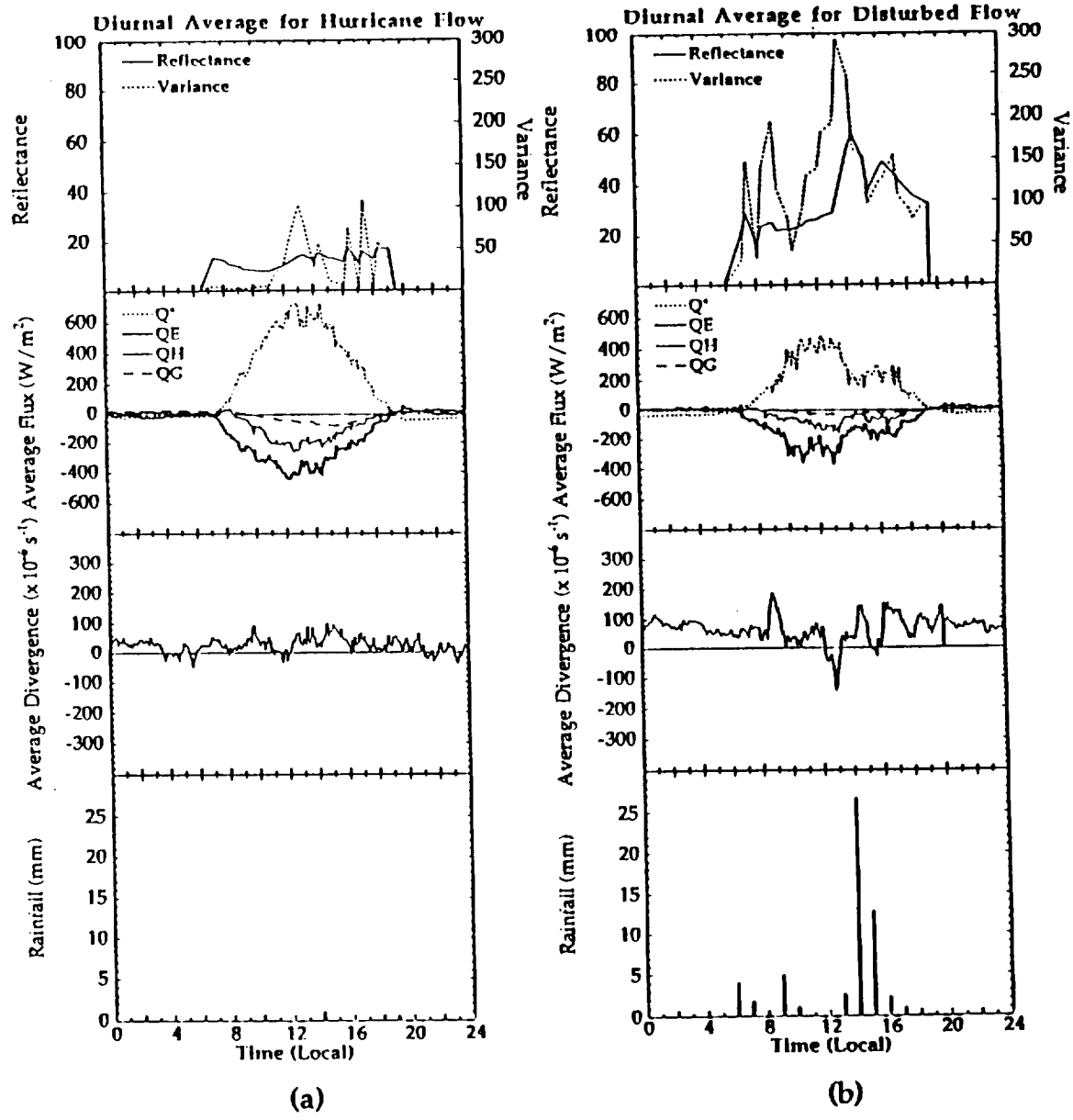

Figures 32(a) and 32(b): Diurnal average and composite of satellite reflectance (solid line) and variance of reflectance (dashed line) in the top panel, net radiation (dashed line), latent heat flux (heavy solid line), sensible heat flux (thin solid line), and soil heat flux (long dashed line) in the second from the top panel, divergence over Merritt Island (solid line) in the third from the top panel and hourly accumulative rainfall (bottom panel) for days of hurricane flow (a) and disturbed flow (b).

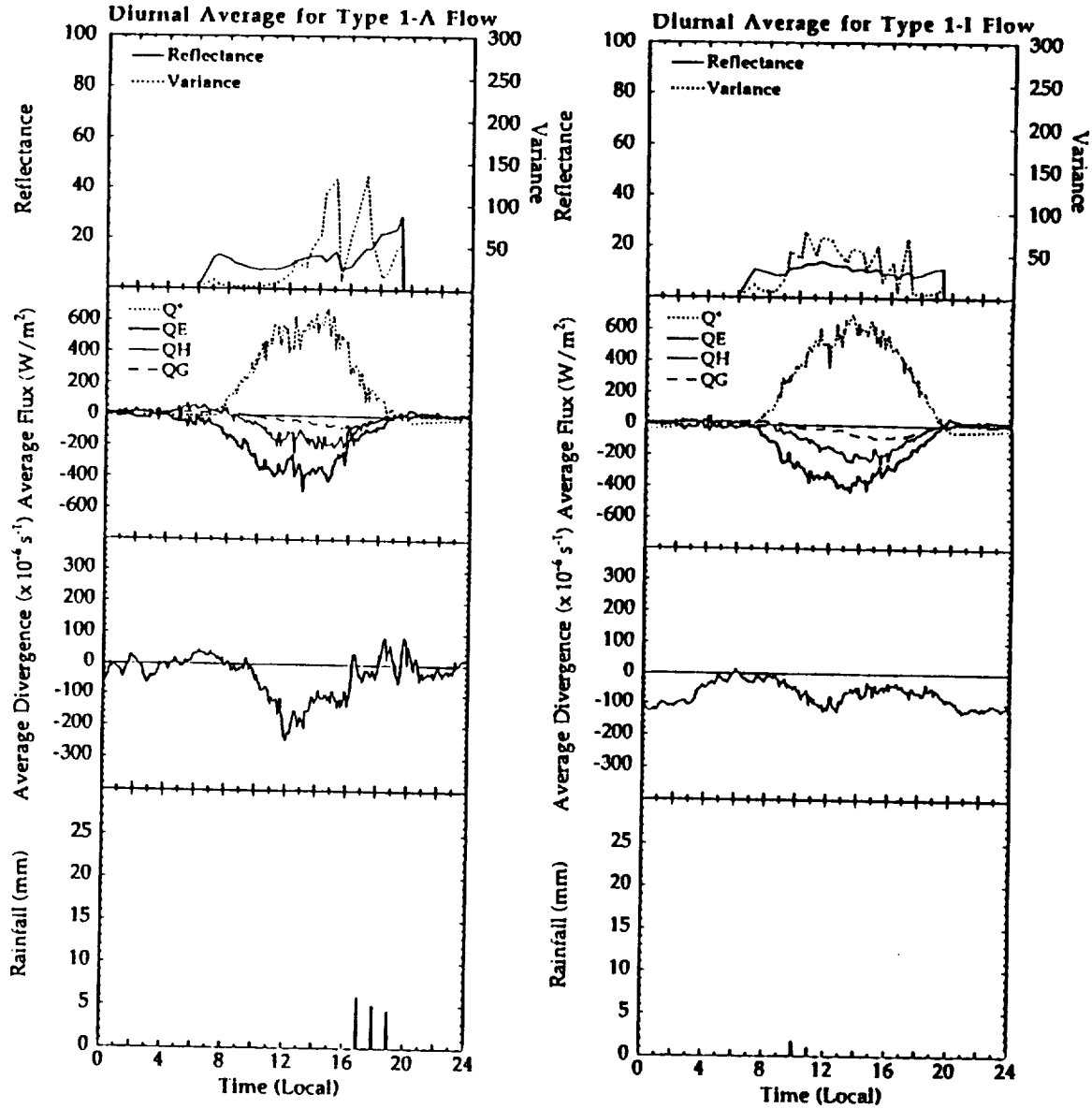

(c) (d)

Figures 32(c) and 32(d): Diurnal average and composite of satellite reflectance (solid line) and variance of reflectance (dashed line) in the top panel, net radiation (dashed line), latent heat flux (heavy solid line), sensible heat flux (thin solid line), and soil heat flux (long dashed line) in the second from the top panel, divergence over Merritt Island (solid line) in the third from the top panel and hourly accumulative rainfall (bottom panel) for days of Type 1-A flow (c) and Type 1-I flow (d).

The Type 2-A flow produces the most intense convection in the satellite analysis; top panel of Figure 32(c). The damping of net radiation and consequently of latent and sensible heat fluxes follows the convection, and the island divergence shows a clear sea breeze oscillation. Heavy afternoon showers occur mostly between 1500 and 2200 LDT. The Type 2-I flow indicates little convection in the satellite reflectance panel, a strong, clear sea breeze signal in the divergence field, and moderate rainfall around dusk or 2000 LDT. Inter-flow comparison shows that the satellite reflectance on Type 1-I days is indeed higher earlier in the day than on Type 2-I days and is also more intense on Type 2-A days than on Type 1-A days.

Figures 32(g) and 32(h) show FSU-SREB measurements for July 21, a typical Type 1 day and July 28, a typical Type 2 day. The top panel, which shows the air temperature at 2.75 meters, exhibits the expected strong diurnal cycle. The Type 2 day air temperature is slightly higher than the Type 1 day and the Type 1 day shows a more level peak temperature. This may be explained by the appearance and persistence of pre-noon clouds associated with Type 1 flow. The second and third panel shows the u and v components of the wind as measured at 3.0 meters at the FSU stations. Even at this low height, the u component shows a trend towards an easterly component in Type 1 flow and a trend towards a westerly component in Type 2 flow. The specific humidities show similar behavior in each of the two flow regimes.

The analysis in this section demonstrates conclusively that the interruption of net radiation flux into the surface layer by clouds is the major controlling factor in determining the magnitude and partitioning of the components of the surface energy budget, and that a loss of net radiation because of interposed cloudiness results in a larger decrease in latent heat flux than

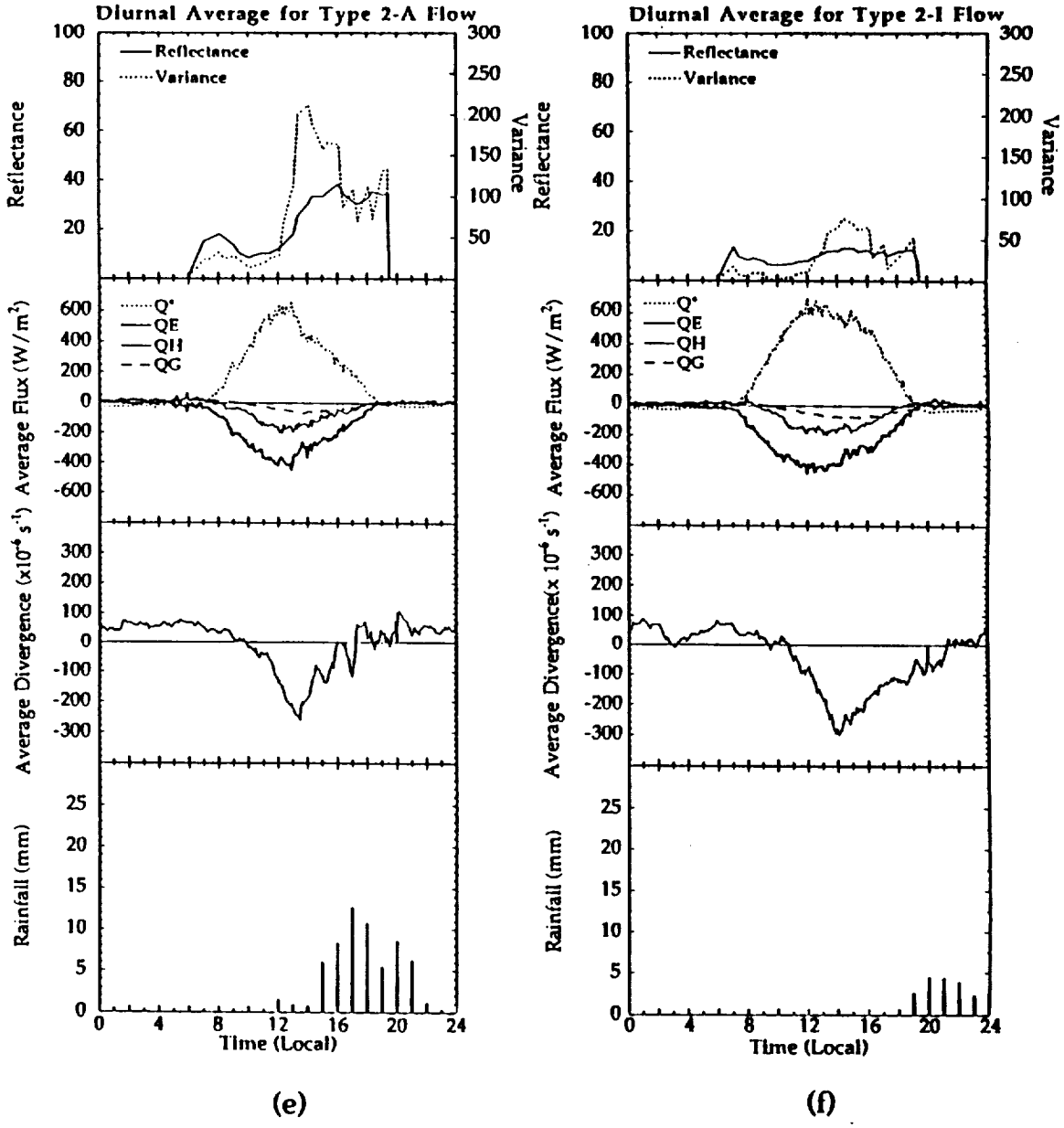

Figures 32(e) and 32(f): Diurnal average and composite of satellite reflectance (solid line) and variance of reflectance (dashed line) in the top panel, net radiation (dashed line), latent heat flux (heavy solid line), sensible heat flux (thin solid line), and soil heat flux (long dashed line) in the second from the top panel, divergence over Merritt Island (solid line) in the third from the top panel and hourly accumulative rainfall (bottom panel) for days of Type 2-A flow (e) and Type 2-I flow (f).

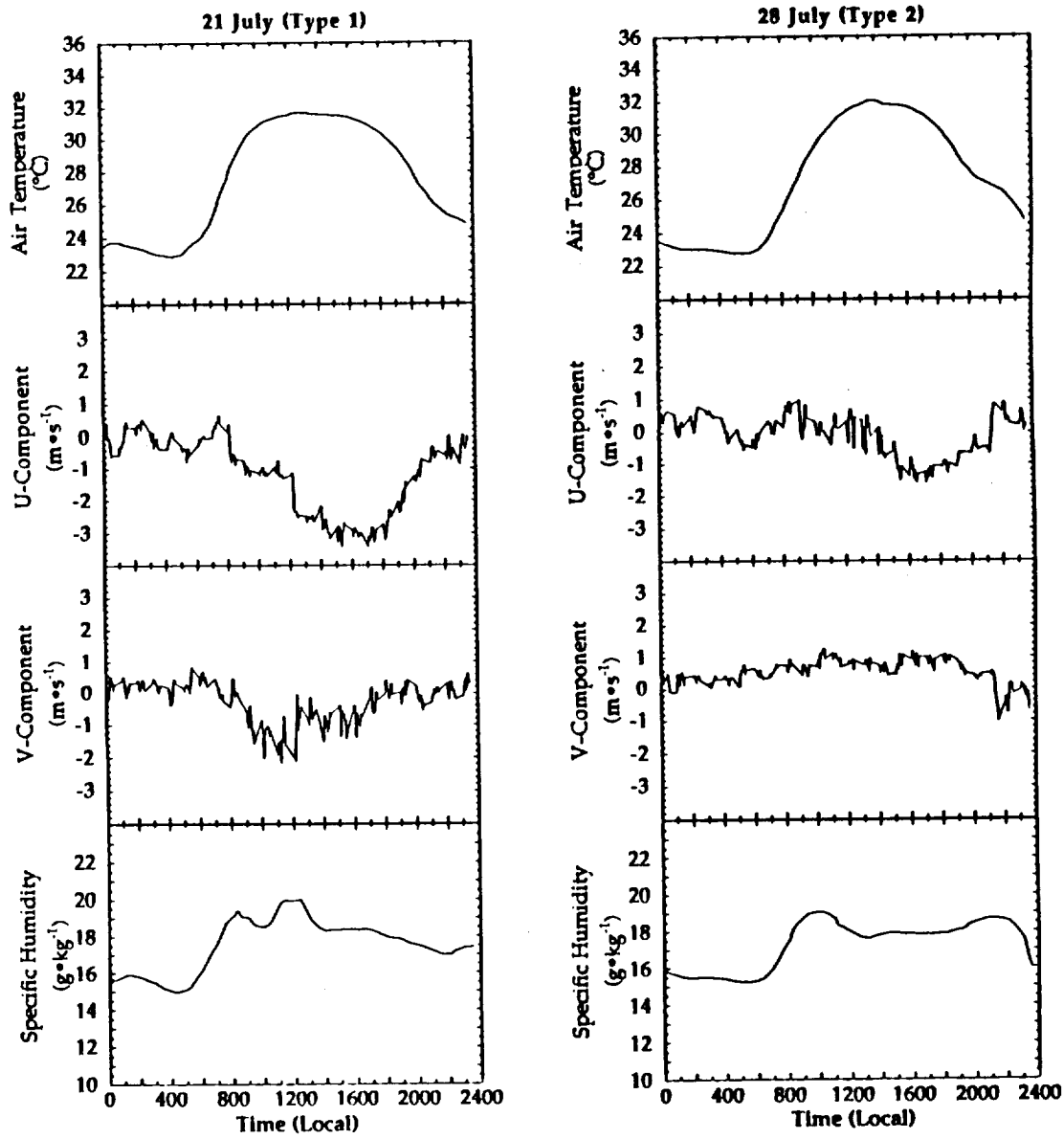

Figures 32(g) and 32(h): Meteorological data taken from the FSU-SREB Stations on July 21, 1991 (g) and July 28, 1991 (h). Top panel shows air temperature, second and third panels show u and v component of wind, respectively, and the bottom panel shows the specific humidity.

sensible heat flux, possibly in response to changes in transpiration rates in vegetation at the surface, and the partial closing of plant stomata under conditions of cloudiness.

4.2 The Surface Fluxes Beneath a Composite Storm

In this section, the construction of a composite site-specific downdraft event is discussed. The purpose of the compositing analysis is to investigate the effects of rain-driven downdrafts at a fixed location directly underneath the rainshaft of a given thunderstorm. The ultimate aim is to quantify the interaction between the downdraft air and the surface fluxes, in such a way that a Lagrangian storm outflow could be produced by time-space conversion and appropriate assumptions regarding spatial symmetry in rainfall and downdraft intensity. The composite downdraft event is constructed in 4 steps:

Step 1:

Using the gridded divergence plots, the KSC divergence grid locations collocated around each of the FSU sites were used to estimate the divergence immediately over each site. This was done for both sites and for all days of the experiment. Inspection of the area-averaged divergence time series over each site disclosed 30 cases when the time series suggested a direct hit by a downdraft. Examination of the KSC divergence animation sequences narrowed the candidate cases to 12 direct hits over both or either of the FSU flux sites. Of these 12 cases, 6 cases were immediately eliminated because the fine-wire thermocouples used by the DEW-10 system were destroyed by the heavy rainfall from the storm. While unfortunate, this in itself is conclusive evidence that the selection of downdraft cases is unquestionable. One more case, that of 10 August, was rejected for inclusion in the composite because the storm occurred very late in the day, and as such, not representative of the afternoon storm events

which are most common. That left five clear-cut candidates for the composite. These are listed in Table 9, along with the original 12 downdraft candidates.

Step 2:

Data visualization of the KSC network divergence over Merritt Island, which was used in Step 1 to determine candidate days for compositing, was also used to determine the exact time at which the downdraft arrived over one or both of the FSU flux sites, and to ensure that the site was located at the center of the downdraft outflow at that time. The times of arrival of the downdrafts over the sites are included in Table 9.

Step 3:

The mean time of day that a downdraft arrived over an FSU flux station was close to 1535 LDT. In order to eliminate diurnal effects from the composited fluxes, the departures from a reference diurnal flux cycle were calculated for each event. The reference diurnal cycle of radiative and thermodynamic fluxes was comprised of the averages of all the clear day cases used in Section 4.1. The reference day cycle is depicted in Figures 33(a) and 33(b). A list of the days used in the reference composite can be found in Table 10.

Step 4:

For each downdraft event, the surface energy budget fluxes were composited about the time of arrival of the downdraft over the site for a period of 10 hours before and 10 hours after the maximum downdraft. The raw composites for net radiation, sensible, latent and soil heat fluxes are shown in Figures 34(a - d).

For each of the 5 raw signals classified by the four steps outlined above, the percentage of reference day flux was calculated each five minutes by:

Table 9: Days selected for use in the storm composite.

Date (Julian)	Time	Station	Flow Regime	Composited
16 July (197)	16:45	1	Type 1-A	Yes
25 July (206)	17:35	1	Type 2-A	No
26 July (207)	15:55	1	Type 2-A	No
26 July (207)	16:10	2	Type 2-A	Yes
30 July (211)	13:55	2	Type 2-A	No
31 July (212)	14:40	1	Type 2-A	No
31 July (212)	15:40	2	Type 2-A	No
01 Aug (213)	14:35	1	Type 2-A	Yes
01 Aug (213)	14:30	2	Type 2-A	Yes
05 Aug (217)	15:45	2	Type 2-A	Yes
09 Aug (221)	17:30	2	Type 2-A	No
10 Aug (222)	19:15	2	Type 2-A	No

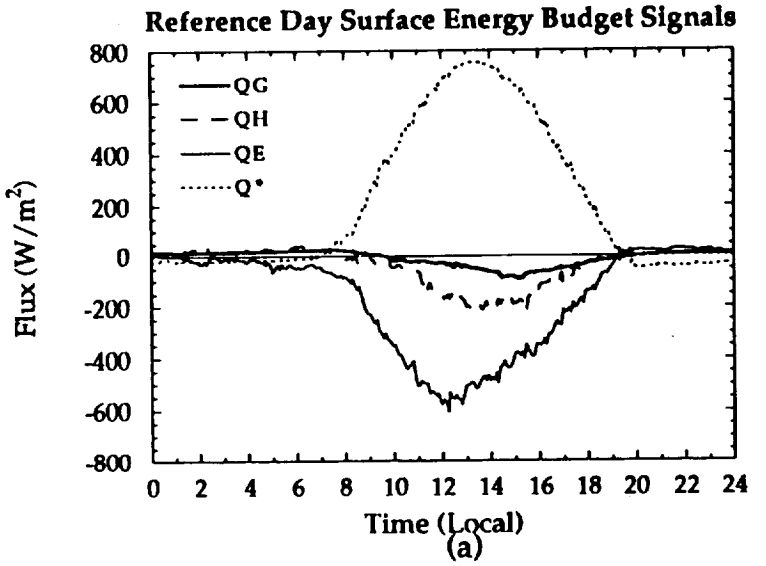

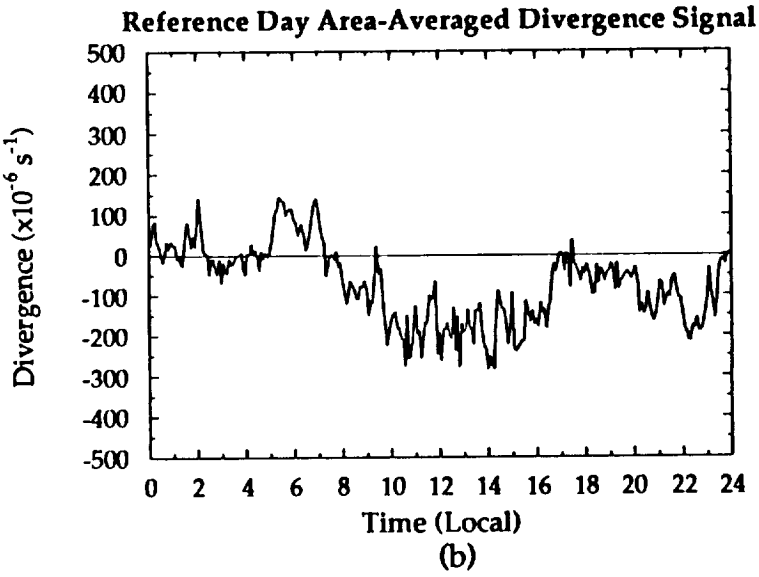

Figures 33(a) and 33(b): Diurnal average of net radiation (short dashed line), latent heat flux (thin solid line), sensible heat flux (long dashed line) and soil heat flux (heavy solid line) for the 3 clear days at the FSU flux sites (a). Diurnal average of low level divergence for the 3 clear days at the FSU flux sites (b).

Table 10: Days used for the clear day signal in the composite storm.

Date (Julian)	Station	Flow Regime
28 July (209)	2	Type 2-I
06 August (218)	1	Type 1-I
06 August (218)	2	Type 1-I

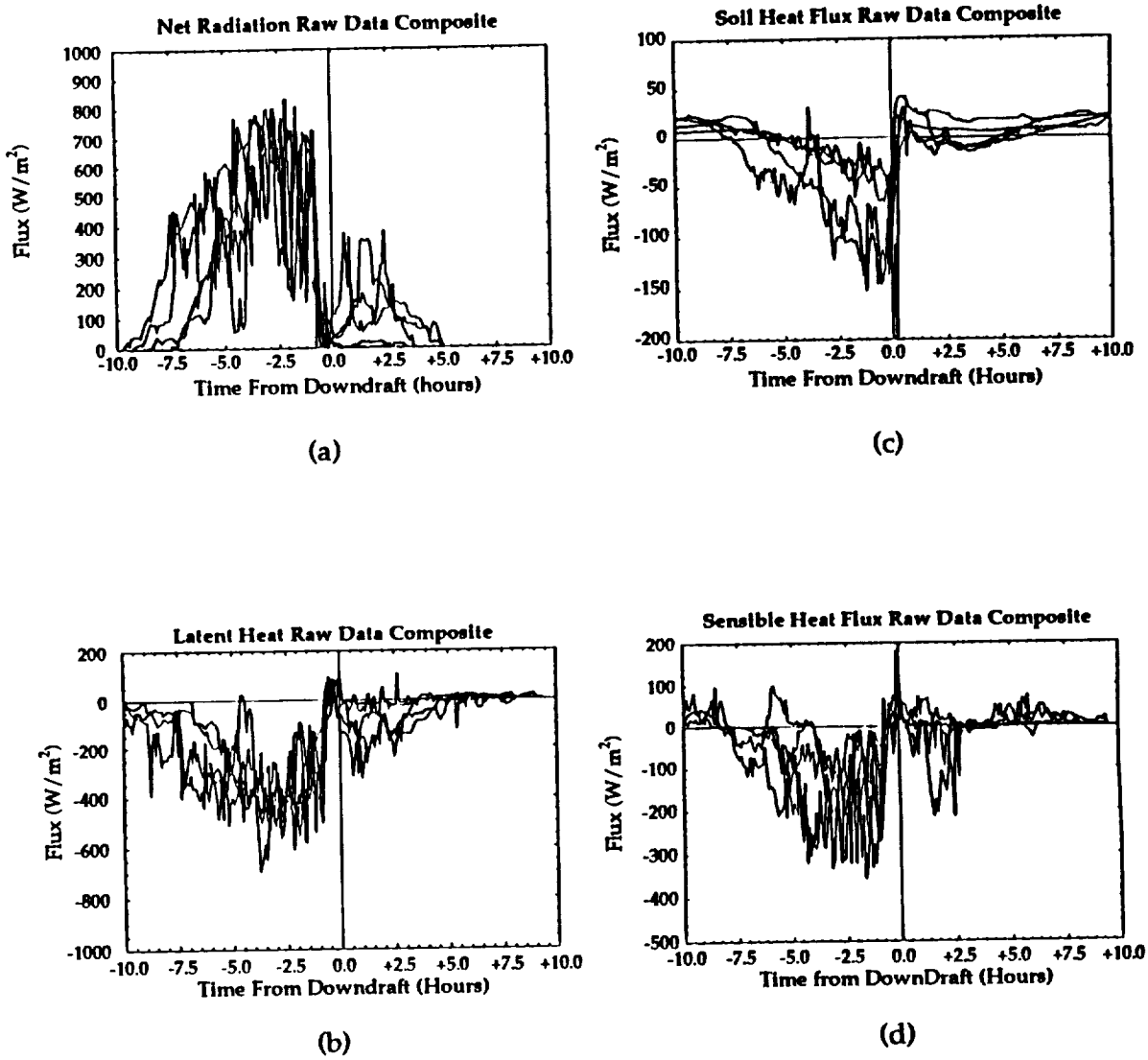

Figures 34(a) - 34(d): Composite of raw net radiation (a), latent heat flux (b), soil heat flux (c), and sensible heat flux (d) for the 5 storm cases over the FSU sites.

$$P_i(t) = \frac{V_i(t)}{R(t)} \tag{19}$$

where $P_i(t)$ is the percentage of clear sky values for event i at time t on the reference day. $V_i(t)$ is the actual magnitude of the flux for event i at time t, on the day being composited, and R(t) is the value of the same flux at time t on the reference day. The values of $P_i(t)$ were then composited about the time of maximum downdraft for each case i, in the same way that the raw fluxes were composited in Figures 34(a) and 34(b). The result is a new time series of $P_i(T)$, were T is now the time relative to the maximum downdraft. The average percent of reference day flux was then calculated from:

$$\overline{P} = \frac{1}{5}\sum_{i=1}^{5} P_i(T) \tag{20}$$

Figure 35 shows the results of the compositing process for ± 5 hours from the maximum downdraft. The ± 5 hour composite exhibits most of the characteristics associated with a rainfall event. All of the parameters in question show a very strong connection to the low level winds. This is evident from how closely each signal has conformed to a compositing process that was based solely on observed wind patterns. The variance in the GOES-VIS image over the island (Figure 35, top panel), reaches a maximum just before the peak downdraft, while the average reflectance reaches a maximum just after the peak divergence. This is consistent with previous explanations in terms of rising spatial heterogeneity of reflectance as the storms enter the satellite scene field of view followed by a lowering of variance and a relatively invariant average reflectance as the scene is filled by anvils from the mature stage cell.

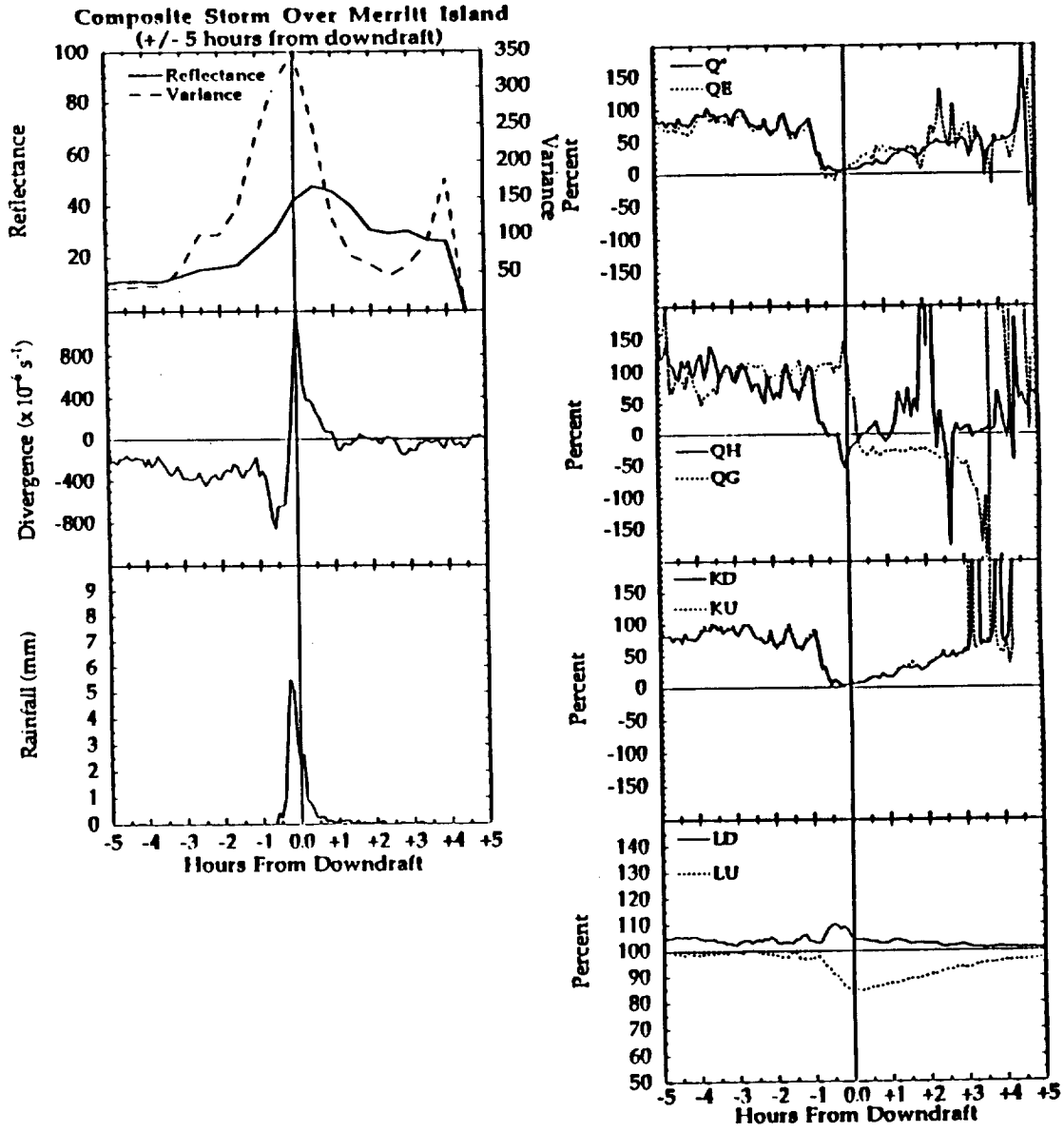

Figure 35: Composite storm picture including satellite reflectance and variance of reflectance, percent of clear day values for net radiation, latent heat flux, sensible heat flux, soil heat flux, downwelling solar and longwave radiation, upwelling solar and longwave radiation, average divergence, and averaged rainfall.

As a consequence of loss of downwelling solar radiation beneath the rainshaft, the net radiation in the composite storm approaches 10% of its reference day value just before the time of peak divergence (Figure 35, second panel). The latent heat departure actually shows a minimum of -10% of its reference day value at the same time. This negative percent is a result of the latent heat flux becoming positive (towards the ground) just before the downdraft moves over the site. This is also evident in the raw composite as seen in Figures 34(a) and 34(b). This may be a result of moisture convergence in the gust front convergence zone immediately ahead of the rainshaft, or the advection of saturated downdraft air over the site.

The sensible and soil heat fluxes show similar behavior (Figure 35, panel three). The composite sensible heat flux departures decrease from near reference day values and reach a minimum value of -50 % at the time of the maximum downdraft. This reversal of sign is most likely a result of rainfall cooling the ground to the point were it is colder than the air flowing over it. The soil heat flux shows a similar behavior in that it decreases to near -20% of reference day values within an hour after the storm event. However, unlike any of the other fluxes, the soil heat flux does not begin to diminish until about one half hour after the rain has began to reach the ground. It then quickly falls to near -20% of clear day values. Since the soil heat flux is highly dependent on the soil moisture content, the 30 minute lag exhibited by the soil fluxes relative to the sensible and latent heat fluxes is consistent with an increase in soil heat capacity due to the sudden introduction of large amounts of water into the surface layer soil horizons.

The next two panels of Figure 35, panels four and five from the top, display the composite shortwave and longwave radiative flux measurements.

The shortwave fluxes, K↓ and K↑, drop from near 90% of reference day values to around 10% of reference day values during the hour proceeding the arrival of the downdraft, then recover to 50% of reference day values two or three hours later. The downwelling longwave radiation flux is steadily 5% above reference day values from 5 hours before the rainshaft arrival until the hour before the outflow reaches the site. The downwelling longwave radiation increases during this hour to 10% above reference while the longwave up decreases to 85% of its reference value. The gain in longwave down and the loss in longwave up are not coincident. The gain in longwave down occurs some 30 to 40 minutes before the peak downdraft, while the loss of longwave up, which is coincident with large amounts of rainfall reaching the surface, is most pronounced directly beneath the rainshaft. A more detailed analysis of the composite radiative fluxes along with the calculation of a spectral transmittance is presented in section 4.4.

Figure 35, panel six, shows the averaged divergence for the composite storm. This is not percentage of the reference day because the reference day signal is mostly noise associated with the light and variable wind conditions found on the reference day. The storm signals tend to be sufficiently powerful as to completely overwhelm the background conditions. As expected, the divergence signal is consistently negative around -300 x 10^{-6} s^{-1} before the storm and then drops rapidly to a minimum value around -800 x 10^{-6} s^{-1}. The signal then quickly peaks near 1000 x 10^{-6} s^{-1} as the downdraft moves over the site. The time span between the negative and positive divergence peaks is about 30 minutes. Once the storm has passed, the divergence signal hovers around zero.

Finally, it should be pointed out that the satellite reflectance shown in Figure 35, top panel, and rainfall measured at the FSU sites shown in Figure 35, bottom panel, are in close agreement. The rapid changes in surface fluxes are

also coincident with the maximum surface rainrates. The rainfall measurements, the flux measurements, the satellite measurements and the KSC wind network divergence calculated over each site are all derived from mutually independent measuring systems. The validity of the compositing process is therefore credible because of the close simultaneity of these quite disparate and independent observations.

4.3 Recovery of Latent Heat Energy by the Atmosphere

In order to gain a more complete understanding of the effects of clouds on the hydrology of the Merritt Island system, the rate of recovery of the surface after a convective event has been investigated. The recovery time (T) is defined to be the time necessary for the surface latent heat flux to return to the atmosphere the total amount of latent heat energy lost to the ground in the form of rainfall. The latent heat fluxes calculated for the composite storm are representative of the fluxes which actually take place beneath storm downdrafts. A typical storm event, in terms of latent heat fluxes, was constructed by multiplying the composite percentage latent heat flux depicted in Figure 35 by the reference day values in Figure 33(a). The composite storm latent heat fluxes and average rainfall rates were centered around 1535 LDT on the reference day, which was the mean time of arrival of the downdraft over the sites. By concatenating the resulting composite storm day with the reference days (which are also clear days), the recovery time for a typical storm over a given location can be determined by calculating the difference between the accumulated latent heat energy in the rainfall and the accumulated latent heat energy in the latent heat fluxes from the surface layer into the atmosphere. The difference between the accumulated energies ($\Delta E(t)$) for each time step t is given by:

$$\Delta E(t) = \{RR(\tau)L_v\rho_w - QE(\tau)\}\Delta X\Delta Y d\tau \qquad (21)$$

where:

$RR(\tau)$ = measured rainrate ($m \bullet s^{-1}$)

L_v = latent heat of vaporization ($2.375 \times 10^6 J \bullet kg^{-1}$)

ρ_w = density of water ($10^3 kg \bullet m^{-3}$)

$QE(\tau)$ = measured latent heat flux ($W \bullet m^{-2}$)

$\Delta X = 1$ m

$\Delta Y = 1$ m

$d\tau$ = time step (300 s)

The recovery time (T) is calculated from:

$$\int_0^T \Delta E(\tau) d\tau = 0 \qquad (22)$$

In this way, four 'empirical models' were designed. The first model consists of a storm day at a site followed by continuous clear days. The second model is that of a storm day followed by continuous dry days with Type 1 flow. The third model is the storm day followed by continuous dry days with Type 2 flow, and the fourth model consists of the storm day followed by continuous days when it rained again every day. Figure 36 show the results of these calculations. In the case of the storm followed by continuous clear days, the latent heat requires about 3.5 days to return the moisture from the rainfall back into the atmosphere. The cases of dry Types 1 and 2 flow require 4.5 days to evaporate off the water, about one day longer than the clear day case. However, even as close as Type 1 and 2 dry days are, the case of Type 2 flow requires a slightly longer time to evaporate off the rainfall than does the Type 1 case. This is in agreement with the differences in the two regimes as found in this study, that is, the Type 1 flow, generally southeasterly, is less likely to have substantial convective activity develop than the Type 2 flow. This implies that the days of

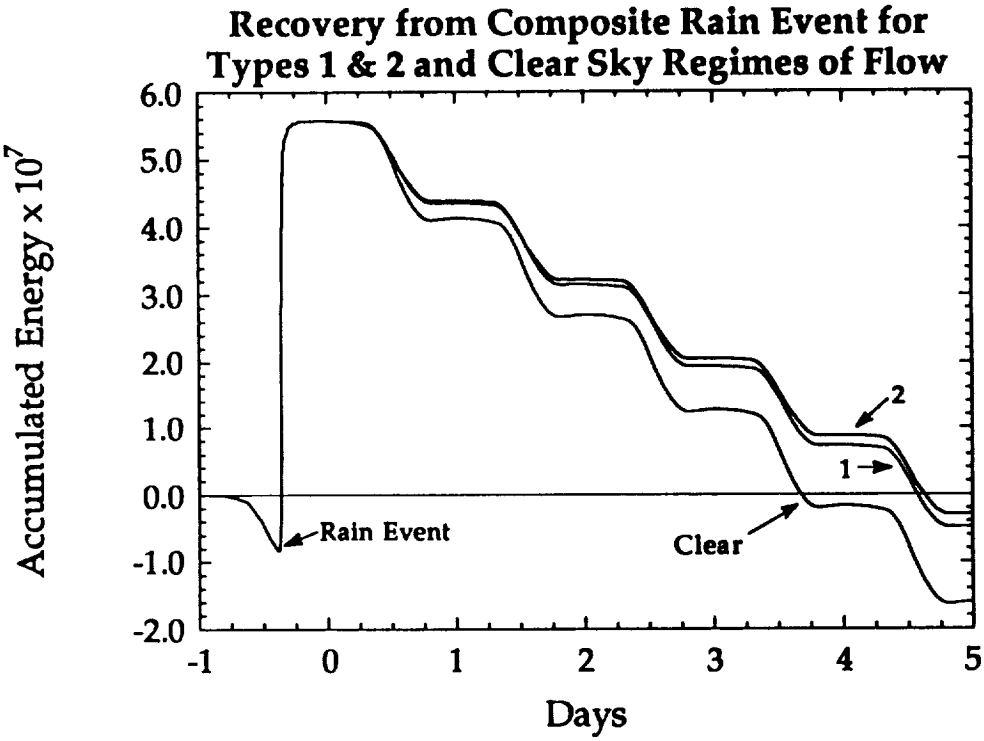

Figure 36: Recovery from the composite rainfall event for continuous clear days, days of Type 1 flow and days of Type 2 flow.

Type 1 flow would be more cloud free than the days of Type 2 flow and hence, have a higher accumulated latent heat flux for that day. The case of the composite storm followed by continuous days of rain events behaves as expected. The system never recovers. This case is not shown. It accumulates moisture at the surface at a higher rate than latent heat transfer can remove it. Table 11 lists the different flow regimes, the total cumulative amounts of latent heat for an average day in that regime, the amount of an average rainfall event, and the amount of energy required to evaporate off the rainfall accumulated at the ground.

It may be noted at this point that there were two periods during the CaPE experiment when a site went more than 3.5 days without receiving rainfall. The storm analysis presented in this section applies only to the storm rainshaft. The area covered by these rainshafts is rather small, on the order of a few square kilometers. While it is true that not a single day passed during the CaPE experiment when rain did not fall somewhere in the PAM network, for a given locality, this is not the case. One day has been mentioned here, August 6, when no rain was recorded anywhere on Merritt Island. Notably, this was the only such day. The larger the area, the less likelihood of no rain. The smaller the area, the greater likelihood of spending a period of time equivalent to the recovery time without rainfall. If it rains at a given point every day, the atmosphere will experience an ever increasing loss of latent heat energy through latent heat release. However, specific localities rarely experience these conditions, and are replenished with atmospheric water vapor during rainless periods, which occur locally at frequent intervals.

Table 11: Energy accumulations for average days in each regime.

Event	Energy (Joules/Day)
Clear Day	1.433×10^7
Type 1 Flow	1.211×10^7
Type 2 Flow	1.721×10^7
Rainfall (27.5 mm)	6.531×10^7

4.4 Shortwave Transmittance and Longwave Equilibrium in the Composite Storm Downdraft

In this section, a spectral transmittance is calculated for that part of the visible spectrum sensed by the GOES satellite. The absorbed (net) visible energy flux at the top of the atmosphere (TOA) is given by:

$$V^*_{TOA} = V\downarrow_{TOA}(1-R_f) \tag{23}$$

where R_f is the reflectance observed by the satellite and $V\downarrow_{TOA}$ is the downwelling energy in the satellite bandwidth, given by:

$$V\downarrow_{TOA} = S_o^{vis} D^2 \cos(\theta_o) \tag{24}$$

Here, S_o^{vis} is the solar constant in the satellite bandwidth, θ_o is the solar zenith angle, and D is the ratio of the mean to actual Earth-sun distance.

At the top-of-atmosphere, the proportion of the total amount of energy flux in the bandwidth 0 - 0.7 μm contained within the satellite bandwidth of 0.5 - 0.7 μm is given by:

$$\alpha = \left[\frac{\int_{0.5}^{0.7} S_o(\lambda)d\lambda}{\int_{0.0}^{0.7} S_o(\lambda)d\lambda} \right] \tag{25}$$

where $S_o(\lambda)$ is the solar constant as a function of wavelength. Using the most current measurements of the solar constant and the tabulated results of Fröhlich and London (1986), it was possible to calculate:

$$\int_{0.5}^{0.7} S_o(\lambda)d\lambda = 345.6 \text{ W} \cdot \text{m}^{-2} \tag{26}$$

and

$$\int_{0.0}^{0.7} S_o(\lambda)d\lambda = 640.8 \text{ W} \cdot \text{m}^{-2} \tag{27}$$

so that α = 0.5393. To first order, it is assumed that α remains constant throughout the atmospheric column. At the surface, the energy flux in the range 0.0 to 0.695 μm is found from the measured downwelling total solar flux, $K\downarrow_{SFC}$, and the measured downwelling near-infrared flux $N\downarrow_{SFC}$ by:

$$V\downarrow_{SFC} = \left(K\downarrow_{SFC} - N\downarrow_{SFC}\right) \tag{28}$$

The energy in the bandwidth 0.5 to 0.7 μm is then estimated from:

$$V\downarrow_{VIS} = \alpha\left(K\downarrow_{SFC} - N\downarrow_{SFC}\right) \tag{29}$$

and the VIS transmittance (τ_{VIS}) is calculated from:

$$\tau_{VIS} = \left(\frac{V\downarrow_{VIS}}{V^*_{TOA}}\right) \tag{30}$$

The results for the cloud transmittance calculations are shown in Figures 37(a) and 37(b). Figure 37(a) shows the downwelling visible radiation at the top-of-atmosphere ($V\downarrow_{TOA}$), the net visible radiation (V^*_{TOA}), and the surface layer downwelling radiation in the satellite bandwidth ($V\downarrow_{VIS}$). Figure 37(b) is the cloud transmittance for the composite storm event. The transmittance drops from a pre-storm maximum of around 0.85 to a minimum value of near 0.1 very quickly as the downdraft approaches. After the peak divergence, the transmittance slowly recovers to a post-storm maximum of around 0.6 about 2.5 hours after the storm.

In addition to the visible transmittance, a calculation of net longwave radiation for the composite storm has also been performed. This is calculated by:

$$L^*_{SFC} = \left(L\downarrow_{SFC} - L\uparrow_{SFC}\right) \tag{31}$$

where $L\downarrow_{SFC}$ and $L\uparrow_{SFC}$ are the downwelling and upwelling fluxes measured at the surface. Figure 38 compares L^*_{SFC} for the composite storm case and the clear day case. In the storm case, L^*_{SFC} goes positive up to around 7 $W \bullet m^{-2}$ just after storm passage. This means sky radiation generated below cloud base is greater

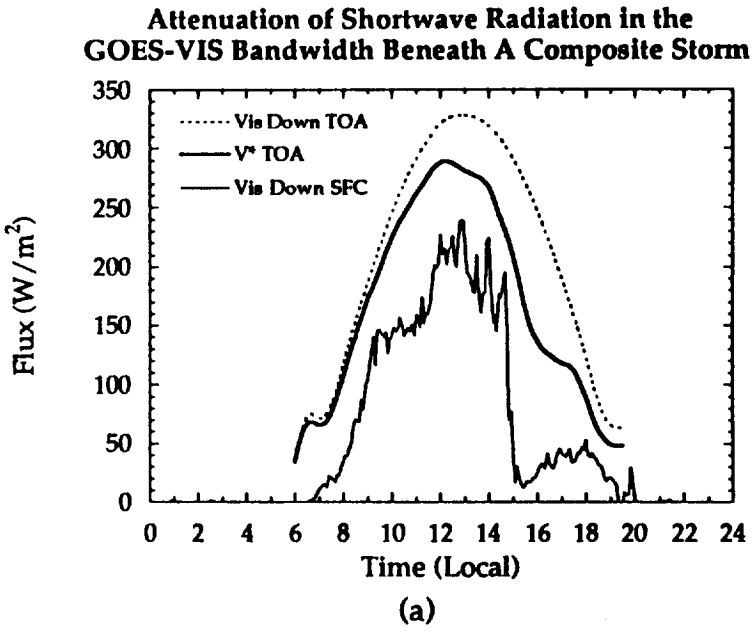

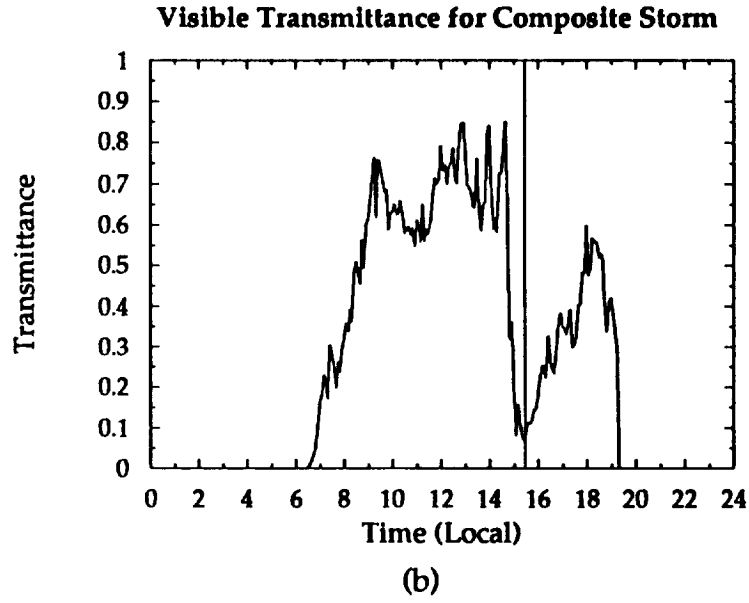

Figures 37(a) and 37(b): Attenuation of shortwave radiation beneath the composite storm; $V\downarrow_{TOA}$ (dashed line), V^*_{TOA} (heavy solid line), and $V\downarrow_{SFC}$ (thin solid line) (a). Visible transmittance for the composite storm (b).

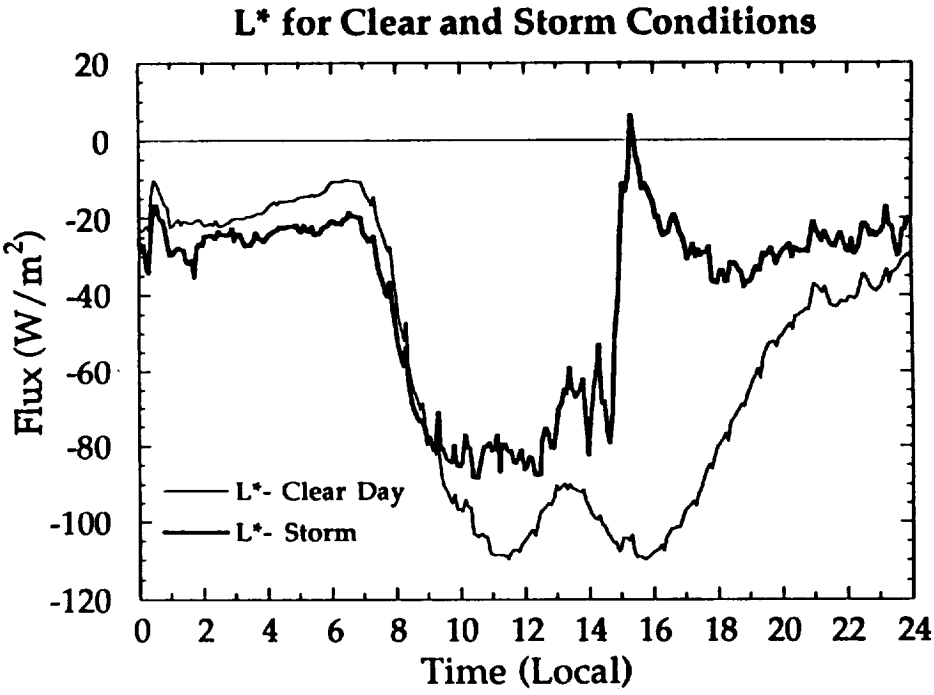

Figure 38: Net longwave radiation for clear sky conditions (thin solid line) and the composite storm values (heavy solid line).

than surface emission, which is the opposite sign of the general clear sky case. This is caused by rainfall cooling the ground while the cloud base emission remains radiatively large.

5.0 Summary and Conclusions

Five independent data sets collected over Merritt Island, Florida during CaPE have been analyzed in an investigation of the interrelationships and feedback processes between surface fluxes and clouds contained within the Florida sea breeze convergence zone. Analysis of soundings from the Cape Canaveral Air Force Station were used to show that the flow over Merritt Island is characterized by easterlies aloft and pulses of westerly momentum in the lower layers, alternating with deep easterlies at all levels. Associated increases in moist static energy departures during the low level westerly regime indicate the presence of active convection.

The surface winds fields, as represented by the mean vertical speeds calculated from the combined PAM and KSC wind networks over Merritt Island, showed four basic regimes during the CaPE experimental period. There were two periods of three to four days duration at the beginning and at the end of the field experiment which were clearly the result of synoptic scale disturbances. The first disturbed period resulted in thunderstorms over the island throughout the day while during the second disturbed period convection was suppressed because of large scale subsidence associated with hurricane Bob offshore. The remaining periods of the experiment exhibited two types of local flow over Merritt Island. In Type 1 flow, the flow over the island remained convergent 24 hours a day. In Type 2 flow, the flow over the island was divergent during the night and convergent during the day. In essence, the Type 2 mode is the classical sea breeze mode. Correlation of days in Type 1 and Type 2 flows with the

sounding analysis revealed that the Type 1 days were associated with deep easterlies while Type 2 days were associated with a westerly component in the lower levels. Further analysis using the surface winds in the mainland part of the PAM network established that Type 1 flow tended to have an easterly component, while the Type 2 flows tended to have a westerly component.

Examination of the site specific divergence immediately over the two surface flux sites on Merritt Island allowed the two types of flow to be further separated into active or inactive days, depending on the occurrence or nonoccurrence of storm signals in the wind field over each site. Analysis of 1x1 km GOES-VIS half-hourly satellite imagery and the measured rainfall was also used to identify active or inactive days. The sea breeze convergence zone was observed using data visualization of the divergence fields within the PAM network and was tracked on a daily basis It was found that the inland propagation speed of the sea breeze front on Type 1 days had a speed of 2.89 $m \cdot s^{-1}$ while on Type 2 days it was found to have a slightly lower propagation speed of 2.69 $m \cdot s^{-1}$. Merging of the west coast sea breeze and the east coast sea breeze often resulted in storms propagating back over the east coast and Merritt Island. The return propagation speeds were 14.3 $m \cdot s^{-1}$ for Type 1 flow and 9.0 $m \cdot s^{-1}$ for Type 2 flow. The larger return speed in the Type 1 flow may be attributed to the eastward propagation of a gravity wave created when the two fronts merge.

The effects of cloudiness associated with sea breeze convection was easily detected in the surface flux measurements at both sites for active and inactive regimes. The absence or presence of clouds was the determining factor in the diurnal evolution of net radiation and latent heat as compared to cloud free days. However, the soil heat fluxes appeared to be as much influenced by the nature of

the soil as by the presence of clouds. The sensible heat fluxes also appeared to be more independent of cloudiness than the net radiation or latent heat flux, and showed the same general tendency to be site specific.

A composite storm was constructed around specific cases when a downdraft was observed to have passed directly over one of the flux sites, and the behavior of the surface energy budget directly underneath the rainshaft has been described. All the thermodynamic fluxes were suppressed, with some out-of-phase behavior on the part of the ground fluxes. The downwelling solar flux was dramatically diminished, whereas the net longwave flux showed an increase in the sub-downdraft surface layer due to a rapid decline in the upwelling component because of surface wetting by rainfall. Using the composited satellite signal to determine top-of-atmosphere net visible radiation and the FSU-SREBS surface measurements of downwelling visible radiation, the visible transmittance beneath an average storm was calculated. The transmittance was found to be near 0.1 directly beneath the downdraft, which is strongly supportive of the black cloud hypothesis.

The composite storm and non-raining Type 1 and 2 days, as well as an average clear day, were concatenated, and a clear day recovery time scale for a typical storm was found to be 3.5 days with the associated e-folding time scale of 1.5 days. For a non-raining yet non-cloud free day, the recovery time was found to be 4.5 days and the e-folding time was found to be 1.75 days.

6.0 Appendix 1: The Bivariate Interpolation Scheme

The bivariate interpolation scheme used in this analysis has been copyrighted by the National Center for Atmospheric Research. The NCAR method is actually a version of the method developed by Akima (1984). It interpolates irregularly spaced data points to a regularly spaced grid. The method involves three basic steps.

The first is the triangulation of the plane of data. That is, the plane containing the data is divided into a number of triangles such that the smallest angle of each triangle is a maximum. The second step is the estimation of the first and second partial derivatives at each data point. Making these estimations involves the estimation of the first partial derivatives and the second partial derivatives. The second derivatives are estimated from the first derivative by the same procedure used to estimate the first derivative from the data. The method for estimation of the first derivatives at each data point (P_o), involves several procedures. A set of n_t data points that are closest to P_o are selected from all data points in the data plane. A vector product for all combinations of i and j is then calculated such that:

$$V_{i,j} = \overline{P_oP_i} \cdot \overline{P_oP_j} \tag{32}$$

where i,j = 1,2,3,. . . ,n_t, and where P_o, P_i, and P_j are arranged to be counterclockwise in the plane of data such that the z component of $V_{x,y}$ is positive. The method then calculates the vector sum (V) of all $V_{i,j}$'s. The

estimation of the first derivative is done by estimating z_x and z_y as the slope of a plane that is normal to the vector sum V:

$$z_x = -\frac{V_x}{V_z} \tag{33}$$

$$z_y = -\frac{V_y}{V_z} \tag{34}$$

This derivative estimation is then repeated on the values just obtained to calculate the second derivative. The third step is the fitting of a fifth-degree polynomial in x and y in each triangle. The interpolated data are then taken from the fitted polynomial.

7.0 Appendix 2: Testing the Interpolation Scheme

In order to verify that the divergence calculation scheme is correct, a test of the system is performed. A continuous data field was constructed using a sine relationship defining the velocity potential, $\Psi(x,y)$:

$$\psi(x,y) = A \sin\left(\frac{2\pi x}{\Delta x}\right) \sin\left(\frac{\pi y}{\Delta y}\right) \tag{35}$$

where A is a constant amplitude term and Δx, Δy are the fixed dimensions of the entire interpolation grid. The velocity at a grid point (x,y) can then be found from the gradient of the velocity potential:

$$\nabla\psi = \frac{\partial\psi}{\partial x}\hat{i} + \frac{\partial\psi}{\partial y}\hat{j} \tag{36}$$

where $\hat{i}$ and $\hat{j}$ are unit vectors in the u and v component directions of a surface wind field. Therefore, u and v can be calculated from:

$$u(x,y) = \frac{A2\pi}{\Delta x} \cos\left(\frac{2\pi x}{\Delta x}\right) \sin\left(\frac{\pi y}{\Delta y}\right) \tag{37}$$

$$v(x,y) = \frac{A\pi}{\Delta y} \sin\left(\frac{2\pi x}{\Delta x}\right) \cos\left(\frac{\pi y}{\Delta y}\right) \tag{38}$$

such that a value of u and v can be assigned to each grid point in the interpolation grid. For the test, a 100 by 100 analytical grid was overlaid on the 20 by 20 grid to simulate a continuous function.

Using the analytical data set, a comparison of actual to interpolated values was carried out. Values corresponding to the locations of the PAM sites were taken from the analytical data set and then interpolated to the 20 by 20 grid network using the bivariate interpolation scheme. These values were then

contoured. Values corresponding to each of the 20 by 20 grid points were then taken from the analytical data set and also contoured. This analysis was performed separately for the KSC network.

The calculations resulted in two separate data sets; one for the PAM network and one for the KSC network. Each separate set contains two values for each of the 20 by 20 grid points, one from the interpolation of the analytical data and one from the analytical data itself. When the values at each grid point are correlated over the PAM network, the resulting correlation coefficient is quite high. When the values at each grid point are correlated over the KSC network, the resulting correlation coefficient is even higher. This was the expected result due to the relative spacing of the stations. That is, each PAM station represents approximately 8 squares on the grid, while each KSC station represents just over one grid square. Thus, the interpolation scheme has to interpolate further between the PAM stations than between the KSC stations. Even considering the larger interpolation lengths, the correlation coefficient are remarkably close. The PAM Network has an r value of 0.995 while the KSC Network has an r value of 0.999. These exceptionally high correlation coefficient indicate that the interpolation scheme was accurately showing how the actual wind fields were behaving and was not introducing any imaginary features into the data field. Figures 39(a) and 39(b) show the correlation plots for the PAM and KSC Networks, respectively as a means of demonstrating how well the interpolated data agrees with the actual signal.

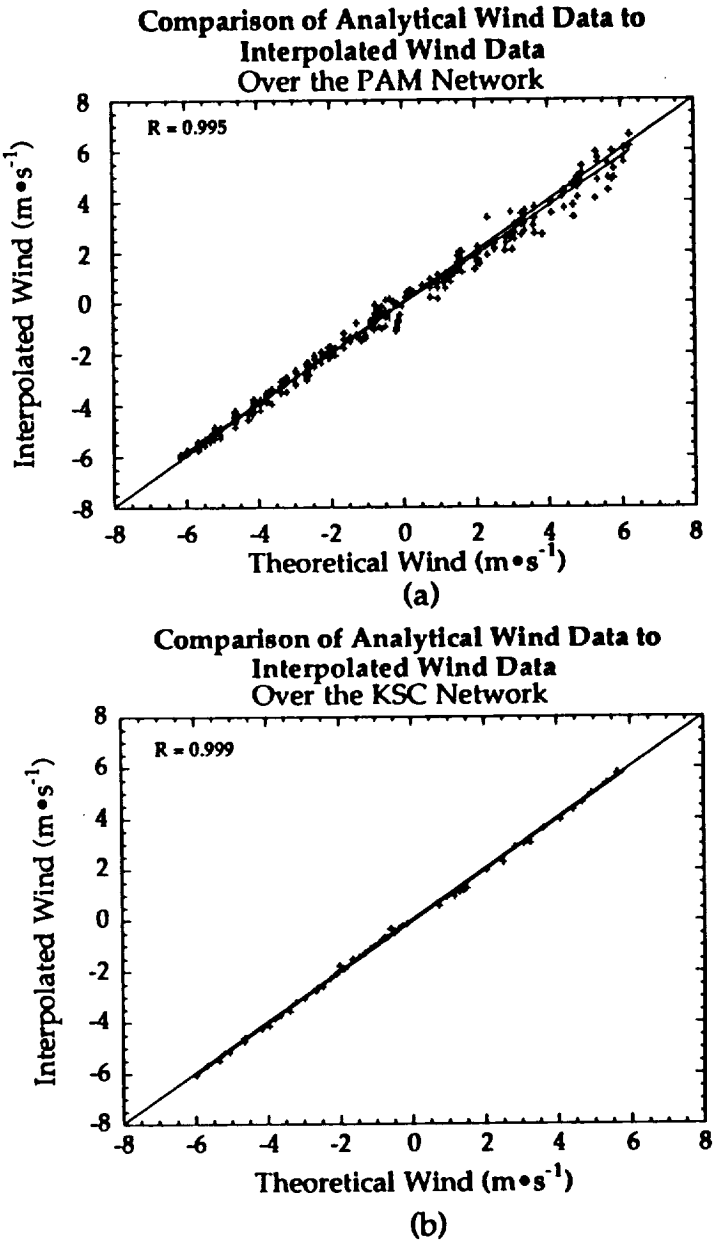

Figures 39(a) and 39(b): Correlation between actual data from the bivariate interpolation grid and data from the analytical signal interpolated by the bivariate routine from the PAM network (a) and KSC network (b).

8.0 References

Akima, H., 1984: On estimating partial derivatives for bivariate interpolation of scattered data. *Rocky Mountain Journal of Mathematics*, **14**, 41-52.

Arritt, R.W., 1993: Effects of the large-scale flow on characteristic features of the sea breeze. *J. Appl. Meteor.* , **32**, 116-125.

Bechtold, P., J.P. Pinty, and P. Mascart, 1991: A numerical investigation of the influence of large-scale winds on sea-breeze- and inland-breeze-type circulations. *J. Appl. Meteor.*, **30**, 1268-1279.

Blanchard, D.O., and R.E. López, 1985: Spatial patterns of convection in south Florida. *Mon. Wea. Rev.*, **113**, 1282-1299.

Burpee, R.W., 1979: Peninsula-scale convergence in the south Florida sea breeze. *Mon. Wea. Rev.*, **107**, 852-860.

Byers, H.R., and R.R. Braham, 1949: The Thunderstorm. US Government Printing Office.

Byers, H.R., and H.R. Rodebush, 1948: Causes of thunderstorms of the Florida peninsula. *J. Meteor.*, 5, 275-280.

Carlson, T.N., J.K. Dodd, S.G. Benjamin, and J.N. Cooper, 1981: Satellite estimation of the surface energy balance, moisture availability and thermal inertia. *J. Appl. Meteor.*, **20**, 67-87.

Chahine, M.T., 1992: GEWEX: The global energy and water cycle experiment. *EOS* , **73**, 8-14.

Cooper, H.J., and E.A. Smith, 1993: The importance of short term forecasting of thunderstorms to launch operations at Cape Canaveral. *Bull. Amer. Meteor. Soc.*, **74**, 81-86.

Cooper, H.J., M. Garstang, and J. Simpson, 1982: The diurnal interaction between convection and peninsular-scale forcing over south Florida. *Mon. Wea. Rev.*, **110**, 486-503.

Dalu, G.A., and R.A. Pielke, 1989: An analytical study of the sea breeze. *J. Atmos. Sci.*, **46**, 1815-1825.

Estoque, M.A., 1962: The sea breeze as a function of the prevailing synoptic situation. *J. Atmos. Sci.*, **19**, 244-250.

Foote, G.B., ed., 1991: Scientific overview and operations plan for the convection and precipitation/electrification experiment, National Center for Atmospheric Research, 1-145.

Fouquart, Y., J. C. Buriez, M. Herman, and R. S. Kandel, 1990: The influence of clouds on radiation: a climate modeling perspective. *Reviews of Geophysics*, **28**, 145-166.

Frank, N.L., P.L. Moore, and G.E. Fisher, 1967: Summer shower distribution over the Florida peninsula as deduced from digitized radar data. *J. Appl. Meteor.*, 6, 309-316.

Fröhlich, C., and J. London, ed., 1986: Revised instruction manual on radiation instruments and measurements. *World Climate Research Programme*, No. 7, 119-135.

Gentry, R.C., and P.L. Moore, 1954: Relation of local and general wind interaction near the sea coast to time and location of air-mass showers. *J. Meteor.*, **11**, 507-511.

Holle, R.L., A.I. Watson, R.E. López, K.W. Howard, R. Oritz, and L. Li, 1992: Meteorological studies to improve short-range forecasting of lightning/thunderstorms within the Kennedy Space Center area, *NSSL Final Report*, 1-91.

Mahfouf, J. F., E. Richard, and P. Mascart, 1987: The influence of soil and vegetation on the development of mesoscale circulations. *Clim. Appl. Meteor.*, **26**, 1483-1495.

Mahrer, Y., and R.A. Pielke, 1977: The effects of topography on sea and land breezes in a two-dimensional numerical model. *Mon. Wea. Rev.*, **105**, 1151-1162.

Neumann, J., 1973: The sea and land breezes in the classical Greek literature. *Bull. Amer. Meteor. Soc.*, **54**, 5-8.

Neumann, J., and Y. Mahrer, 1971: A theoretical study of the land and sea breeze circulation. *J. Atmospheric. Sci.*, **28**, 532-542.

Ookouchi,Y., M. Segal, R.C. Kessler, and R.A. Pielke, 1984: Evaluation of soil moisture effects on the generation and modification of mesoscale circulations. *Mon. Wea. Rev.*, **112**, 2281-2292.

Pielke, R.A., 1974(a): A comparison of three-dimensional and two-dimensional numerical predictions of sea breezes. *J. Atmos. Sci.*, **31**, 1577-1585.

Pielke, R.A., 1974(b): A three-dimensional numerical model of the sea breeze over south Florida. *Mon. Wea. Rev.*, **102**, 115-139.

Rossow, W.B., 1989: Measuring cloud properties from space: a review. *J. Clim.*, **2**, 201-213.

Segal, M., and R.W. Arritt, 1992: Nonclassical mesoscale circulations caused by surface sensible heat-flux gradients. *Bull. Amer. Meteor. Soc.*, **73**, 1593-1604.

Segal, M., R. Avissar, M.C. McCumber, and R.A. Pielke, 1988: Evaluation of vegetation effects on the generation and modification of mesoscale circulations. *J. Atmos. Sci.*, **45**, 2268-2292.

Simpson, J., Th. D. Keenan, B. Ferrier, R.H. Simpson, and G.J. Holland, 1993: Cumulus mergers in the maritime continent region, *Meteorology and Atmospheric Physics*, **51**, 73-99.

Simpson, J., N.E. Wescott, R.J. Clerman, and R.A. Pielke, 1980: On cumulus mergers, *Arch. Met. Geoph. Biocl., Ser, A*, **29**, 1040.

Smith, E.A., W.L. Crosson, and B.D. Tanner, 1992: Estimation of surface heat and moisture fluxes over a prairie grassland, Part 1: In situ energy budget measurements incorporating a cooled mirror dew point hygrometer, *Journal of Geophysical Research*, 97, 18,557-18,582.

Smith, E.A., M. M.-K. Wai, H.J. Cooper, M.T. Rubes, and A. Hsu, 1993: Linking boundary layer circulations and surface processes during FIFE 89. Part 1: Observational analysis using FIFE Information System (FIS), *Journal of Atmos. Sci.*, submitted.

Smith, E. A. and H. E. Fuelberg, 1989: The design of a Florida-based satellite Earth station. Final Rep.-TRDA Project 104, Dept. of Meteorology & Supercomputer Computations Research Institute, Florida State University, Tallahassee, Florida, 15 pp.

Ulanski, S.L., and M. Garstang, 1978: The role of surface divergence and vorticity in the life cycle of convective rainfall. Part I: Observation and analysis. *J. Atmos. Sci.*, **35**, 1047-1062.

Walsh, J.E., 1974: Sea breeze theory and applications. *J. Atmos. Sci.*, **31**, 2012-2026.

Watson, A.I., and D.O. Blanchard, 1984: The relationship between total area divergence and convective precipitation in south Florida, *Mon. Wea. Rev.*, **112**, 673-685.

Watson, A.I., R.L. Holle, R.E. López, and R. Oritz, 1991: Surface wind convergence as a short-term predictor of cloud-to-ground lightning at KSC. *Wea. Forecasting*, **6**, 49-64.

Woodley, W.L., J. Jordan, A. Barnston, J. Simpson, R. Biondini, and J. Flueck, 1982: Rainfall results of the Florida area cumulus experiment, 1970-76. *J. Appl. Meteor.*, **21**, 139-164.

Xian, Z., and R.A. Pielke, 1991: The effects of width of landmasses on the development of sea breezes. *J. Appl. Meteor.*, **30**, 1280-1304.

Yan, H., and R.A. Anthes, 1988: The effect of variations in surface moisture on mesoscale circulations. *Mon. Wea. Rev.*, **116**, 192-208.

Yan, H., and R.A. Anthes, 1987: The effect of latitude on the sea breeze. *Mon. Wea. Rev.*, **115**, 936-956.

Yeh, T.-C., R.T. Wetherald, and S. Manabe, 1984: The effect of soil moisture on the short-term climate and hydrology change-a numerical experiment. *Mon. Wea. Rev.*, **112**, 474-490b

Zhong, S., J.M. Leone, Jr., and E.S. Takle, 1991: Interaction of the sea breeze with a river breeze in an area of complex coastal heating. *Boundary-Layer Meteorology*, **56**, 101-139.

☆U.S. GOVERNMENT PRINTING OFFICE 1993—733-050/80107

REPORT DOCUMENTATION PAGE

Form Approved
OMB No. 0704-0188

Public reporting burden for this collection of information is estimated to average 1 hour per response, including the time for reviewing instructions, searching existing data sources, gathering and maintaining the data needed, and completing and reviewing the collection of information. Send comments regarding this burden estimate or any other aspect of this collection of information, including suggestions for reducing this burden, to Washington Headquarters Services, Directorate for Information Operations and Reports, 1215 Jefferson Davis Highway, Suite 1204, Arlington, VA 22202-4302, and to the Office of Management and Budget, Paperwork Reduction Project (0704-0188), Washington, DC 20503.

1. AGENCY USE ONLY (Leave blank)	2. REPORT DATE	3. REPORT TYPE AND DATES COVERED
	July 1993	Contractor Report (Interim)

4. TITLE AND SUBTITLE

A Study of the Merritt Island, Florida Sea Breeze Flow Regimes and Their Effect on Surface Heat and Moisture Fluxes

5. FUNDING NUMBERS

NAG8-916

6. AUTHOR(S)

M. T. Rubes, H. J. Cooper, and E. A. Smith

7. PERFORMING ORGANIZATION NAME(S) AND ADDRESS(ES)

Department of Meteorology
Florida State University
Tallahassee, FL 32306-3034

8. PERFORMING ORGANIZATION REPORT NUMBER

M-727

9. SPONSORING / MONITORING AGENCY NAME(S) AND ADDRESS(ES)

George C. Marshall Space Flight Center
Marshall Space Flight Center, AL 35812

10. SPONSORING / MONITORING AGENCY REPORT NUMBER

NASA CR-4537

11. SUPPLEMENTARY NOTES

Prepared for Earth Science & Applications Division, Space Science Laboratory, Science & Engineering Directorate. COR: S. J. Goodman

12a. DISTRIBUTION / AVAILABILITY STATEMENT

Unclassified--Unlimited
Subject Category: 47

12b. DISTRIBUTION CODE

13. ABSTRACT *(Maximum 200 words)*

Data collected during the Convective and Precipitation/Electrification Experiment have been analyzed as part of an investigation of the sea breeze in the vicinity of Merritt Island, Florida. Analysis of near-surface divergence fields shows that the classical 24-hour oscillation in divergence over the island due to the direct sea breeze circulation is frequently disrupted and exhibits two distinct modes: (1) the classical sea breeze pattern and (2) deviations from that pattern. A comparison of clear day surface energy fluxes with fluxes on other days indicates that changes in magnitudes were dominated by the presence or absence of clouds. Non-classical sea breeze days tended to lose more available energy in the morning than classical sea breeze days due to earlier development of small cumulus over the island. A composite storm of surface winds, surface energy fluxes, rainfall, and satellite visible data was constructed. A spectral transmittance over the visible wavelengths for the cloud cover resulting from the composite storm has been calculated. It is shown that pre-storm transmittances of 0.8 fall to values near 0.1 as the downdraft moves directly over the site. It is also found that under post-composite storm conditions of continuous clear sky days, 3.5 days are required to evaporate back into the atmosphere the latent heat energy lost to the surface by rainfall.

14. SUBJECT TERMS

Boundary Layers, Surface Fluxes, Meteorology, Precipitation

15. NUMBER OF PAGES

158

16. PRICE CODE

AO8

17. SECURITY CLASSIFICATION OF REPORT	18. SECURITY CLASSIFICATION OF THIS PAGE	19. SECURITY CLASSIFICATION OF ABSTRACT	20. LIMITATION OF ABSTRACT
Unclassified	Unclassified	Unclassified	Unlimited

National Aeronautics and
Space Administration
Code JTT
Washington, DC
20546-0001

Official Business

Penalty for Private Use, $300

SPECIAL FOURTH-CLASS RATE
POSTAGE & FEES PAID
NASA
Permit No. G-27

NASA

POSTMASTER:

If Undeliverable (Section 158
Postal Manual) Do Not Return